

The Pennsylvania State University

The Graduate School

College of Engineering

**DESIGN, MODELING AND OPTIMIZATION OF PIEZOELECTRIC
ACTUATORS**

A Dissertation in

Mechanical Engineering

by

Hareesh Kumar Reddy Kommepalli

© 2010 Hareesh Kumar Reddy Kommepalli

Submitted in Partial Fulfillment

of the Requirements

for the Degree of

Doctor of Philosophy

May 2010

The dissertation of Hareesh Kumar Reddy Kommepalli was reviewed and approved*
by the following:

Christopher D. Rahn
Professor of Mechanical Engineering
Dissertation Co-Advisor
Co-Chair of Committee

Srinivas A. Tadigadapa
Associate Professor of Electrical Engineering
Dissertation Co-Advisor
Co-Chair of Committee

Ashok D. Belegundu
Professor of Mechanical Engineering

M. Amanul Haque
Associate Professor of Mechanical Engineering

Christopher L. Muhlstein
Associate Professor of Materials Science and Engineering

Karen A. Thole
Professor of Mechanical Engineering
Department Head of Mechanical and Nuclear Engineering

*Signatures are on file in the Graduate School.

Abstract

Microactuators provide controlled motion and force for applications ranging from RF switches to microfluidic valves. Large amplitude response in piezoelectric actuators requires amplification of the small strain, exhibited by the piezoelectric material, used in the construction of such actuators. This research studies a uniflex microactuator that combines the strain amplification mechanisms of a unimorph and flexural motion to produce large displacement and blocking force. The design and fabrication of the proposed uniflex microactuator are described in detail. An analytical model is developed with three connected beams and a reflective symmetric boundary condition that predicts actuator displacement and blocking force as a function of the applied voltage. The model shows that the uniflex design requires appropriate parameter ranges, especially the clearance between the unimorph and aluminum cap, to ensure that both the unimorph and flexural amplification effects are realized. With a weakened joint at the unimorph/cap interface, the model is found to predict the displacement and blocking force for the actuators fabricated in this work. This research also compares the performance of a uniflex actuator in terms of its displacement and blocking force with uniflex and flex-

tensional actuators. Analytical models for displacement and blocking force for all the three actuators are used in optimization, to study their relative performance. The uniflex actuator outperforms both unimorph and flextensional actuators in displacement, but, the unimorph actuator generates more blocking force. The uniflex actuator can therefore be used in applications that demand higher displacement and lower blocking force compared to a unimorph actuator.

This research introduces a novel T-beam actuator that can be fabricated by micromachining using a piezoelectric MEMS fabrication process or by dicing using a saw. With a T-shaped cross-section, and bottom and top flange and web electrodes, a cantilevered beam can bend in-plane and out-of-plane with unimorph actuation in both directions. Analytical models are developed to predict displacement, blocking force, and mechanical energy. Six prototypes of these T-beam actuators are fabricated by dicing and electrodes are deposited by photolithography and experimentally tested. The experimentally validated models are used to optimize the cross-section geometry for maximum displacement, blocking force, and mechanical energy. It is found that a cross section with ratio of web width b to total width s , b^* , and flange thickness t to total height h , t^* approaching zero produces maximum displacement. Also, the tip displacement is independent of bounding box of T-beam. The cross section with $b^* = t^* = 0.381$ produces maximum blocking force, while, $b^* = 0.25$, $t^* = 0.33$ produces maximum mechanical energy. A properly designed T-beam has better free tip displacement per unit cross section area than a unimorph. Also, a flange actuated T-beam requires lower voltage than a unimorph to generate same electric field.

Table of Contents

List of Figures	viii
List of Tables	xiv
Acknowledgments	xv
Chapter 1	
Introduction	1
1.1 Applications	2
1.2 Macroactuators	3
1.3 Microactuators	5
1.4 Current Research	6
1.5 Organization of the Dissertation	7
Chapter 2	
Design, Fabrication, and Performance of a Piezoelectric Uniflex Microactuator	8
2.1 Introduction	8
2.2 The Uniflex Actuator	9
2.3 Fabrication of the Uniflex Actuator	11
2.4 Uniflex Actuator Performance	14
2.4.1 Static Displacement Measurement	15
2.4.2 Blocking Force Measurement	18
2.5 Mathematical Modeling	20
2.6 Results and Discussion	26
2.6.1 Rigid Joint Model ($K_t = \infty$)	26
2.6.2 Weakened Joint Model ($K_t < \infty$)	29

Chapter 3	
Optimization of Piezoelectric Uniflex Actuator	35
3.1 Introduction	35
3.2 Unimorph, Flextensional, and Uniflex Actuators	35
3.3 Mathematical Models	37
3.4 Optimal Design	40
3.4.1 Maximized Displacement Design	42
3.4.2 Maximized Blocking Force Design	45
Chapter 4	
Piezoelectric T-beam Actuators	48
4.1 Introduction	48
4.2 The T-Beam Actuator Concept	50
4.3 Analytical Modeling	51
4.3.1 Nondimensional modeling	57
4.4 Fabrication Process	59
4.5 Prototyping and Experimental Setup	61
4.6 Experimental Testing and Validation	64
4.7 Optimization of the T-beam Cross Section	69
4.7.1 Displacement Optimization	71
4.7.2 Blocking Force Optimization	74
4.7.3 Energy Optimization	76
4.8 Comparison with Unimorph Actuator	78
Chapter 5	
Conclusions	82
5.1 Future Work	83
Appendix A	
Additional Results for Uniflex Actuator	85
A.1 Constants for Uniflex Displacement	85
A.2 Constants for Uniflex Blocking Force	86
A.3 Maximum Displacement Design	88
A.4 Maximum Displacement Design with Additional Flextensional Actuator Results	91
A.5 Maximum Blocking Force Design	94
A.6 Maximum Blocking Force Design with Additional Flextensional Actuator Results	97

Appendix B	
Additional Results for T-beam Actuator	101
Bibliography	110

List of Figures

2.1	Schematic representation of the (a) PZT Unimorph Actuator at 0 V and (b) at finite drive voltage V, (c) Uniflex actuator at 0 V and (d) Uniflex actuator at a finite drive voltage V	9
2.2	Finite element model of uniflex actuator: (a) Initial, and (b) after deflection	10
2.3	Schematic (not to scale) illustration of the uniflex fabrication process.	11
2.4	Photograph of a fabricated unimorph.	14
2.5	Photograph of the fabricated uniflex actuator array.	15
2.6	Zygo image of a 400 μm long flextensional actuator with (a) no bias and (b) bias of 10 V. 4.16 μm of displacement was measured. The displacement is the difference in the height of the aluminum cap with respect to the PZT actuator between the two cases.	16
2.7	Actuator deflection as a function of applied voltage for various lengths of the actuator and for (a) 1 μm thick PZT and 1 μm thick Al cap, (b) 1 μm thick PZT and 2 μm thick Al cap, (c) 1.4 μm thick PZT and 1 μm thick Al cap, (d) 1.4 μm thick PZT and 2 μm thick Al cap.	17
2.8	(a) Blocking force raw data obtained using the nanoindenter for 300 μm long actuator with 1 μm thick PZT and 1 μm thick Al cap. (b) The data is converted into a voltage-blocking force graph showing the hysteresis actuation behavior of the actuator.	19
2.9	Photograph (a) and X-X cross-section schematic of the initial (b) and deflected (c) uniflex actuator.	21
2.10	Geometrically exact uniflex actuator model displacement versus clearance L_1 for an actuator length $L_a=300 \mu\text{m}$, rigid joint ($K_t = \infty$), Aluminum cap thickness $t_a = 1 \mu\text{m}$, PZT thickness $t_p = 1 \mu\text{m}$, and other actuator parameters shown in Tab. 2.1: $w_2(L)$ (solid line) and $w_3(0)$ (dashed).	30
2.11	Displacement versus actuator length L_a for the four configurations of the actuator: Uniflex experimental data is shown as dots, and theoretical weakened joint displacement $w_2(L)$ is shown as the solid lines.	32

3.1	Schematic of deflected (a) unimorph, (b) flextensional, and (c) uniflex actuators.	36
3.2	Maximum displacement versus actuator length: uniflex actuator w_{UF} with $t_a = 1 \mu\text{m}$ (solid), unimorph actuator w_U (dotted), and flextensional actuator w_F with $t_a = 1 \mu\text{m}$ (dashed).	39
3.3	Blocking force for maximum displacement design versus actuator length: uniflex actuator F_{UF} with $t_a = 1 \mu\text{m}$ (solid), unimorph actuator F_U (dotted), and flextensional actuator F_F with $t_a = 1 \mu\text{m}$ (dashed).	39
3.4	Maximum displacement versus Al thickness ($L_a = 300 \mu\text{m}$): uniflex w_{UF} (solid), unimorph w_U (dotted), and flextensional w_F (dashed).	41
3.5	Blocking force for maximum displacement design versus Al thickness ($L_a = 300 \mu\text{m}$): uniflex F_{UF} (solid), unimorph F_U (dotted), and flextensional F_F (dashed).	41
3.6	Clearance for maximum displacement design versus Al thickness ($L_a = 300 \mu\text{m}$): uniflex (solid) and flextensional (dashed).	42
3.7	Maximum blocking force versus actuator length: uniflex actuator F_{UF} with clearance $L_1 = 2.7 \mu\text{m}$ (solid), unimorph actuator F_U (dotted), and flextensional actuator F_F with clearance $L_1 = 2.7 \mu\text{m}$ (dashed).	44
3.8	Displacement for maximum blocking force design versus actuator length: uniflex actuator w_{UF} with clearance $L_1 = 2.7 \mu\text{m}$ (solid), unimorph actuator w_U (dotted), and flextensional actuator w_F with clearance $L_1 = 2.7 \mu\text{m}$ (dashed).	44
3.9	Maximum blocking force versus clearance ($L_a = 300 \mu\text{m}$): uniflex actuator F_{UF} (solid), unimorph F_U (dotted), and flextensional actuator F_F (dashed).	45
3.10	Displacement for maximum blocking force design versus clearance ($L_a = 300 \mu\text{m}$): uniflex actuator w_{UF} (solid), unimorph w_U (dotted) and flextensional actuator w_F (dashed).	46
3.11	Aluminum cap thickness t_a for maximum blocking force design versus clearance ($L_a = 300 \mu\text{m}$): uniflex actuator (solid) and flextensional actuator (dashed).	47
4.1	T-beam actuator concept: (a) As fabricated and deflected shapes when voltage is applied between (b) both flanges and bottom electrodes, (c) web and bottom electrode, (d) left flange and bottom electrode, and (e) right flange and bottom electrode.	49
4.2	Web actuated cantilevered Tbeam: (a) Transverse deflection, and (b) electric field	51
4.3	T-beam model: (a) the initial and deflected shape (out-of-plane (top) and in-plane (bottom)) and (b) cross section.	52

4.4	Schematic illustration of T-beam fabrication: (a) start with 1mm thick bulk PZT-4 with Cr/Au coating, (b) dice to form web regions, (c) etch bottom electrodes, (d) spray photoresist pattern and evaporate Cr/Au for flange electrodes, (e) lift-off photoresist to form flange electrodes, (f) release individual T-beams by dicing.	59
4.5	Photograph of a fabricated and mounted T-beam (Device 4) actuator.	62
4.6	Photograph of experimental set-up to measure displacement and blocking force of T-beam actuators.	63
4.7	Applied electric field ϕ versus free tip out of plane displacement w_f for Device 3: Theoretical (solid - web actuation, dashed - flange actuation, dashdot - right or left flange actuation) and experimental (star - web actuation, diamond - flange actuation, square - left flange, and triangle - right flange).	65
4.8	Applied electric field, ϕ versus in-plane tip displacement, v_f for Device 3: theoretical (dashdot - Right flange (top), left flange (bottom)) and experimental (plus - left flange, circle - right flange).	66
4.9	Applied electric field ϕ versus tip force, F_3 for Device 3: Theoretical (solid - web actuation, dashed - flange actuation) and experimental (star - web actuation, diamond - flange actuation).	67
4.10	Non-dimensional voltage, V_2^* , V_3^* , versus displacement, v_f^* , w_f^* , for Devices 1 - 6: Theoretical (solid) and experimental (star - web actuation, diamond - flange actuation, square or plus - left flange, triangle or circle - right flange actuation).	68
4.11	Non-dimensional blocking force F_{3b}^* versus nondimensional voltage V_3^* for Devices 1 to 6: Theoretical (solid) and experimental (star - web actuation, diamond - flange actuation).	69
4.12	Contour plot of nondimensional displacement $(K_w)_{flange}$ versus b^* and t^* for PZT-4 material properties (Tab. 4.4)	72
4.13	Non-dimensional displacement K_w versus t^* for $b^*=0.381$ with PZT-4 material properties for web (theoretical - solid, experimental - star) and flange (theoretical - dashed, experimental - diamond) actuation.	74
4.14	Non-dimensional blocking force K_F versus b^* and t^*	75
4.15	Non-dimensional blocking force K_F versus t^* for $b^*=0.381$ for web (theoretical - solid and experimental - star) and flange (theoretical - dashed and experimental - diamond) actuation.	76
4.16	Non-dimensional energy parameter K_E versus b^* , t^*	77
4.17	Non-dimensional mechanical energy K_E versus t^* for $b^*=0.381$ (theoretical - black solid (web actuation) and black dashed (flange actuation), Experimental - star (web actuation) and diamond (flange actuation)) and $b^*=0.25$ (cyan)	78

4.18	Flange displacement coefficient $(w_c)_{flange}$ versus b^*, t^*	80
A.1	Clearance L_1 for maximum displacement versus length (L_a) : uniflex actuator with $t_a = 1 \mu\text{m}$ (dashed) and $t_a = 0.3 \mu\text{m}$ (dotted), and flextensional actuator with $t_a = 1 \mu\text{m}$ (dash-double dotted).	89
A.2	Ratio t_p/t_b for maximum displacement versus length L_a : uniflex actuator with $t_a = 1 \mu\text{m}$ (dashed) and $t_a = 0.3 \mu\text{m}$ (dotted), and unimorph actuator (dash-dotted).	90
A.3	Uniflex actuator ratio t_p/t_b for maximum displacement versus Al thickness t_a ($L_a = 300 \mu\text{m}$).	91
A.4	Maximum displacement versus length L_a : uniflex actuator $w_2(L)$ with $t_a = 1 \mu\text{m}$ (dashed) and $t_a = 0.3 \mu\text{m}$ (dotted), unimorph actuator $w_3(0)$ (dash-dotted), and flextensional actuator $w_2(L)$ with $t_a = 1 \mu\text{m}$ (dash-double dotted) and $t_a = 0.3 \mu\text{m}$ (double dash-dotted).	92
A.5	Blocking force F for maximum displacement configuration versus length L_a : uniflex actuator with $t_a = 1 \mu\text{m}$ (dashed) and $t_a = 0.3 \mu\text{m}$ (dotted), unimorph actuator (dash-dotted), and flextensional actuator with $t_a = 1 \mu\text{m}$ (dash-double dotted) and $t_a = 0.3 \mu\text{m}$ (double dash-dotted).	93
A.6	Clearance L_1 for maximum displacement versus length L_a : uniflex actuator with $t_a = 1 \mu\text{m}$ (dashed) and $t_a = 0.3 \mu\text{m}$ (dotted), and flextensional actuator with $t_a = 1 \mu\text{m}$ (dash-double dotted) and $t_a = 0.3 \mu\text{m}$ (double dash-dotted).	94
A.7	Al thickness t_a for maximum blocking force versus length L_a : uniflex actuator with clearance $L_1 = 2.7 \mu\text{m}$ (dashed) and $L_1 = 40 \mu\text{m}$ (dotted), and flextensional actuator with $L_1 = 2.7 \mu\text{m}$ (dash-double dotted).	95
A.8	Ratio t_p/t_b for maximum blocking force versus length L_a : uniflex actuator with clearance $L_1 = 2.7 \mu\text{m}$ (dashed) and $L_1 = 40 \mu\text{m}$ (dotted), and unimorph actuator (dash-dotted).	96
A.9	Uniflex actuator ratio t_p/t_b for maximum blocking force versus clearance L_1 for $L_a = 300 \mu\text{m}$	97
A.10	Maximum blocking force F versus length L_a : uniflex actuator with clearance $L_1 = 2.7 \mu\text{m}$ (dashed) and $L_1 = 40 \mu\text{m}$ (dotted), unimorph actuator (dash-dotted), and flextensional actuator with $L_1 = 2.7 \mu\text{m}$ (dash-double dotted) and $L_1 = 40 \mu\text{m}$ (double dash-dotted).	98
A.11	Displacement for maximum blocking force configuration versus length L_a : uniflex $w_2(L)$ with clearance $L_1 = 2.7 \mu\text{m}$ (dashed) and $L_1 = 40 \mu\text{m}$ (dotted), unimorph actuator $w_3(0)$ (dash-dotted), and flextensional actuator $w_2(L)$ with $L_1 = 2.7 \mu\text{m}$ (dash-double dotted) and $L_1 = 40 \mu\text{m}$ (double dash-dotted).	99

A.12	Al thickness t_a for maximum blocking force versus length L_a : uniflex with clearance $L_1 = 2.7 \mu\text{m}$ (dashed) and $L_1 = 40 \mu\text{m}$ (dotted), and flextensional actuator with clearance $L_1 = 2.7 \mu\text{m}$ (dash-double dotted) and $L_1 = 40 \mu\text{m}$ (double dash-dotted).	100
B.1	Applied electric field ϕ versus free tip out of plane displacement w_f for Device 1: Theoretical (solid - web actuation, dashed - flange actuation, dashdot - right or left flange actuation) and experimental (star - web actuation, diamond - flange actuation, square - left flange, and triangle - right flange).	102
B.2	Applied electric field, ϕ versus in-plane displacement tip displacement, v_f for Device 1: theoretical (dashdot - Right flange (top), left flange (bottom)) and experimental (plus - left flange, circle - right flange). . . .	102
B.3	Applied electric field ϕ versus tip force, F_3 for Device 1: Theoretical (solid - web actuation, dashed - flange actuation) and experimental (star - web actuation, diamond - flange actuation).	103
B.4	Applied electric field ϕ versus free tip out of plane displacement w_f for Device 2: Theoretical (solid - web actuation, dashed - flange actuation, dashdot - right or left flange actuation) and experimental (star - web actuation, diamond - flange actuation, square - left flange, and triangle - right flange).	103
B.5	Applied electric field, ϕ versus in-plane displacement tip displacement, v_f for Device 2: theoretical (dashdot - Right flange (top), left flange (bottom)) and experimental (plus - left flange, circle - right flange). . . .	104
B.6	Applied electric field ϕ versus tip force, F_3 for Device 2: Theoretical (solid - web actuation, dashed - flange actuation) and experimental (star - web actuation, diamond - flange actuation).	104
B.7	Applied electric field ϕ versus free tip out of plane displacement w_f for Device 4: Theoretical (solid - web actuation, dashed - flange actuation, dashdot - right or left flange actuation) and experimental (star - web actuation, diamond - flange actuation, square - left flange, and triangle - right flange).	105
B.8	Applied electric field, ϕ versus in-plane displacement tip displacement, v_f for Device 4: theoretical (dashdot - Right flange (top), left flange (bottom)) and experimental (plus - left flange, circle - right flange). . . .	105
B.9	Applied electric field ϕ versus tip force, F_3 for Device 4: Theoretical (solid - web actuation, dashed - flange actuation) and experimental (star - web actuation, diamond - flange actuation).	106

B.10 Applied electric field ϕ versus free tip out of plane displacement w_f for Device 5: Theoretical (solid - web actuation, dashed - flange actuation, dashdot - right or left flange actuation) and experimental (star - web actuation, diamond - flange actuation, square - left flange, and triangle - right flange).	106
B.11 Applied electric field, ϕ versus in-plane displacement tip displacement, v_f for Device 5: theoretical (dashdot - Right flange (top), left flange (bottom)) and experimental (plus - left flange, circle - right flange). . . .	107
B.12 Applied electric field ϕ versus tip force, F_3 for Device 5: Theoretical (solid - web actuation, dashed - flange actuation) and experimental (star - web actuation, diamond - flange actuation).	107
B.13 Applied electric field ϕ versus free tip out of plane displacement w_f for Device 16: Theoretical (solid - web actuation, dashed - flange actuation, dashdot - right or left flange actuation) and experimental (star - web actuation, diamond - flange actuation, square - left flange, and triangle - right flange).	108
B.14 Applied electric field, ϕ versus in-plane displacement tip displacement, v_f for Device 6: theoretical (dashdot - Right flange (top), left flange (bottom)) and experimental (plus - left flange, circle - right flange). . . .	108
B.15 Applied electric field ϕ versus tip force, F_3 for Device 6: Theoretical (solid - web actuation, dashed - flange actuation) and experimental (star - web actuation, diamond - flange actuation).	109

List of Tables

2.1	Parameters for uniflex actuator	27
2.2	Uniflex actuator blocking force experimental data and theoretical predictions	33
2.3	Uniflex* actuator displacement amplification over unimorph actuator for PZT thickness $t_p = 1.4 \mu\text{m}$, Si_3N_4 thickness $t_b = 1 \mu\text{m}$, and Aluminum thickness* $t_a = 1 \mu\text{m}$ at 10 V	33
4.1	Electromechanical coefficients for web and flange actuation	54
4.2	Cross-sectional area, first moment of area, and second moment of area for web, flange and, single flange actuation	56
4.3	Fabricated prototype parameters	61
4.4	PZT-4 material properties	64

Acknowledgments

I would like to thank my advisors Dr. Christopher Rahn and Dr. Srinivas Tadigadpa for their excellent mentoring and support throughout my Ph.D program. Without their timely advice and direction it is impossible to completed this humongous task.

I would like to thank the wonderful committee members Dr. Ashok D. Belegundu, Dr. Christopher L. Muhlstein, and Dr. M. Amanul Haque for taking time of their busy schedules and providing valuable suggestions.

I would like to thank Han G. Yu for fabricating the uniflex prototypes and providing the experimental data. This work is also supported by the Pennsylvania State University Materials Research Institute NanoFabrication Network and the National Science Foundation Cooperative Agreement No. 0335765, National Nanotechnology Infrastructure Network, with Cornell University. Any opinions, findings, and conclusions or recommendations expressed do not necessarily reflect the views of Cornell University nor those of the National Science Foundation. I would like to thank Kiron Mateti for fabricating the T-beam prototypes which enabled me to experimentally measure the T-beam performance. Also, I would like to thank the Air Force Office of Scientific Research and Dr. Victor Giurgiutiu for their support of this work under grant # FA9550-07-1-0367.

I would like to thank "The Mechanical and Nuclear Engineering Department" and

”The Pennsylvania State University” for giving me this great opportunity.

I am very lucky to have great friends and labmates who are always available, whenever, I need help. I would like to thank Deepak, Kiron, Amir, Andy, Thomas, Paul, Ying, and Lloyd for their support and having fun time together. I would like to thank my loving parents for supporting my decision to take up this challenging task.

Finally, I would like to dedicate this work to my loving wife, Vijitha, for her love, motivation, and continuous support.

Chapter 1

Introduction

The past few years have seen significant improvement in the commercial applications for electro-mechanical actuators. Piezoelectric electro-mechanical actuators provide a seamless way to convert electrical and mechanical energy back and forth thereby, providing lot of scope, for energy harvesting and actuation.

The challenge of piezoelectric actuation is the amplification of small strain (0.1%) to produce reasonable displacement. Most piezoelectric actuators use Lead Zirconate Titanate (PZT) because it provides large piezoelectric and electro-mechanical coupling factors [1, 2]. To produce reasonable motion, however, the piezoelectric strain must be amplified. Several amplification mechanisms are studied by various researchers. Some of the designs and their applications are presented in the following sections.

1.1 Applications

Piezoelectric actuators are extensively used in commercial products at the macroscale. High performance V-stack actuators are used for control of high aspect ratio wings in uninhabited air vehicles [3]. Properly designed actuators provide active control of helicopter rotors with improved vibration control and stability [4, 5, 6, 7, 8]. Naval applications like low frequency piezoelectric SONAR devices having lower weight and higher portability are reported in [9]. Piezoelectric actuators are also used in adaptive optics to produce deformable mirrors [10] because of its low voltage actuation and capability of miniaturization. Piezoelectric actuated auto focus lenses enable scanners to read the barcode at much longer distances [11, 12].

Micro-feed stages and multi degree of freedom micro manipulators driven by piezoelectric actuators enable ultra-precision positioning of 0.001 to 0.01 μm because of their fine displacement resolution and no friction [13, 14]. There is a lot of research going on for application to acoustic transducers like microphone and micro speakers [15, 16]. The piezoelectric cantilevered microphones are found to be more sensitive and stress free when compared to the conventional microphones [17, 18]. Disk type piezoelectric actuators have wide applications in micro pumps for micro pump driver [19] and fuel drop generation in automobiles [20]. Recently, piezoelectric cymbal actuators are reported for micro-flow applications [21]. Cantilevered piezoelectric unimorph actuators are extensively used in RF switches [22, 23, 24] because of better isolation and low insertion loss from DC to 50 GHz.

1.2 Macroactuators

Various designs are invented by different researchers to enable reasonable strain amplification and also obtain required blocking force. Stack actuators [25, 26, 27] produce larger motions at low voltages by stacking electroded thin PZT disks and actuating through the thickness. In this case, the material poling, applied voltage and displacement are all in the same direction. Adjacent disks have opposite poling and field directions. This makes use of the d_{33} piezoelectric coefficient which is much larger than the d_{31} coefficient ($\sim 1/3$ of d_{33}) used in unimorph or bimorph actuators. The stack actuators are modeled [27, 28], compared [25], optimized for maximum energy output [26], and to many specific applications like V-stack actuator [3]. Further displacement amplification with four bar linkages and stack actuators is reported to provide flapping action for flying insect robots [29, 30]. Stack actuators are capable of producing very high force but displacement is limited by number of layers that can be fabricated to operate at reasonable voltages and size of actuator.

Unimorph actuators use the compliant bending mechanism to amplify the displacement, using the d_{31} piezoelectric coefficient [27, 31]. The unimorph has a PZT layer poled through the thickness and a passive layer bonded to it. The PZT layer expands through the thickness and contracts longitudinally when an electric field is applied in the poling direction between the electrodes placed on top and bottom of piezoelectric layer. The longitudinal contraction causes the unimorph to bend due to the constraining passive layer (like silicon nitride). Static and dynamic models to predict displacement,

blocking force, resonant frequencies [27, 32], and electro-mechanical coupling factors and output efficiencies [31, 33] are studied by various researchers .

To improve the displacement further, both the layers of unimorph can be made of active piezoelectric material, polarized in the same direction. For one of the layers the voltage is applied in the direction of poling and opposite for another layer. The first layer contracts while the second layer expands in length resulting in very high transverse displacement [27, 32]. The maximum applied field in the opposite direction of poling is limited to $\sim 1/3$ of the positive field to prevent depoling of the PZT. The force produced by such a structure is higher than the unimorph alone for the same applied field. Also, multimorphs consisting of cantilevers with multiple layers of PZT and passive layers are also reported [34, 35, 36]. Tube actuators that produce bimorph actuation in two directions have been demonstrated at the macroscale [37].

Flextensional actuators [38, 39] have a bulk PZT with a metallic cap bonded at the ends. When the PZT is actuated, the d_{31} actuation causes the bulk PZT to contract in length and the cap flexes producing displacement. One of such popular macroscale actuator is flextensional Moonie actuator which uses the flexural motion of the cap [38], whereas the cymbal actuator uses both flexural and rotation motions [40, 41, 42]. Cymbal actuators are also fabricated with lead free piezo-ceramic materials [43, 44, 45]. Displacement, resonance frequency [46, 47] and the effective piezoelectric coefficient [48] characteristics of these actuators are extensively studied. Some researchers used topology optimization to obtain optimum flextensional designs for displacement and

blocking output [49].

Another kind of novel actuator called "drum actuator" consists of a circular disc, with brass membrane attached at the circular end as in a drum. PZT layer is attached to the brass membrane and when actuated produces flexural motion of brass and PZT layers using d_{31} piezoelectric coefficient [50, 51].

1.3 Microactuators

At the microscale, however, piezoelectric actuators are difficult to fabricate. Although solder bonding techniques for PZT have been reported [52] stack actuators of more than a few layers have not been fabricated.

Some researchers used low performance AlN or ZnO piezoelectric materials [53] to produce flextensional actuators. These micro-scale flextensional actuators can operate in ultrasound frequencies unlike their macro scale counter parts [54]. Considerable analytical and experimental research is done about the applicability of these micro flextensional actuators to ultrasound [55, 56] and high resolution ink-jet printing applications [53, 57] using the thin plate theory and Mindlin plate theory.

Recently, using thin film and solder bonding techniques, researchers have fabricated microscale piezoelectric unimorph [32] and flextensional [58] actuators. Thin film PZT actuators are successfully implemented for precision alignment of fibre-optic cables [59] and circular unimorph disks for micropump applications [60]. There is also considerable interest in fabricating piezoelectric thin film actuators using micromachining [61, 62].

Micromachined cantilevered unimorph and bimorphs are extensively studied for RF applications [63, 64]. Micromachined multimorphs are explored for micro-optic applications [65]. Conventional silicon chip manufacturing process uses spinning to deposit photoresists. To reduce the wastage during the process, micro machined actuators are studied for spinless resist deposition [66]

The PZT thin films that have been demonstrated, however, do not have the quality of bulk PZT [67] and stress mismatch between the layers during the fabrication, results in variably defected structures upon release. So the performance of piezoelectric microactuators can be improved. Also novel designs that can further amplify displacement will greatly increase the applicability of these actuators.

1.4 Current Research

This research describes the design, modeling, and optimization of a piezoelectric uniflex microactuator and a T-beam actuator. The uniflex actuator combines the actuation mechanisms of a unimorph and flextensional actuator. A flexural aluminum cap is attached at the ends of a unimorph to form a uniflex actuator. The unimorph bends and the cap flexes to amplify the small strain of piezoelectric material and produce relatively large displacement. Prototypes are fabricated using photolithography and thin film deposition techniques. Physics based analytical models are developed to predict displacement and blocking force as functions of the applied voltage and force. The models are validated against the experimental data[68]. The uniflex designs that maximize displacement and

blocking force are discussed in detail based on experimentally validated models.

Also, this research introduces a novel monolithic microactuator that can be fabricated from bulk PZT by micro-machining using an Inductive Coupled Plasma-Reactive Ion Etching (ICP- RIE) [69] or by dicing. Using this process, a two axis unimorph can be fabricated from a bulk PZT wafer. This T-beam actuator is fabricated and experimentally shown to produce both out-of-plane and inplane displacements. Analytical models are built to predict the displacement and blocking force and validated using experimental models. Prototypes are fabricated using dicing for detailed parametric studies. Model-based analysis shows that the T-beam actuator geometry can be optimized to produce large displacement and blocking force. Specific configurations that maximize displacement, blocking force, and mechanical energy are discussed in detail.

1.5 Organization of the Dissertation

Chapter 2 discusses about the design, fabrication, and modeling of uniflex microactuator. Chapter 3 discusses in the detail the optimization of uniflex actuator. Chapter 4 introduces the concept of novel T-beam micro-actuator. Analytical modeling, experimental validation and optimization are discussed in detail. Chapter 5 concludes with the results from uniflex and T-beam actuators analysis. Also, future research ideas are presented.

Design, Fabrication, and Performance of a Piezoelectric Uniflex Microactuator

2.1 Introduction

In this chapter the design, fabrication and performance of piezoelectric microactuator is discussed. The uniflex actuator combines the amplification methods of unimorph and flextensional actuators. The unimorph bends and the cap flexes to amplify the small strain of piezoelectric material and produce relatively large displacements. A detailed model that predicts the displacement and blocking force of uniflex actuators as a function of the applied voltage is presented.

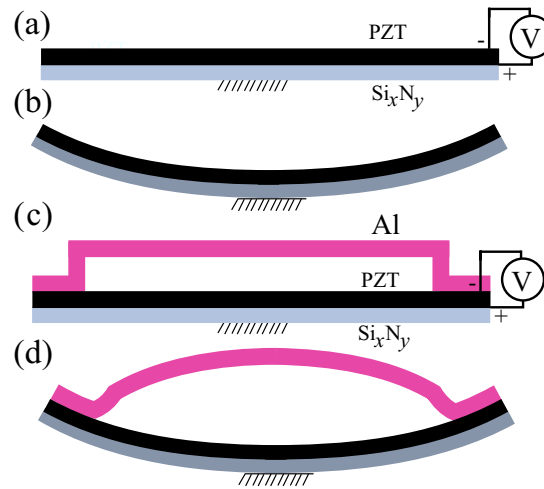


Figure 2.1. Schematic representation of the (a) PZT Unimorph Actuator at 0 V and (b) at finite drive voltage V, (c) Uniflex actuator at 0 V and (d) Uniflex actuator at a finite drive voltage V.

2.2 The Uniflex Actuator

Fig. 2.1(a and b) illustrate schematically the construction and operation of unimorph actuator. The unimorph actuator has a bottom layer of passive Si_xN_y and a top layer of $\text{PbZr}_{0.52}\text{Ti}_{0.48}\text{O}_3$ (PZT). The PZT is poled through the thickness and electroded on top and bottom. Voltage is applied in the poling direction, causing d_{31} contraction of the PZT and upward bending of the unimorph. Fig. 2.1(c and d) show a schematic diagram of a uniflex actuator. The uniflex actuator consists of a unimorph that is supported by a bridge structure at the center and an Al cap that is bonded at the ends of the unimorph. The Al cap is bent away from the unimorph such that there is a small gap between the cap and unimorph over most of the length. When the unimorph is actuated, the Al cap is compressed by the unimorph and, if correctly designed, buckles upward. Thus, the uniflex actuator combines unimorph and flexural displacement amplification mech-

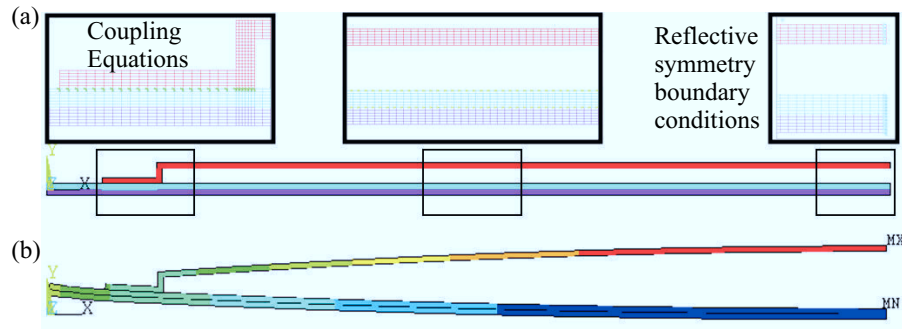


Figure 2.2. Finite element model of uniflex actuator: (a) Initial, and (b) after deflection.

anisms to produce large vertical displacement at the center of the Al cap. Figure 2.2(a) shows the two dimensional half sector finite element model of uniflex actuator. ANSYS PLANE13 coupled field elements are used to model the active piezoelectric material (PZT). PLANE 42 elements with plane stress option are used to model the base silicon nitride of unimorph and the flexural aluminum cap. Aluminum cap is attached to the unimorph by writing the coupling equations $(u_x)_{Al} = (u_x)_{PZT}$, and $(u_y)_{Al} = (u_y)_{PZT}$ at the interface (shown in light green), where u_x and u_y are the deflections in horizontal and vertical directions. Reflective symmetry boundary conditions are applied at the right end for both unimorph, and aluminum cap. Figure 2.2(b) shows the deflected shape of uniflex actuator when voltage is applied between top and bottom layers of PZT. The deflected configuration shows that uniflex design works as expected.

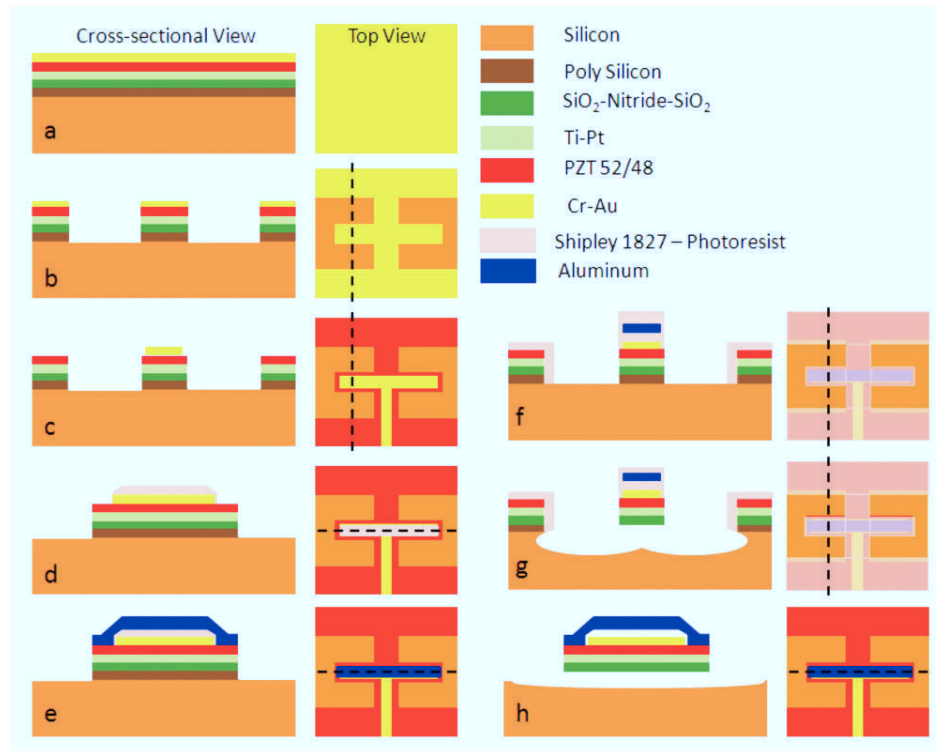


Figure 2.3. Schematic (not to scale) illustration of the fabrication process. Cross-sectional view corresponds to the dotted line on top view. (a) Deposit PolySi/SiO₂-Si₃N₄-SiO₂/Ti-Pt/PZT/Cr-Au, (b) Apply photoresist and pattern the PZT unimorph stack and RIE etch through PolySi, (c) Apply photoresist and pattern Cr-Au layer for top electrode via wet etching, (d) Deposit 2.7 μm thick photoresist (Shipley 1827) for sacrificial layer and pattern, (e) Deposit Al for cap structure, pattern, and etch, (f) Pattern photoresist to prevent unwanted undercutting during release step, (g) Release actuator structure using XeF₂ isotropic etching while other surfaces are covered by photoresist for protection from XeF₂, (h) Release flexural (Al cap) structure with acetone/IPA/Methanol.

2.3 Fabrication of the Uniflex Actuator

The micromachined uniflex actuator uses a PZT unimorph actuator as the active element with a secondary metal flexural element. The major fabrication process steps shown in Fig. 2.3 include (i) the preparation of substrate wafers, (ii) deposition of the PZT film, (iii) patterning the active structure, (iv) fabrication of the metal flexural structure, and

(v) the final release. A total of five photolithographic steps were used in the fabrication of the uniflex microactuator.

On single side polished, (100) silicon wafers, the stack of sacrificial and structural layers were deposited as follows (i) 0.5 μm thick polysilicon (low pressure chemical vapor deposition (LPCVD) process using SiH_4 at 620 $^\circ\text{C}$ for 2 hours) as sacrificial layer, (ii) 0.1 μm thick silicon oxide (plasma enhanced chemical vapor deposition (PECVD) using N_2 , SiH_4 , and N_2O , radio frequency (RF) power of 300 W at 2 Torr, 400 $^\circ\text{C}$) as protection layer, (iii) 0.8 μm thick low stress (~ 200 MPa tensile) silicon nitride (LPCVD using SiCl_2H_2 and NH_3 , 170 mTorr; 850 $^\circ\text{C}$, 4 hours) as the passive unimorph layer, (iv) 0.1 μm thick silicon oxide (plasma enhanced chemical vapor deposition (PECVD) using N_2 , SiH_4 , and N_2O , RF power of 300 W at 2 Torr, 400 $^\circ\text{C}$) as adhesion promotion layer and (v) 20nm/100nm thick Ti/Pt (sputtered at 300 $^\circ\text{C}$ with RF/direct current power of 200 W at 5 mTorr) as bottom electrode layer were deposited in the sequence described. Sol-gel lead zirconate titanate (PZT) with Zr/Ti ratio of 52/48 (PZT solution was spun at 1500 rpm for 30 seconds and two pyrolysis steps at 300 $^\circ\text{C}$ and 450 $^\circ\text{C}$ for 60 seconds each followed by 60 seconds crystallization at 700 $^\circ\text{C}$ resulting in a 0.2 μm thick PZT film) were used as the active unimorph layer. Several repetitions of these steps are required to obtain the desired thickness. A complete description of the preparation and characterization of the PZT films is given elsewhere [70]. After the deposition of the PZT film, 20 nm/200 nm thick Cr/Au (electron beam evaporation at 10^{-7} Torr) as top electrode layer completed the stack formation.

The first photolithography step is the patterning of photoresist for the definition of the unimorph structure in PZT. An electroplated nickel mask was used for this etching of the entire stack down to the silicon substrate using an inductively coupled plasma reactive ion etch (ICP RIE) process. In the physical etching mode, the ICP RIE etched PZT at a rate of 0.17 to 0.2 $\mu\text{m}/\text{min}$, with the condition of 2000 W and 475 W for the source and substrate powers respectively with an Ar flow rate of 50 sccm. By adding 10 sccm of SF_6 , the etch rate could be increased by $\sim 0.4 \mu\text{m}/\text{min}$ [71]. Shipley 1827 and benzocyclobutene (BCB) photoresists can be used for masking when only Ar gas was used but in our work we found that these masks could not reliably withstand the 5-10 minute etch process upon the addition of 10% SF_6 . Therefore, we used Ni hard mask which provided better yield as well as selectivity with respect to etching the stack. This was followed by the patterning of the top Cr/Au electrode using standard wet etching method.

For fabrication of the flexural structure, Shipley 1827 positive photoresist was chosen as the sacrificial material and thus only resist exposure and development steps were required. The thickness of this sacrificial photoresist layer was 2.7 μm . This was followed by the sputtering of required thickness of aluminum and the final lithography step to define the flexural element. Aluminum was wet etched. The device was once again spin coated with photoresist and a protection mask was used to open up areas to be etched in XeF_2 vapor phase etching as shown in 2.3(f). The uniflex structure was released by isotropically etching polysilicon and substrate as shown schematically

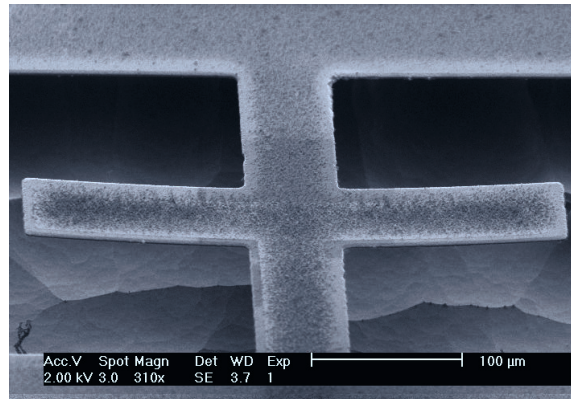


Figure 2.4. Photograph of a fabricated unimorph.

in 2.3(g). The use of polysilicon sacrificial layer, which etches much more rapidly in XeF_2 than single crystal substrate silicon, coupled with the photoresist protection mask prevented excessive lateral undercutting of the anchor areas and guaranteed complete release of the actuator structure with a relatively short etch time in XeF_2 . The sacrificial and protective layers of photoresist were finally removed in acetone followed by an IPA/methanol rinse for achieving stiction free release. Figures 2.4 and 2.5 show the fabricated unimorph and uniflex devices.

2.4 Uniflex Actuator Performance

After fabrication and release, the devices were placed in a dual in-line package (DIP). Electrical connections were made via conventional ball wire bonding, and the packaged MEMS were mounted in a zero insertion force (ZIF) socket. Uniflex actuators with two different thicknesses of the PZT layer ($1 \mu\text{m}$ and $1.4 \mu\text{m}$) and aluminum caps layer (1

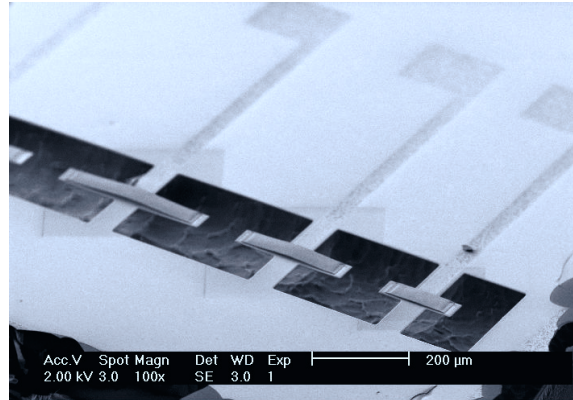


Figure 2.5. Photograph of the fabricated uniflex actuator array.

μm and $2 \mu\text{m}$) resulting in 4 different configurations were fabricated. 200, 300, 400 and $500 \mu\text{m}$ long uniflex actuators in each configuration were measured for their static deflection and blocking force characteristics. These measurements were accomplished using a white light interferometer and a nanoindenter and are described in detail.

2.4.1 Static Displacement Measurement

Measurements of the static displacement as a function of applied voltage were performed using a Zygo NT-100 white light interference microscope. Prior to making any displacement measurements, the devices were poled using 10 V (equivalent to 100 kV/cm) for 20 mins and were actuated 5 to 6 times to remove any initial hysteresis. The effectiveness of this treatment was based upon achieving stable and reproducible voltage deflection curves from the actuators. Stable displacement curves as a function of voltage in the 0 - 10 V range in 1 V steps for each uniflex length were obtained for both increasing and decreasing voltage cycles. Figure 2.6 shows the initial and the actuated shape of

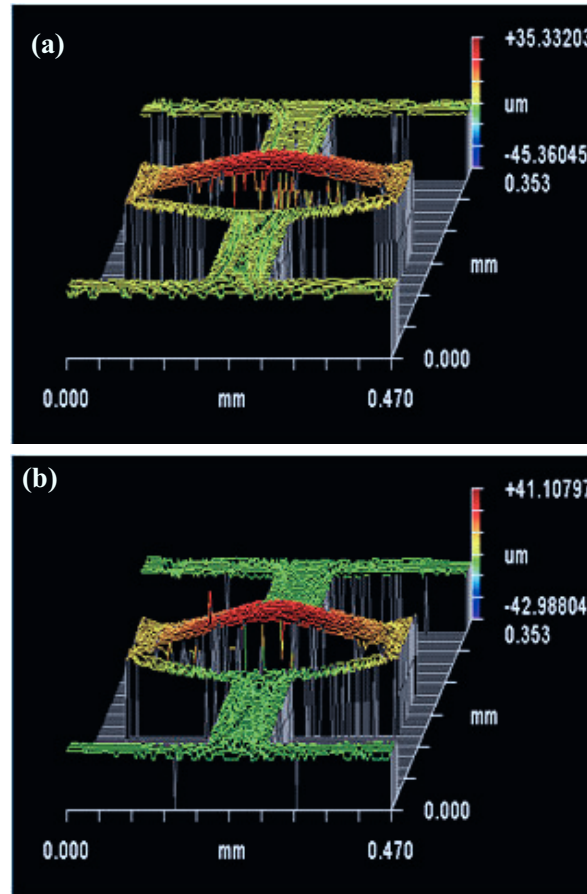


Figure 2.6. Zygo image of a 400 μm long flextensional actuator with (a) no bias and (b) bias of 10 V. 4.16 μm of displacement was measured. The displacement is the difference in the height of the aluminum cap with respect to the PZT actuator between the two cases.

a 400 μm long flextensional actuator with 1 μm thick PZT and 1 μm thick aluminum cap configuration. It shows that the released structure has an initial curvature due to the larger tensile stress in the PZT layer in comparison to the 0.8 μm thick low-stress silicon nitride passive layer. Deflection of the actuator was measured as the position of the top of the aluminum cap with respect to the PZT unimorph actuator at the mid-point of the structure (point of maximum deflection). This definition of deflection makes it

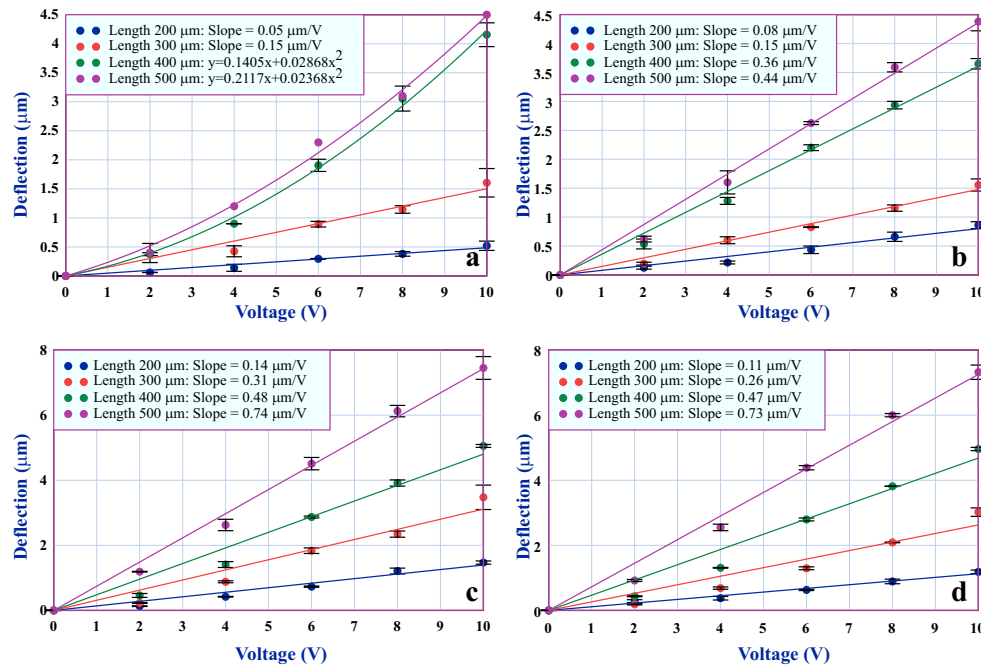


Figure 2.7. Actuator deflection as a function of applied voltage for various lengths of the actuator and for (a) 1 μm thick PZT and 1 μm thick Al cap, (b) 1 μm thick PZT and 2 μm thick Al cap, (c) 1.4 μm thick PZT and 1 μm thick Al cap, (d) 1.4 μm thick PZT and 2 μm thick Al cap.

impervious to any offsets or motion of the freestanding anchor point of the actuator. For the device shown in Fig. 2.6, a displacement of 4.16 μm was obtained for 10 V applied bias.

Figure 2.7 shows the deflection curves for the four configurations and for the four lengths of the actuators. As expected, the deflection of all the actuators shows a linear dependence on the drive voltage except for two actuators in Fig. 2.7(a). This unusual deflection characteristics might be due to material imperfections in the PZT films or due to unanticipated structural defects in these specific actuators.

2.4.2 Blocking Force Measurement

The blocking force measurements were performed in a Hysitron, Inc. TriboIndenter operating in laboratory air ($\sim 22 \pm 2$ °C, ~ 50 % R.H.). Electrical connections to the devices (via the ZIF socket) were routed through the TriboIndenter acoustic housing to insure a low vibration environment during testing. Prior to testing, the positions of the samples were identified in the optical video image, and the coordinates of the ends of the flexures were noted (± 2 μm , typical). The positions of the centers of the devices were then calculated, thereby insuring precise alignment of the measurement location. Initial poling of devices was then performed at $3E_c$ (7.5 V) for 20 minutes with an Agilent E3612A DC power supply. A 500 nm radius, diamond, spheroconical indenter was then placed on the surface of the aluminum flexure with a contact force of 1.5 μN . The use of a large, blunt indenter insured that contact between the tip and the device did not induce damage. The TriboIndenter was then allowed to stabilize for 1 hour to minimize the effects of thermal drift on measurement accuracy.

After stabilization, a series of blocking force measurements were performed. The TriboIndenter was used to apply a displacement-controlled, trapezoidal waveform, and the blocking force measurements were made during the constant position portion of the test. At the start of each test, the thermal drift in the system was monitored for 60 seconds, and a least squares, linear fit of the drift rate for the last 30 seconds of the monitoring period was used to correct all data (typical drift rates were ~ 0.005 nm/s with a maximum allowable rate of 0.1 nm/s). The indenter tip was then linearly ramped at

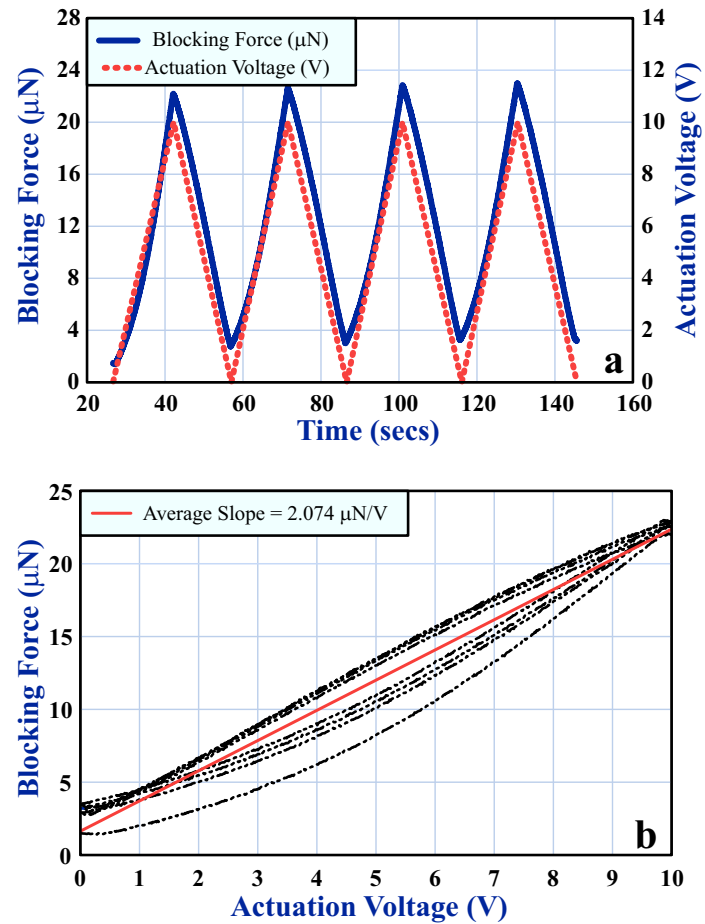


Figure 2.8. (a) Blocking force raw data obtained using the nanoindenter for $300 \mu\text{m}$ long actuator with $1 \mu\text{m}$ thick PZT and $1 \mu\text{m}$ thick Al cap. (b) The data is converted into a voltage-blocking force graph showing the hysteresis actuation behavior of the actuator.

2.5 nm/s to an initial displacement of 25 nm. This linear ramp was followed by a 40, 70, 130, or 250 second period where the position was held constant. During this hold period a 0 to 10 V, triangular ramp waveform at 34 mHz was applied with an Agilent 33120A arbitrary waveform generator. The number of applied voltage cycles was 1, 2, 4, and 8 for the 40, 70, 130, and 250 second hold periods, respectively. Figure 2.8(a) shows the raw blocking force data obtained as a function of time for actuator $300 \mu\text{m}$ long actuator

with 1 μm thick PZT and 1 μm thick Al cap. This data is converted into a voltage versus blocking force data as shown in Fig. 2.8(b). The hold period was then followed by the withdrawal of the diamond tip at a rate of 2.5 nm/s. The force and displacement data were measured continuously throughout the test with the personal computer controlled data acquisition system, and were saved to file for evaluation.

2.5 Mathematical Modeling

The uniflex actuator shown in Fig. 2.9(a) is modeled as an assembly of beams 1, 2, and 3 as shown in Fig. 2.9(b). Beam 3 is the unimorph and beams 1 and 2 are the support leg and span of the aluminum cap, respectively. We assume symmetric loading (mid-span point load), so a half span model with a reflective symmetric boundary condition at the right boundary of the cap is used. The cartesian coordinates, x_i and z_i ($i = 1, 2, 3$) shown in Fig. 2.9(b) denote the horizontal and vertical positions of the material particles, for the three beams. Figure 2.9(c) shows the deflected structure with centroidal displacements u_i and w_i in the x_i and z_i directions, respectively. The thickness dimensions t_a , t_p and t_b correspond to the Al cap, PZT, and Si_xN_y , respectively. Beams 3 and 2 have length L and L_1 is the length of beam 1 or the clearance between beam 2 and beam 3. The actuator length $L_a = 2L + 40 \mu\text{m}$ includes the $20 \mu\text{m}$ clamped region at the ends of the structure that contribute to the length of the actuator but not the displacement.

The three beams have eighteen boundary conditions. Beam 3 is clamped at the right end and fixed via a torsional spring of stiffness K_t at the left end to beam 1. Geometri-

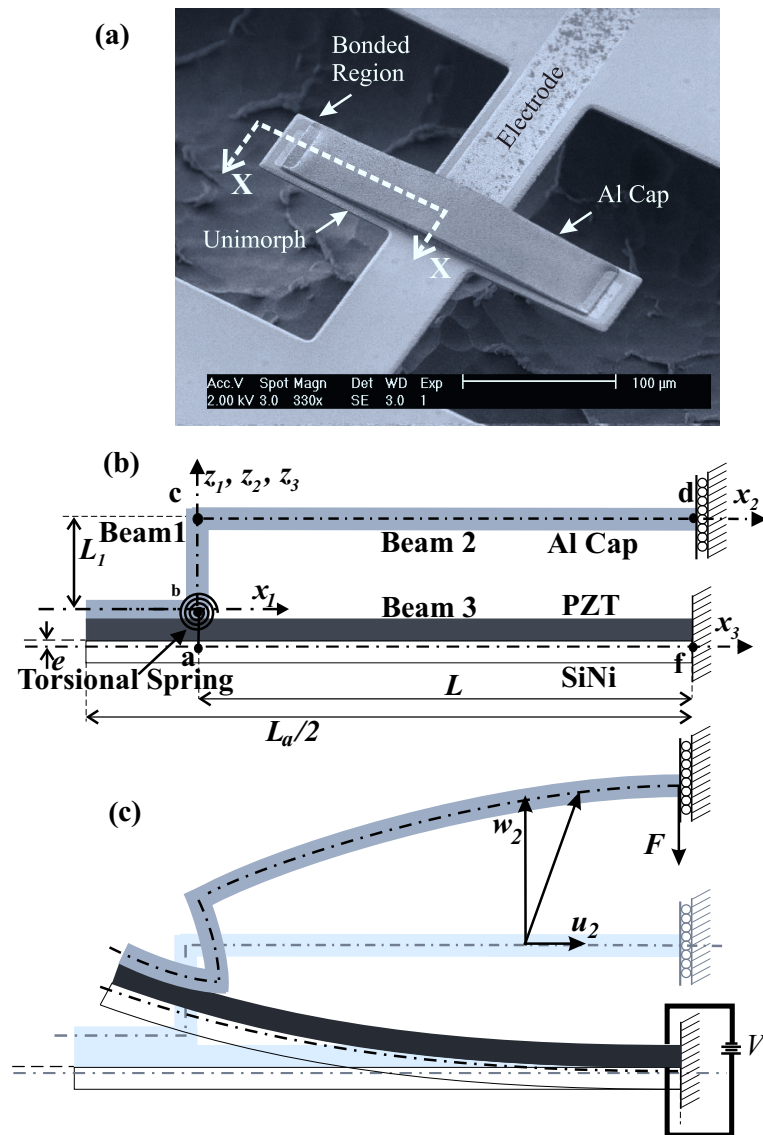


Figure 2.9. Photograph (a) and X-X cross-section schematic of the initial (b) and deflected (c) unimorph actuator.

cally exact modeling of the unimorph actuator requires a rigid connection between beams 1 and 3 or $K_t = \infty$. However, the weakened connection associated with $K_t < \infty$ is found to more accurately predict the experimentally measured displacement and blocking force

of the uniflex actuator. Beam 2 is clamped to beam 1 at the left end and guided at the right end. The governing equations and the boundary conditions for static operation are obtained using the principle of virtual work. The potential energy for the structure is [32]

$$\begin{aligned}
U_1 &= \int_{V_1} \frac{E_1}{2} \left(\frac{\partial w_1(z_1)}{\partial z_1} - x_1 \left(\frac{\partial^2 u_1(z_1)}{\partial z_1^2} \right) \right)^2 dV, \\
U_2 &= \int_{V_2} \frac{E_2}{2} \left(\frac{\partial u_2(x_2)}{\partial x_2} - z_2 \left(\frac{\partial^2 w_2(x_2)}{\partial x_2^2} \right) \right)^2 dV, \\
U_3 &= \int_{V_b} \frac{E_b}{2} \left(\frac{\partial u_3(x_3)}{\partial x_3} - z_3 \left(\frac{\partial^2 w_3(x_3)}{\partial x_3^2} \right) \right)^2 dV \\
&\quad + \int_{V_p} H dV, \\
U_{TS} &= \frac{K_t}{2} \left(\frac{dw_1(0)}{dx_1} - \frac{du_1(0)}{dz_1} \right)^2, \\
U &= U_1 + U_2 + U_3 + U_{TS},
\end{aligned} \tag{2.1}$$

where $E_1 = E_2$, E_p and E_b are the Young's moduli of Al, PZT and Si_xN_y, respectively, V_1 , V_2 , V_p and V_b are volumes of beam 1, beam 2, PZT and Si_xN_y layers of beam 3, respectively, U_1 , U_2 , U_3 , U_{TS} are the potential energy of beam 1, beam 2, beam 3, and the torsional spring, respectively, and U is the total potential energy of the actuator. The

electric enthalpy H for the piezoelectric material is [32]

$$\begin{aligned}
H = & \frac{E_p}{2} \left(\frac{\partial u_3(x_3)}{\partial x_3} \right)^2 + \frac{e_{31}V}{2t_p} \frac{\partial u_3(x_3)}{\partial x_3} \\
& + \left(\frac{1}{2} \left[E_p + \frac{e_{31}^2}{\epsilon_{33}} \right] z_3^2 - \frac{e_{31}^2(2e-t_p)^2}{8\epsilon_{33}} \right) \\
& \left(\frac{\partial^2 w_3(x_3)}{\partial x_3^2} \right)^2 - \frac{e_{31}V}{2t_p} (2e-t_p) \frac{\partial^2 w_3(x_3)}{\partial x_3^2} \\
& - \frac{\epsilon_{33}V^2}{2t_p^2} + \left(\frac{e_{31}^2(2e-t_p)}{2\epsilon_{33}} - \left[E_p + \frac{e_{31}^2}{\epsilon_{33}} \right] z_3 \right) \\
& \frac{\partial^2 w_3(x_3)}{\partial x_3^2} \frac{\partial u_3(x_3)}{\partial x_3},
\end{aligned} \tag{2.2}$$

where e_{31} is piezoelectric stress coefficient, ϵ_{33} is the permittivity of PZT, V is the potential difference between top and bottom layers of PZT, and e is the distance between the centroid of beam 3 and the PZT/Si_xN_y interface [32] given by

$$e = \left(\frac{t_b}{2} \right) \left(\frac{\frac{E_b}{E_p} - \left(\frac{t_p}{t_b} \right)^2}{\frac{E_b}{E_p} + \frac{t_p}{t_b}} \right). \tag{2.3}$$

Substitution of Eqs. (2.1) into the principal of virtual work, $\int_0^t (\delta U + F \delta u_2(L,t)) dt = 0$, produces the boundary conditions and field equations

$$\frac{d^2 w_1(z_1)}{dz_1^2} = 0, \quad \frac{d^4 u_1(z_1)}{dz_1^4} = 0, \quad \forall z_1 \in (0, L_1), \tag{2.4a}$$

$$\frac{d^2 u_2(x_2)}{dx_2^2} = 0, \quad \frac{d^4 w_2(x_2)}{dx_2^4} = 0, \quad \forall x_2 \in (0, L), \tag{2.4b}$$

$$\frac{d^2 u_3(x_3)}{dx_3^2} = 0, \quad \frac{d^4 w_3(x_3)}{dx_3^4} = 0, \quad \forall x_3 \in (0, L). \tag{2.4c}$$

The natural and geometric boundary conditions at joint **a-b** are

$$\begin{aligned}
& w_1(0) = w_3(0), \quad u_1(0) = u_3(0) - \delta \frac{dw_3(0)}{dx_3}, \\
& -E_1 A_1 \frac{dw_1(0)}{dz_1} + (E_b I_{be} + 2a_2 I_{pe} + 2a_3 A_p) \frac{d^3 w_3(0)}{dx_3^3} = 0, \\
& E_1 I_1 \frac{d^3 u_1(0)}{dz_1^3} - \left[(E_b A_b + E_p A_p) \frac{du_3(0)}{dx_3} + a_8 A_p \right] = 0, \\
& K_t \left(\frac{dw_3(0)}{dx_3} + \frac{du_1(0)}{dz_1} \right) - \delta E_1 I_1 \frac{d^3 u_1(0)}{dz_1^3} - \\
& \left[(E_b I_{be} + 2a_2 I_{pe} + 2a_3 A_p) \frac{d^2 w_3(0)}{dx_3^2} + a_4 A_p \right] = 0, \\
& K_t \left(\frac{dw_3(0)}{dx_3} + \frac{du_1(0)}{dz_1} \right) - E_1 I_1 \frac{d^2 u_1(0)}{dz_1^2} = 0,
\end{aligned} \tag{2.5}$$

where δ is the length of rigid link **a-b**, I_1 is the moment of inertia of beam 1, I_{be} and I_{pe} are moment of inertia for Si_xN_y and PZT of beam 3, and A_b and A_p are the cross-sectional areas of Si_xN_y and PZT, respectively. The electro-mechanical factors a_2 , a_3 , a_4 and a_8 are given by

$$\begin{aligned}
a_2 &= \frac{1}{2} \left(E_p + \frac{e_{31}^2}{\epsilon_{33}} \right), \quad a_3 = \frac{-e_{31}^2 (2e + t_p)^2}{8\epsilon_{33}}, \\
a_4 &= -\frac{e_{31} (2e + t_p) V}{2t_p}, \quad a_8 = e_{31} \frac{V}{t_p}.
\end{aligned} \tag{2.6}$$

The boundary conditions at rigid joint **c** are

$$\begin{aligned}
 w_1(L_1) &= w_2(0), \quad u_1(L_1) = u_2(0), \\
 -\frac{du_1(L_1)}{dz_1} &= \frac{dw_2(0)}{dx_2}, \\
 E_1A_1\frac{dw_1(L_1)}{dz_1} + E_2I_2\frac{d^3w_2(0)}{dx_2^3} &= 0, \\
 -E_1I_1\frac{d^3u_1(L_1)}{dz_1^3} - E_2A_2\frac{du_2(0)}{dx_2} &= 0, \\
 -E_1I_1\frac{d^2u_1(L_1)}{dz_1^2} - E_2I_2\frac{d^2w_2(0)}{dx_2^2} &= 0.
 \end{aligned} \tag{2.7}$$

The reflective symmetric boundary conditions at **d** are

$$u_2(L) = 0, \quad \frac{dw_2(L)}{dx_2} = 0, \quad -E_2I_2\frac{d^3w_2(L)}{dx_2^3} = F, \tag{2.8}$$

where F is the vertical point force applied at **d**. The fixed boundary conditions at **f** are given by

$$u_3(L) = 0, \quad w_3(L) = 0, \quad \frac{dw_3(L)}{dx_3} = 0. \tag{2.9}$$

In total, there are 6 differential equations (2.4) and 18 boundary conditions (2.5)-

(2.9). The solutions of Eqs. (2.5) are

$$\begin{aligned}
 w_i(x) &= a_{3i}x^3 + a_{2i}x^2 + a_{1i}x + a_{0i}, \quad i = 2, 3, \\
 u_1(z) &= b_{31}z^3 + b_{21}z^2 + b_{11}z + b_{01}, \\
 u_i(x) &= b_{1i}x + b_{0i}, \quad i = 2, 3, \\
 w_1(z) &= a_{11}z + a_{01}.
 \end{aligned} \tag{2.10}$$

The 18 unknown coefficients a_{ij} , b_{ij} are solved analytically using the 18 boundary conditions using MAPLE.

2.6 Results and Discussion

To validate the model, we compare the theoretically predicted displacement and blocking force with the experimental results. The parameters are shown in Table 2.1. The displacement of the uniflex actuator at \mathbf{d} is obtained with $F = 0$ and $V = 10$ V. The blocking force is obtained by enforcing a clamped boundary condition at \mathbf{d} , applying $V = 10$ V, and calculating the vertical resultant force at \mathbf{d} . The model can also produce the displacement of the unimorph without the cap by setting $t_a = 0$.

2.6.1 Rigid Joint Model ($K_t = \infty$)

To better understand the physics of the uniflex actuator, we investigate the displacement as a function of a critical parameter in the structural design: The clearance or gap be-

Table 2.1. Parameters for uniflex actuator

Description	
Young's modulus of Si_xN_y , E_b (GPa) [72]	250
Young's modulus of PZT, E_p (GPa) [73]	100
Young's modulus of Al, E_a (GPa) [74]	70
Thickness of Si_xN_y , t_b (μm)	1
Thickness of PZT, t_p (μm)	1, 1.4
Thickness of Al, t_a (μm)	1, 2
Width of actuator, b (μm)	70
Piezo-electric coefficient, d_{31} (C/N) [75]	-40e-12
Permittivity of PZT, ϵ_{33} ($\text{C}^2/(\text{Nm}^2)$) [76]	7.97e-09
Applied potential difference, V (V)	10

tween the unimorph and cap, L_1 . In this analysis, Fig. 2.10 shows the theoretical uniflex actuator displacement with $K_t = \infty$ at the center ($w_2(L)$) and at the end ($w_3(0)$) of the uniflex actuator for a 300 μm long actuator. For the rigid joint case, sanity checks are made by comparing the predicted uniflex actuator deflections, using our analytical solution, with ANSYS simulations and they are found to agree well with each other. For small clearances, the displacement at the end is actually larger than the displacement at the center. This means that the flexural effect is being overwhelmed by the clamped boundary condition at $x_2 = 0$. The clamped boundary condition forces the Al cap downward because the downward slope of the Al cap approximately matches the upward slope of the unimorph if the clearance is small.

In fact, for zero clearance, the cap bends down with the same shape that the unimorph bends up, resulting in zero displacement at center of aluminum cap. As clearance increases $w_2(L)$ gradually increases due to relaxation obtained from beam 1 deformation.

At a critical gap ($L_1 = 1.6 \mu\text{m}$ for this set of parameters) the model predicts that the aluminum cap takes a horizontally flat shape after deformation because the boundary rotation causes the same amount of downward deflection as the flexural effect causes upward deflection. Clearly, this is the minimum clearance that is required to ensure that the uniflex actuator produces a maximum displacement $w_2(L)$ at the center of aluminum cap instead of at the tip of unimorph, thereby, taking advantage of both the unimorph and flexural displacement amplifying mechanisms.

If we make the aluminum cap thickness $t_a = 0$, the model can predict the unimorph alone tip displacement $w_3(0)$ without the aluminum cap. Further, if $E_b = E_p$, $t_b = t_p = t/2$, the unimorph tip displacement reduces to

$$w_3(0) = \frac{12\epsilon_{33}L^2d_{31}V}{t^2(8\epsilon_{33} + E_p d_{31}^2)}, \quad (2.11)$$

where, t =total unimorph thickness. As $E_p d_{31}^2$ is 3 orders smaller than ϵ_{33} , the displacement can be further simplified by neglecting it as

$$w_3(0) = \frac{3L^2d_{31}V}{2t^2}, \quad (2.12)$$

which is same as developed by earlier researchers [27] for unimorph actuators. So the model can be used to predict unimorph alone actuator displacement by making aluminum cap thickness as zero.

For the uniflex actuator however, the theoretically predicted displacements under the

assumption of $K_t = \infty$ are significantly lower than the experimentally measured values. Similar under prediction for the blocking force has also been observed with this model. We hypothesize that this disagreement between theory and experiment arises due to mismatch between the ideal boundary conditions used in the model and the actual boundary conditions that exist in the fabricated actuators that lead to larger displacements. Weakening of the joint b is one possible imperfection that could be caused by poor adhesion between the Al cap and the substrate. For the observed deflections, the expected change in the angle of this joint is ~ 0.8 to 1.8 degree for lengths of actuators from $200 \mu\text{m}$ to $500 \mu\text{m}$, therefore any imperfections between the interface of the PZT/Al cap layer can easily have the effect of softening this spring. The stress is relatively high at joint b and repeated actuation could also weaken the joint. This weakening would result in less clockwise rotation of beam 1 in the model and a corresponding increase in displacement. The limiting case of such a joint approximates a hinge in which case $K_t = 0$

2.6.2 Weakened Joint Model ($K_t < \infty$)

Stiffness $K_t < \infty$ is introduced into the mathematical model to simulate the uniflex actuators with a weakened joint. Figure 2.11 shows the experimentally measured deflection and the model fitting to the data for the four actuator configurations. In each case the stiffness of the torsional spring K_t was adjusted to match the experimentally observed data. Figure 2.11 shows that one value of K_t can be used to match the averaged displacement of several actuators with four different lengths. It must be noted that although

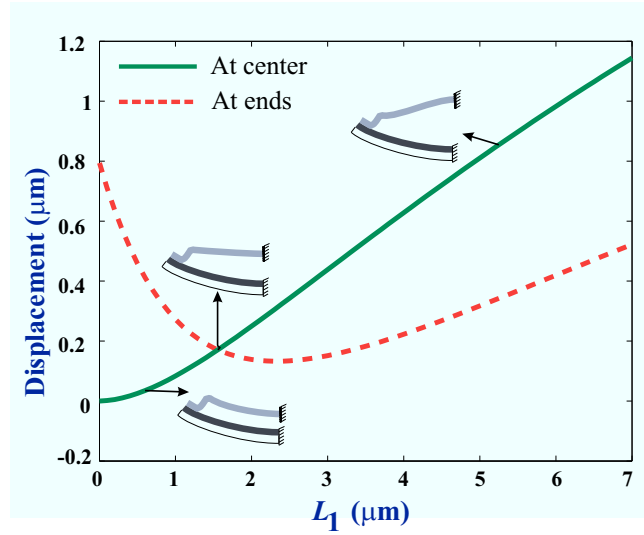


Figure 2.10. Geometrically exact uniflex actuator model displacement versus clearance L_1 for an actuator length $L_a=300 \mu\text{m}$, rigid joint ($K_t = \infty$), Aluminum cap thickness $t_a = 1 \mu\text{m}$, PZT thickness $t_p = 1 \mu\text{m}$, and other actuator parameters shown in Tab. 2.1: $w_2(L)$ (solid line) and $w_3(0)$ (dashed).

we use $K_t = \infty$ in the rigid joint approximation, for the devices discussed in this work $K_t = 1 \mu\text{Nm/rad}$ already has the effect of an infinitely rigid joint. In comparison to this value the weakened joint model is found use a value of K_t between 0 - 33 nNm/rad. Furthermore, it is interesting to note that a single value of K_t seems to fit the observed deflection for all four lengths of the devices tested. However different K_t values are required for the different stack thickness configurations of the actuators. Since actuators of different lengths but same stack configuration are made under identical fabrication steps it seems reasonable to attribute the origin of weakening of the joint to the fabrication, material, and interface properties between the Al cap and the PZT layers. Since no interface evaluation studies were performed, it is not possible to attribute this effect with any further specificity in terms of process step and/or materials. In addition to the

inclusion of K_f , the structure of the fabricated device has two other imperfections that need to be mentioned here. The first relates to the built-in stress gradients in the actuator structure which results in a pre-deflected initial state. Typically this initial deflection was less than $5 \mu\text{m}$ for the $500 \mu\text{m}$ long actuators. This worst case initial deflection is relatively small giving a radius of curvature of $\sim 6.25 \text{ mm}$ and was therefore not considered as part of the initial modeling. Another imperfection which was not considered arises from the undesired double clamped bridge actuator structure to which the actuator is attached. Since the application of voltage is also expected to actuate this bridge structure, the overall deflection can be expected to be affected by this effect. To reduce this effect, in the design of the actuator, we have minimized the width of electrode that runs on this double clamped structure. Furthermore, any undesired actuation of the PZT double-clamped bridge is likely to induce overall tensile stress in the structure and will essentially pull the bridge structure taut approximating more of the ideal boundary condition. Since all deflections measured were relative to the bridge, we did not consider non-idealities arising from this effect in our model.

The blocking force measurements performed using the nanoindenter were much more complex experiments and the performance of the actuators under these boundary conditions is less well understood. As can be seen in Table 2.2 the experimental blocking force data is far more scattered and shows little patterns of correlation between the geometric dimensions of the actuators and the measured blocking force. In Table 2.2, the blocking force predicted using the developed model is also listed. In each case we

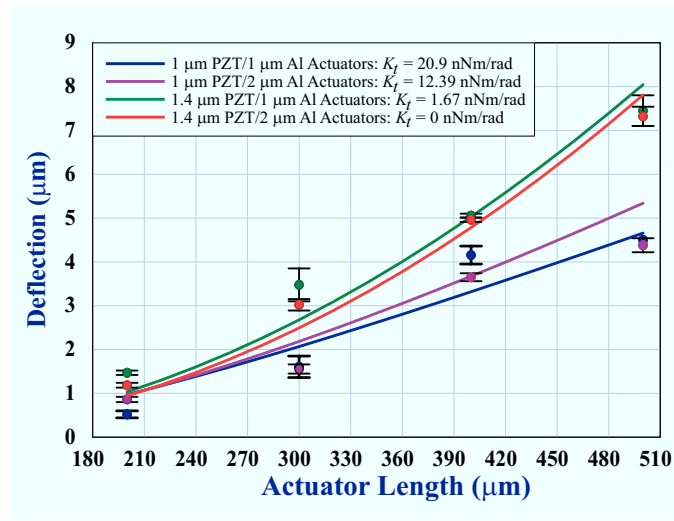


Figure 2.11. Displacement versus actuator length L_a for the four configurations of the actuator: Uniflex experimental data is shown as dots, and theoretical weakened joint displacement $w_2(L)$ is shown as the solid lines. The individually tuned torsional spring constants that were required to closely match the experimentally observed data are indicated in the figure legend.

used the same torsional spring constant as used for predicting the deflection of the actuators. For the 2 μm thick Al cap devices, the agreement between the model and the measured values is close. For other cases the agreement is not so close, but $\sim 50\%$ of the experimentally observed blocking force. The data from Table 2.2 clearly provides only further evidence of joint weakening in the fabricated uniflex actuators. The scatter in the blocking force data could easily be arising out of the initial loading force of 1.5 μN that is used for determining the zero position of the aluminum flexure of the actuator by the nanoindenter. This is a significant proportion of the predicted blocking force of the actuators. This force might cause the double clamped bridge structure which supports the actuator to bend downwards resulting in a perturbed zero position of the actuator. Upon actuation, the tensile stress that will be generated in the bridge structure is likely

Table 2.2. Uniflex actuator blocking force experimental data and theoretical predictions

Actuator Thickness (PZT/Al Cap)	Actuator Length (μm)	Measured Blocking Force (μN)	Predicted Blocking Force (μN)
1 μm /1 μm	300	16	5.5835
	400	12	3.3718
1 μm /2 μm	300	18.52	20.773
	500	6.2	10.571
1.4 μm /1 μm	300	20.26	8.6304
	500	9.9	4.7568
1.4 μm /2 μm	300	20.4	23.519
	400	17.2	17.005

Table 2.3. Uniflex* actuator displacement amplification over unimorph actuator for PZT thickness $t_p = 1.4 \mu\text{m}$, Si_3N_4 thickness $t_b = 1 \mu\text{m}$, and Aluminum thickness* $t_a = 1 \mu\text{m}$ at 10 V

Actuator Length (L_a) (μm)	Unimorph Displacement ($w_3(0)$) (μm)	Uniflex Displacement ($w_2(L)$) (μm)	Amplification ($\frac{w_2(L)}{w_3(0)}$)
300	2.38	3.48	1.46
400	3.61	5.06	1.40
500	5.17	7.45	1.44

to cause it to flatten, essentially resulting in additional blocking force to be added to the measurement. This can easily result in the observed scatter in the experimental results. On the other hand, deflection measurements performed under zero loading force do not suffer from this situation and show less scatter.

Overall the uniflex actuators presented show a performance that is superior to reports in the literature on similar unimorph actuators. While a direct comparison without accounting for the detailed geometric, structural, and material factors makes it difficult, cantilever type unimorph actuators have been reported to obtain blocking forces in the range of 2 - 55 μN with a maximum deflection of 6 - 1 μm at drive voltages of 2 - 10 V

respectively [77, 78]. The values of deflection and blocking force reported in this work for the 1.4 μm thick PZT and 1 and 2 μm thick Al cap, clearly exhibit higher values than these reported values. In this work, as shown in table 2.3, we were able to obtain $\sim 40\%$ greater deflection in the uniflex actuators (1 μm thick Aluminum cap) as compared to the similar unimorph actuators proving the efficacy of the uniflex design.

Optimization of Piezoelectric Uniflex Actuator

3.1 Introduction

In this chapter, we optimize and compare the performance of a uniflex actuator with unimorph and flextensional actuators in terms of displacement and blocking force. The uniflex model developed and validated in Chapter 2 is used to predict displacement and blocking force.

3.2 Unimorph, Flextensional, and Uniflex Actuators

Fig. 3.1(a) shows the schematic of a deflected unimorph actuator. The passive bottom layer is assumed to be Si_xN_y , and the top layer $\text{PbZr}_{0.52}\text{Ti}_{0.48}\text{O}_3$ (PZT). Electrodes are

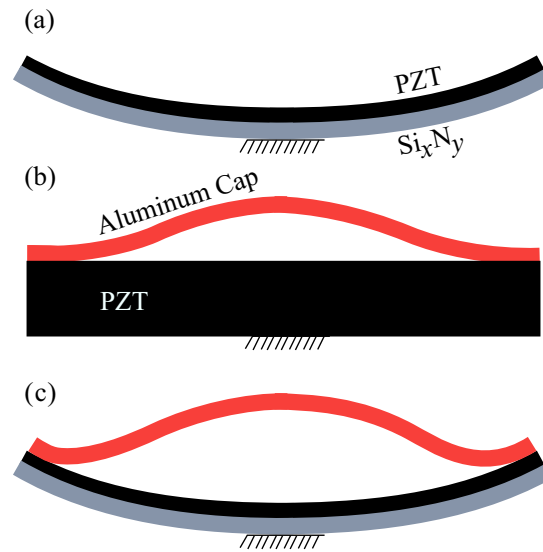


Figure 3.1. Schematic of deflected (a) unimorph, (b) flextensional, and (c) uniflex actuators.

placed on the top and bottom of the PZT layer. The PZT is poled through the thickness and voltage applied across the thickness causes the PZT layer to contract due to the d_{31} coefficient, resulting in upward bending of the actuator. The flextensional actuator shown in Fig. 3.1(b) uses the flexural motion of an aluminum (Al) cap to produce displacement. Voltage applied across the thickness of the bulk PZT contracts the PZT and flexes the Al cap upward.

The uniflex actuator shown in Fig. 3.1(c) consists of a unimorph that is supported at the center and an Al cap that is bonded at the ends of the unimorph. The Al cap is bonded to the ends of unimorph structure such that there is a small offset from PZT. As in the unimorph, the PZT is poled through the thickness and electroded on both top and bottom. Voltage across the thickness causes PZT contraction and bending of the unimorph. The Al cap is compressed by the unimorph and, if correctly designed, buckles

upward. Thus, the uniflex actuator combines the unimorph and flexural displacement amplification mechanisms to produce large vertical displacement at the center of the Al cap.

3.3 Mathematical Models

Mathematical models for displacement and blocking force of a uniflex actuator are developed and validated [79, 68]. The free displacement of a uniflex actuator at the center of aluminum cap is

$$w_{UF} = \frac{C_1 L^3 + C_2 L^2}{C_3 L^2 + C_4 L + C_5}, \quad (3.1)$$

where L is the half length of the actuator and the coefficients C_1, \dots, C_5 are defined in Appendix A and depend on the system parameters: E_a , E_b , and E_p are the Young's moduli, t_a , t_b , and t_p are the thicknesses, A_a , A_b , and A_p are the cross-sectional areas, I_a , I_{be} , and I_{pe} are moments of inertia about the neutral axis of aluminum cap, silicon nitride, and PZT respectively, and L_1 is the initial gap between Al cap and PZT. The parameters a_2 , a_3 , a_4 , and a_8 are the electromechanical factors, δ is the offset, and K_l is the joint stiffness.

The blocking force of a uniflex actuator, defined as the force required to constrain the center of aluminum cap at zero vertical displacement upon actuation is

$$F_{UF} = 2w_{UF} \left(\frac{-B_7 L^2 - B_8 L - B_9}{B_1 L^5 + B_2 L^4 + B_3 L^3 + B_4 L^2 + B_5 L + B_6} \right), \quad (3.2)$$

where the coefficients B_1, \dots, B_9 are defined in Appendix A.

The displacement w_F and blocking force F_F of flextensional actuator at the center of the aluminum cap are obtained directly from equations 3.1 and 3.2 by equating the thickness of silicon nitride layer t_b to zero.

For the unimorph (shown in Fig. 3.1(a)), the displacement w_U and blocking force F_U are evaluated at the tip. The tip displacement w_U , obtained by letting aluminum cap thickness $t_a = 0$ in the uniflex model [79], is

$$w_U = \frac{L^2 a_4 A_p}{2(E_b I_{be} + 2a_2 I_{pe} + 2a_3 A_p)}, \quad (3.3)$$

and the blocking force is

$$F_U = \frac{3a_4 A_p}{L}. \quad (3.4)$$

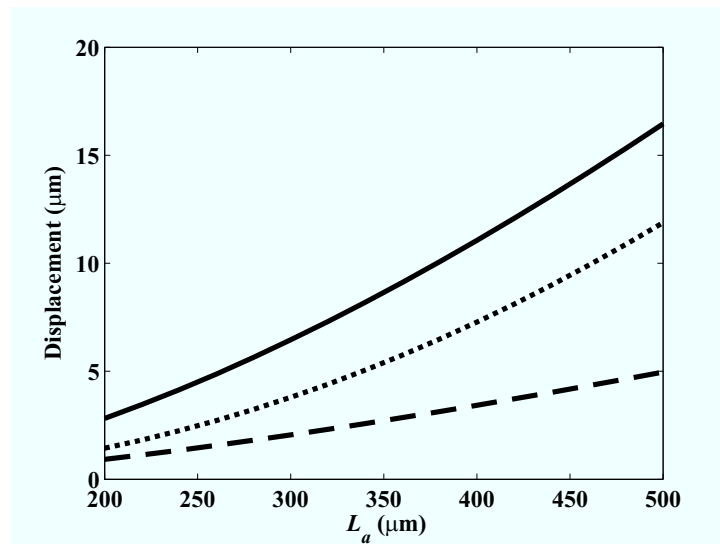


Figure 3.2. Maximum displacement versus actuator length: uniflex actuator w_{UF} with $t_a = 1 \mu\text{m}$ (solid), unimorph actuator w_U (dotted), and flextensional actuator w_F with $t_a = 1 \mu\text{m}$ (dashed).

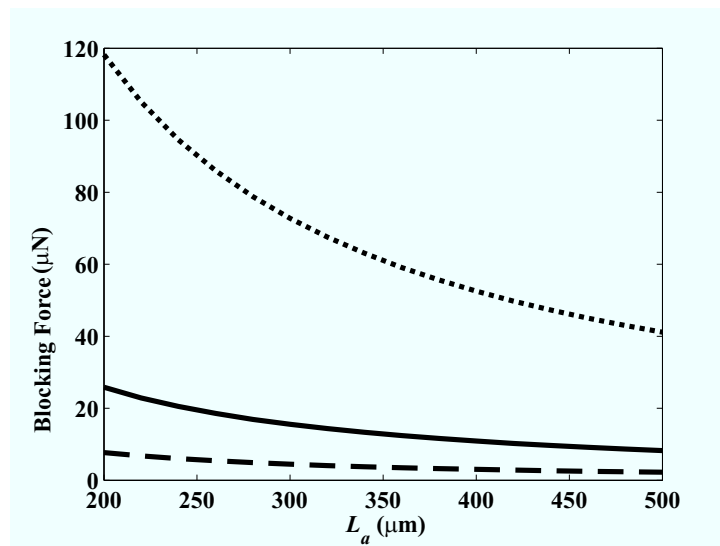


Figure 3.3. Blocking force for maximum displacement design versus actuator length: uniflex actuator F_{UF} with $t_a = 1 \mu\text{m}$ (solid), unimorph actuator F_U (dotted), and flextensional actuator F_F with $t_a = 1 \mu\text{m}$ (dashed).

3.4 Optimal Design

The uniflex model predicts the displacement and blocking force of uniflex actuators, so it can be used to optimize the uniflex design. The uniflex design has many geometric parameters that can be optimized: L_a , b , L_1 , t_a , t_p , and t_b . The actuator length includes the active and a $40 \mu\text{m}$ bonding region so $L_a = 2L + 40 \mu\text{m}$. The displacement and blocking force increase and decrease with actuator length L_a , respectively, so it is considered to be an input to the design. The actuator width, b , does not affect displacement and proportionally scales blocking force, so it is held constant at $70 \mu\text{m}$. The material properties given in Tab. 2.1 with $d_{31} = -30 \text{ pC/N}$, $K_t = 4e-9$ are used. A constant electric field of $20 \text{ V}/\mu\text{m}$ is applied for all the actuators during comparison. The overall thickness of the unimorph is held constant at $t_p + t_b = 2 \mu\text{m}$.

The optimal uniflex results are compared with an optimal $2 \mu\text{m}$ thick unimorph of length $2L$ and an optimal flextensional actuator of length L_a . Optimization is performed by the pattern search algorithm in MATLAB.

The unimorph has an optimal ratio $t_p/t_b = 1.58$ that produces both maximum displacement and blocking force. The flextensional actuator is the same as uniflex actuator except that $t_p = 0$. The clearance L_1 and thickness t_a are optimized as in the uniflex actuator to produce maximum displacement or maximum blocking force.

In the following, we optimize L_1 , t_p/t_b and t_a to either produce maximum displacement or blocking force for uniflex actuators. The optimal uniflex designs are compared with the optimal unimorph and flextensional actuators.

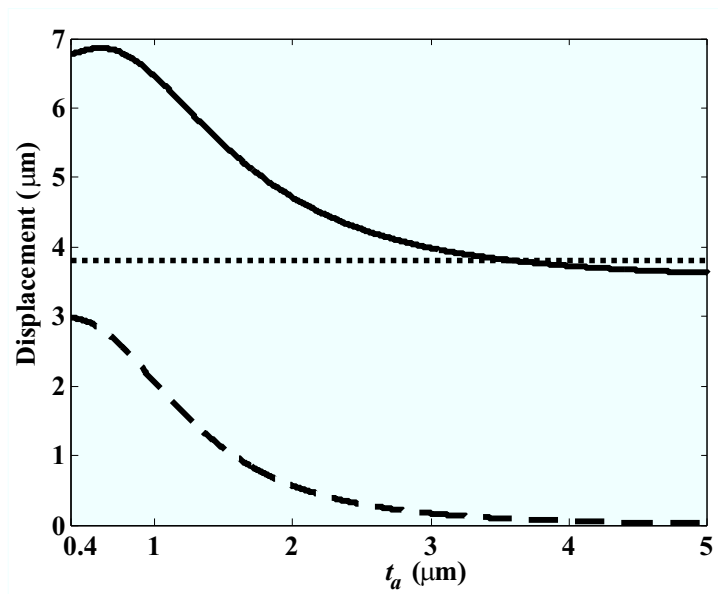


Figure 3.4. Maximum displacement versus Al thickness ($L_a = 300 \mu\text{m}$): uniflex w_{UF} (solid), unimorph w_U (dotted), and flextensional w_F (dashed).

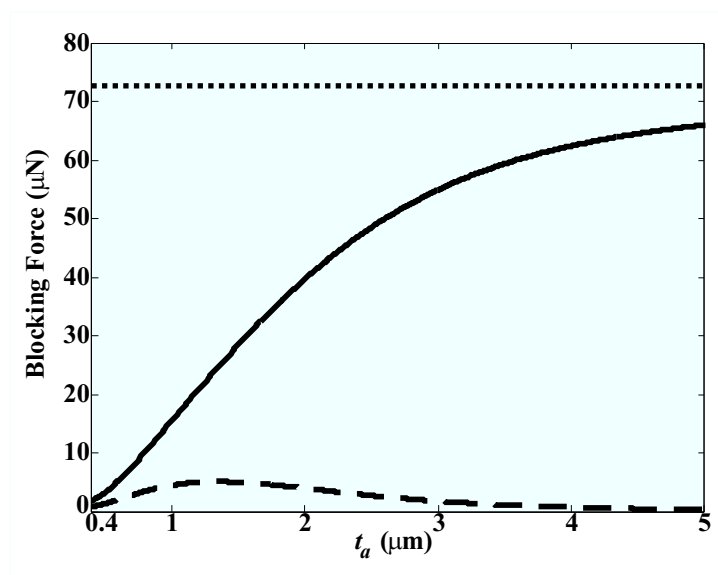


Figure 3.5. Blocking force for maximum displacement design versus Al thickness ($L_a = 300 \mu\text{m}$): uniflex F_{UF} (solid), unimorph F_U (dotted), and flextensional F_F (dashed).

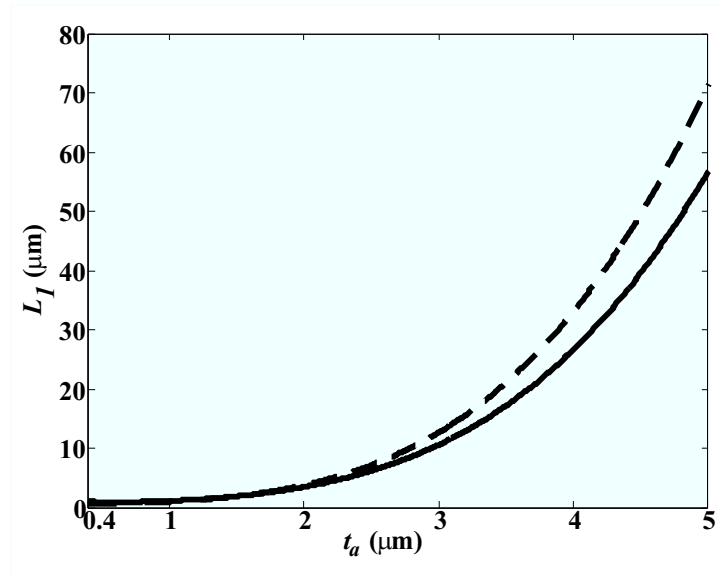


Figure 3.6. Clearance for maximum displacement design versus Al thickness ($L_a = 300 \mu\text{m}$): uniflex (solid) and flextensional (dashed).

3.4.1 Maximized Displacement Design

Optimization of the flextensional and uniflex designs for maximum displacement with all the parameters L_1 , t_p/t_b and t_a as variables for a given actuator length L_a produces a thin aluminum cap, with t_a approaching zero. We therefore first fix t_a , and find the ratio t_p/t_b and clearance L_1 that maximize actuator displacement. For optimization using the pattern search algorithm, the objective function is to maximize displacement with constraints $t_a = 1 \mu\text{m}$, $t_p/t_b = 0$ to 1 , $L_1 = 0$ to ∞ and actuator length L_a prescribed from 200 to $500 \mu\text{m}$ in increments of $10 \mu\text{m}$.

Figures 3.2 and 3.3 show the displacement and corresponding blocking force for

actuators that are designed to maximize displacement. The displacement of all three actuators increases with the actuator length. The uniflex actuator maximum displacement in Fig. 3.2 is higher than that of the optimal unimorph and flextensional actuators. The optimal clearance $L_a/L_1 \approx 300$ and the optimal $t_p/t_b \approx 2$ for the displacement optimized uniflex actuator with $t_a = 1 \mu\text{m}$ and $200 \mu\text{m} < L_a < 500 \mu\text{m}$. The blocking force in Fig. 3.3, however, is lower than the unimorph but higher than the flextensional actuator.

In order to study the effect of aluminum cap thickness t_a on maximum displacement, we fix the actuator length $L_a = 300 \mu\text{m}$ and find optimum clearance L_1 and ratio t_p/t_b that produces maximum displacement for a given $t_a = 0.4$ to $5 \mu\text{m}$. Figures 3.4 and 3.5 show the displacement and blocking force variations with t_a for the displacement optimized actuators. The unimorph actuator has no Al cap, so the displacement and blocking force are independent of t_a at the values for $L_a = 300 \mu\text{m}$ of $w_U(0) = 3.8 \mu\text{m}$ and $F_U = 73 \mu\text{N}$. The flextensional effect is amplified at low t_a for both the uniflex and flextensional designs showing that the optimal aluminum cap thickness t_a is the thinnest physically possible layer. The unimorph blocking force, however, is greater than the uniflex and flextensional designs, which vanishingly small as $t_a \rightarrow 0$. As t_a gets large, the uniflex displacement and blocking force converge to the unimorph values from above and below, respectively. The optimal clearance (see Fig. 3.6) is more sensitive to t_a , increasing from $L_a/L_1 = 300$ to 5.4 as $t_a = 1 \mu\text{m}$ to $5 \mu\text{m}$. The optimal ratio t_p/t_b is found to decrease from 2.1 to 1.6 over this range of t_a .

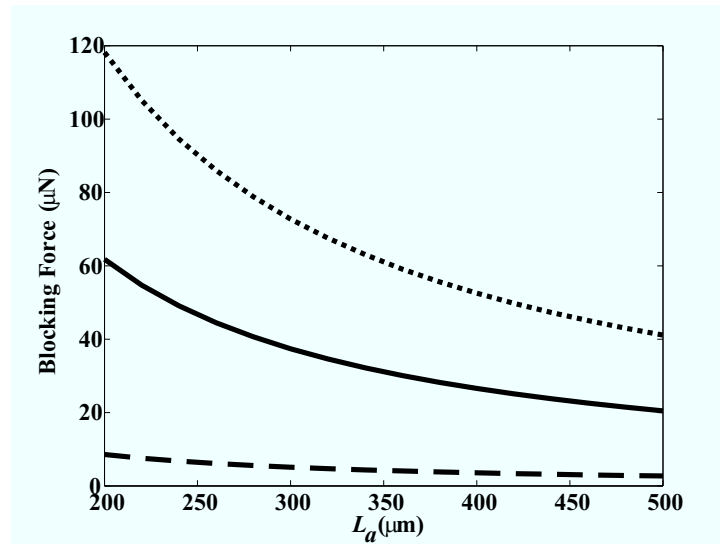


Figure 3.7. Maximum blocking force versus actuator length: uniflex actuator F_{UF} with clearance $L_1 = 2.7 \mu\text{m}$ (solid), unimorph actuator F_U (dotted), and flextensional actuator F_F with clearance $L_1 = 2.7 \mu\text{m}$ (dashed).

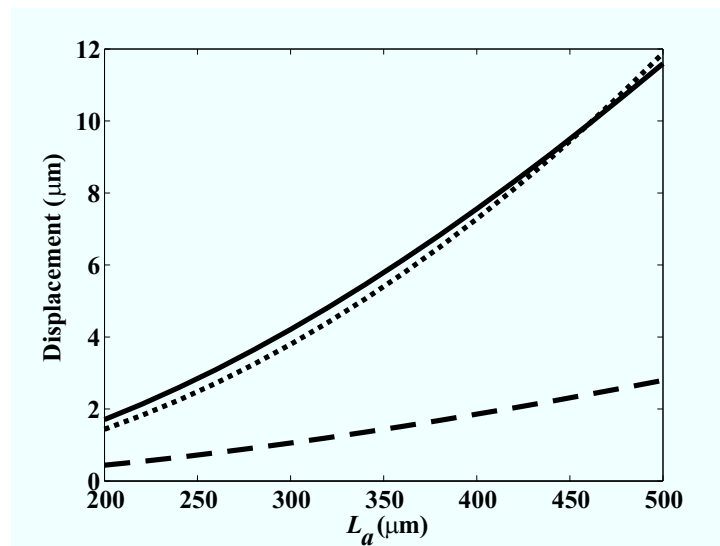


Figure 3.8. Displacement for maximum blocking force design versus actuator length: uniflex actuator w_{UF} with clearance $L_1 = 2.7 \mu\text{m}$ (solid), unimorph actuator w_U (dotted), and flextensional actuator w_F with clearance $L_1 = 2.7 \mu\text{m}$ (dashed).

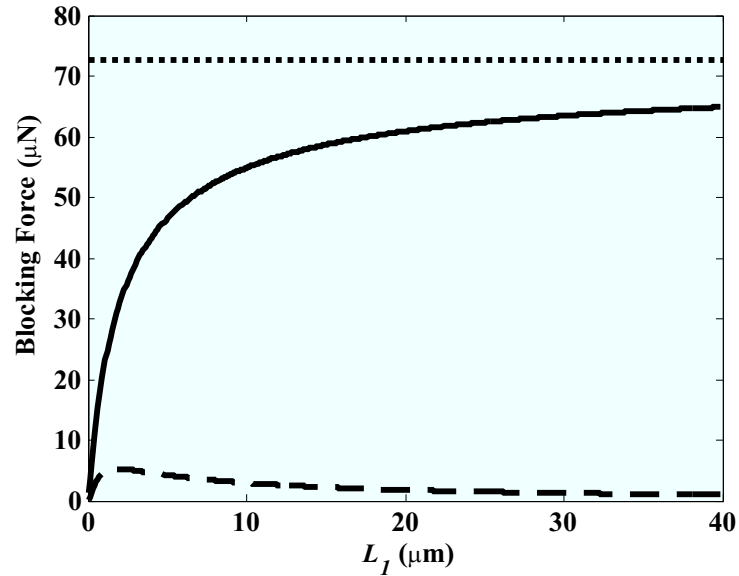


Figure 3.9. Maximum blocking force versus clearance ($L_a = 300 \mu\text{m}$): uniflex actuator F_{UF} (solid), unimorph F_U (dotted), and flextensional actuator F_F (dashed).

3.4.2 Maximized Blocking Force Design

Similar to the maximum displacement design, optimization of the uniflex actuator for maximum blocking force with all the parameters as variables for a given actuator length L_a increases the clearance L_1 to excessively large values. We therefore first fix $L_1 = 2.7 \mu\text{m}$ and find the t_p/t_b ratio and aluminum cap thickness t_a for a given actuator length L_a that maximize the blocking force. Figures 3.7 and 3.8 show the optimization results for the maximized blocking force designs versus L_a . The blocking force (Fig. 3.7) decreases with increasing actuator length for all three actuators. The uniflex blocking force is larger than the displacement optimized designs in Fig. 3.3. The displacement in Fig. 3.8 increases with actuator length. The uniflex displacement is smaller than the displacement-optimized designs in Fig. 3.2.

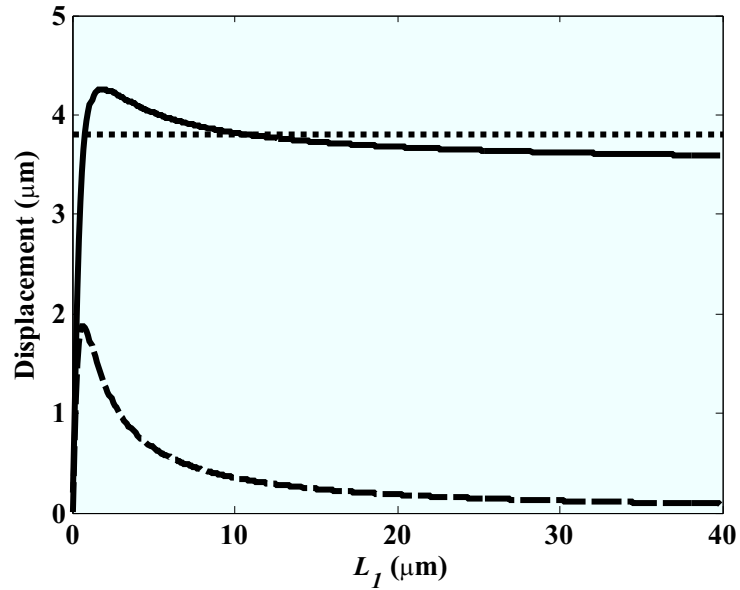


Figure 3.10. Displacement for maximum blocking force design versus clearance ($L_a = 300 \mu\text{m}$): uniflex actuator w_{UF} (solid), unimorph w_U (dotted) and flextensional actuator w_F (dashed).

The unimorph actuator produces the highest blocking force followed by the uniflex and flextensional actuators. The uniflex and unimorph actuators produce similar displacement with the flextensional design producing significantly less displacement. From the optimization it is found that with the increasing actuator length (L_a), the optimum aluminum cap thickness (t_a) and ratio (t_p/t_b) remain approximately constant ($t_a \approx 2.2 \mu\text{m}$ and $t_p/t_b \approx 1.65$) for the uniflex actuator with $L_1 = 2.7 \mu\text{m}$.

Now the effect of clearance L_1 is studied for a fixed actuator length $L_a = 300 \mu\text{m}$ by varying the ratio t_p/t_b and aluminum cap thickness t_a for a given clearance $L_1 = 0$ to $40 \mu\text{m}$ producing maximum blocking force. Figures 3.9 and 3.10 show the maximized blocking force design versus clearance. In Fig. 3.8, the uniflex maximum blocking force increases monotonically and approaches the unimorph. The flextensional blocking

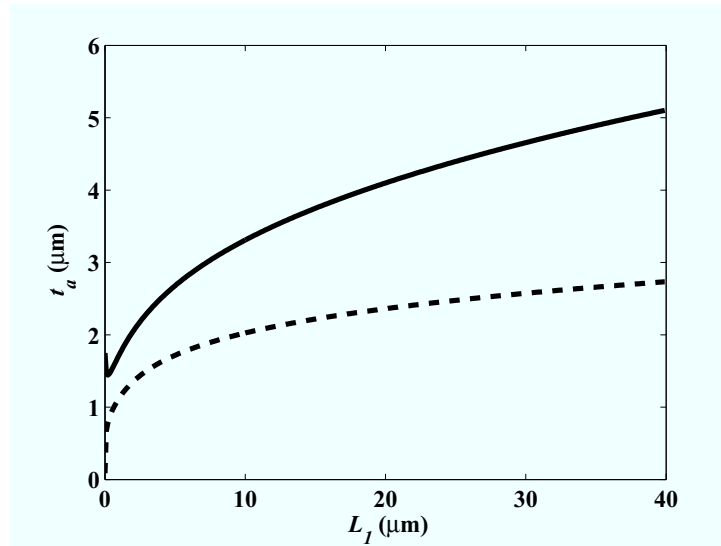


Figure 3.11. Aluminum cap thickness t_a for maximum blocking force design versus clearance ($L_a = 300 \mu\text{m}$): uniflex actuator (solid) and flextensional actuator (dashed).

force, on the other hand, increases initially and then decreases for $L_1 > 3 \mu\text{m}$. The corresponding displacements (Fig. 3.10) remain almost constant and approach zero for the uniflex and flextensional actuators, respectively, as L_1 increases. The uniflex and flextensional designs have a thicker aluminum cap as (L_1) increases as shown in Fig. 3.11. The uniflex actuator optimum $t_p/t_b \approx 1.65$ for these cases.

The optimization results show that a properly designed uniflex actuator produces more displacement than the unimorph and flextensional actuators. With a thick cap and large gap the uniflex actuator approaches but does not exceed the unimorph blocking force.

Piezoelectric T-beam Actuators

4.1 Introduction

This chapter introduces a novel monolithic T-beam actuator design that can be fabricated from bulk PZT by dicing or micro-machining and does not require bonding of two layers. This chapter describes the design, fabrication, and testing of meso-scale prototypes that are diced from bulk PZT. Although micro-scale T-beam actuators are not described here, they can be fabricated using Reactive Ion Etching [69] and the models developed in this thesis can be applied to their design and optimization. The meso-scale T-beam actuators fabricated are experimentally shown to produce both out-of-plane and in-plane displacements and out-of-plane blocking force. Models are developed that predict in-plane and out-of-plane displacement and out-of-plane blocking force as functions of the T-beam parameters and the applied voltage. Experimental measurements of displacements and blocking forces validate the theoretical models. Model-based analysis and

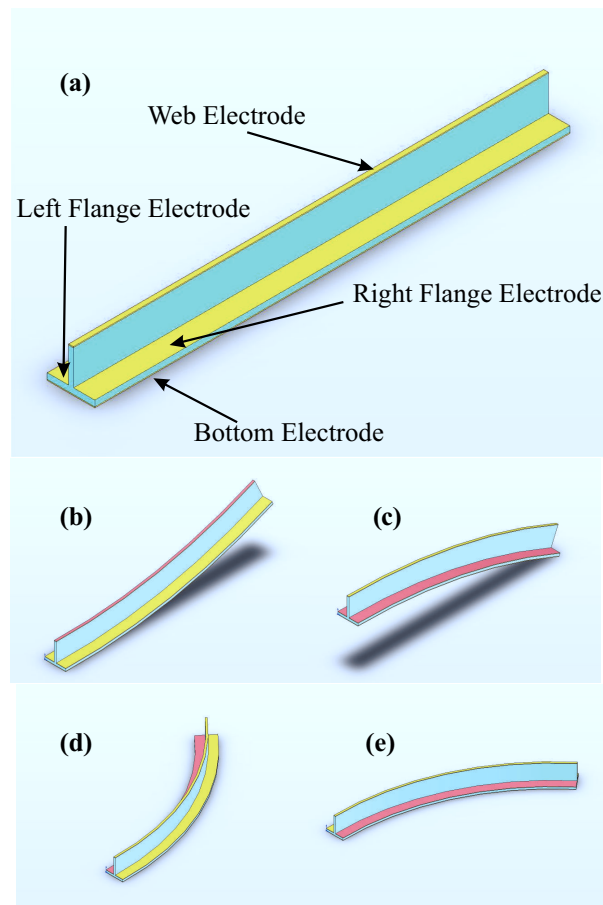


Figure 4.1. T-beam actuator concept: (a) As fabricated and deflected shapes when voltage is applied between (b) both flanges and bottom electrodes, (c) web and bottom electrode, (d) left flange and bottom electrode, and (e) right flange and bottom electrode.

optimization are used to optimize the T-beam actuator geometry to produce large displacement and blocking force. T-Beam out-of-plane displacement and blocking force performance is compared with a unimorph.

4.2 The T-Beam Actuator Concept

The schematic design of a cantilevered T-beam actuator that has a T-shaped cross-section is shown in Fig. 4.1. The entire T-beam is PZT with electrodes deposited on the top of the web, the top of each flange, and the bottom of the flange. The PZT is poled through-the-thickness from top to bottom.

Fig. 4.1 shows that the T-beam actuator can be bent both in-plane and out-of-plane by selectively activating the various electrodes. The bottom electrode acts as a ground. Out-of-plane motion can be achieved by applying voltage to the web electrode or to both flange electrodes. Application of voltage to the web electrode causes the web to expand through the thickness and contracts (d_{31} piezoelectric effect). The inactive flange constrains the lower part of the T-beam, acting as the passive layer in a unimorph design, and the beam bends upward (see Fig. 4.1(b)). Alternatively, the two flanges contract due to flange actuation, the web resists contraction, and the T-beam bends downward (see Fig. 4.1(c)).

The T-beam can also provide in-plane displacement by differential application of voltage to the two flanges. For in-plane bending the left and right flange electrodes are actuated to produce left and right bending as shown in Figs. 4.1(d) and 4.1(e), respectively.

Preliminary investigations of T-beams are performed using the finite element models. ANSYS SOLID5 three dimensional piezoelectric coupled field elements are used to model the entire T-beam. Cantilevered boundary conditions are applied with dis-

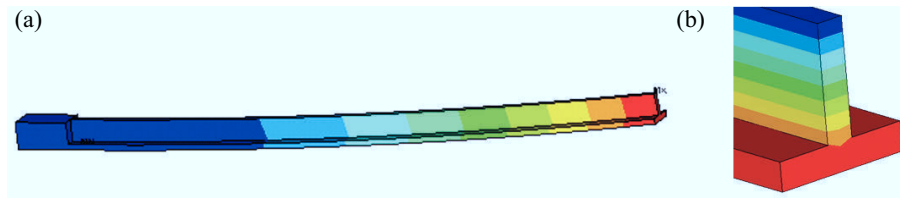


Figure 4.2. Web actuated cantilevered T-beam: (a) Transverse deflection, and (b) electric field placements rigidly fixed at left end and left free at right end. Figure 4.2(a) shows the transverse deflection of the T-beam for web actuation when voltage is applied between top of the web and entire bottom electrode region. Figure 4.2(b) shows that the electric field is concentrated in the web region under web actuation. Similarly, electric field is concentrated in the flange region under flange actuation and in the single flange under single flange actuation.

4.3 Analytical Modeling

To understand the physical behavior of the T-beam actuator and optimize its performance we develop a physics based model that predicts its out-of-plane and in-plane displacement and blocking force. The T-beam actuator with the web and flange electrodes shown in Fig. 4.3 is modeled as a cantilever beam using Euler-Bernoulli beam theory and assuming uniform electric field through the thickness. Fig. 4.3(a) shows a schematic of the initial and deflected shapes of the T-beam actuator in both out-of-plane (top) and in-plane (bottom) directions. The beam is assumed to be initially straight and lying along the longitudinal x_1 axis. F_2 and F_3 are the horizontal (inplane) and vertical

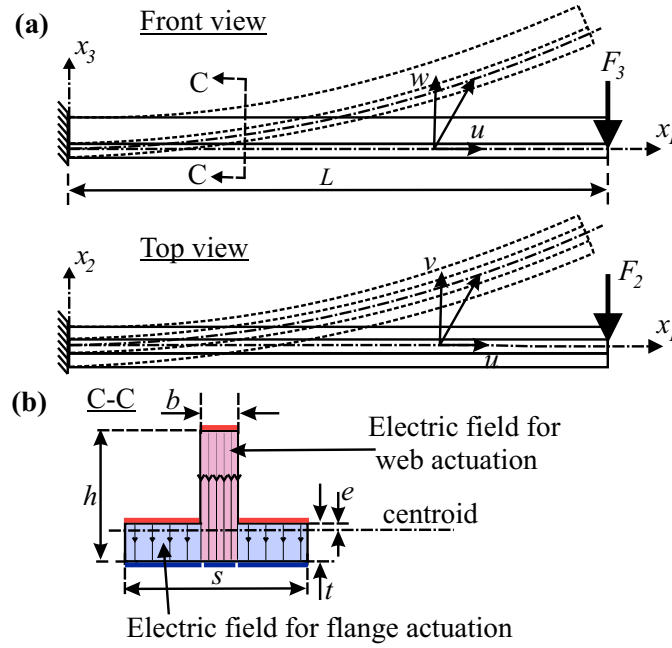


Figure 4.3. T-beam model: (a) the initial and deflected shape (out-of-plane (top) and in-plane (bottom)) and (b) cross section.

loads passing through the shear center of beam such that they do not cause twist. The variables u , v and w denote the displacements in the longitudinal (x_1), transverse in-plane (x_2) and transverse out-of-plane (x_3) directions, respectively. The cross-section of the T-beam shown in Fig. 4.3(b) has a flange width s , flange thickness t , web thickness b , and overall height h . The longitudinal axis runs through the centroid of the T-beam cross section, halfway through the cross section in the x_3 direction and through the centroidal at a distance

$$e = \frac{1}{2} \frac{t^2 s - t^2 b + 2tbh - bh^2}{ts - tb + bh}, \quad (4.1)$$

below the top of the flange. As shown in Fig. 4.3 (b), the bottom electroded is subdivided into three regions under the right and left flanges and the web. For upward out-of-

plane actuation, voltage, V is applied between the web and the middle electrode on the bottom of the flange. Voltage applied between right or left flange electrodes and the corresponding outer electrode on the bottom of the flange produces in-plane motion. We assume uniform and constant electric field along the x_3 axis through the thickness of actuator as shown in Fig. 4.3(b). For flange actuation, $V = \phi_{\text{flange}} - \phi_{\text{bottom}}$ and we neglect the field in the web. For web actuation $V = \phi_{\text{web}} - \phi_{\text{bottom}}$ and we neglect the field in the flanges.

The governing equations are obtained using the principle of virtual work. The potential energy of the T-beam actuator is

$$\begin{aligned} U_b &= \int_{V_b} \frac{E}{2} (u' - x_2 v'' - x_3 w'')^2 dV, \\ U_p &= \int_{V_p} H dV, U = U_b + U_p, \end{aligned} \quad (4.2)$$

where $()' = \frac{d()}{dx_1}$, E is the Young's modulus of PZT, U_b and U_p are the potential energy of the passive region and active region, respectively, and U is the total potential energy.

The electric enthalpy H for the active piezoelectric material, obtained from piezoelectric constitutive equations [69, 32] and electric boundary conditions $V = \phi_{\text{web}} - \phi_{\text{bottom}}$ and $V = \phi_{\text{flange}} - \phi_{\text{bottom}}$ for web and flange actuations, respectively, is given by

$$\begin{aligned} H &= \frac{E}{2} (u'')^2 + \frac{E}{2} x_2^2 (v'')^2 - E x_2 u' v'' + (a_2 x_3^2 + a_3) (w'')^2 \\ &+ a_4 V w'' + a_5 V^2 + (a_6 + a_7 x_3) w'' u' - (a_7 x_2 x_3 + a_6 x_2) w'' v'' \\ &+ a_8 V u' - a_8 V x_2 v'', \end{aligned} \quad (4.3)$$

Table 4.1. Electromechanical coefficients for web and flange actuation

Coefficient	Web	Flange
a_2	$\frac{1}{2} \left(E + \frac{e_{31}^2}{\epsilon_{33}} \right)$	$\frac{1}{2} \left(E + \frac{e_{31}^2}{\epsilon_{33}} \right)$
a_3	$-\frac{e_{31}^2(2e+h-2t)^2}{8\epsilon_{33}}$	$-\frac{e_{31}^2(2e-t)^2}{8\epsilon_{33}}$
a_4	$-\frac{e_{31}(2e+h-2t)}{2h}$	$-\frac{e_{31}(2e-t)}{2t}$
a_5	$\frac{-\epsilon_{33}}{2h^2}$	$\frac{-\epsilon_{33}}{2t^2}$
a_6	$\frac{e_{31}^2}{2\epsilon_{33}}(2e+h-2t)$	$\frac{e_{31}^2}{2\epsilon_{33}}(2e-t)$
a_7	$-\frac{E\epsilon_{33} + e_{31}^2}{\epsilon_{33}}$	$-\frac{E\epsilon_{33} + e_{31}^2}{\epsilon_{33}}$
a_8	$\frac{e_{31}}{2h}$	$\frac{e_{31}}{2t}$

where $e_{31} = Ed_{31}$ is piezo-electric stress coefficient, and $\epsilon_{33} = K\epsilon_0$ is the permittivity of PZT [32]. The coefficients in Eq. (4.3) are given in Table 4.1 for web and both flange actuation and d_{31} is the piezoelectric strain coefficient, K is relative permittivity of PZT, and ϵ_0 is the permittivity of free space.

Substitution of Eqs. (4.2) into the principal of virtual work,

$\int_0^t (\delta U + F_2 \delta v(L) + F_3 \delta w(L)) dt = 0$, produces the field equations

$$\frac{d^4 w(x_1)}{dx_1^4} = 0, \frac{d^4 v(x_1)}{dx_1^4} = 0, \frac{d^2 u(x_1)}{dx_1^2} = 0, \forall x \in (0, L), \quad (4.4)$$

geometric boundary conditions at the fixed end

$$u(0) = 0, v(0) = 0, w(0) = 0, \frac{dv(0)}{dx} = 0, \frac{dw(0)}{dx} = 0, \quad (4.5)$$

and the natural boundary conditions at the free end

$$\begin{aligned} E(A_b + A_p) \frac{du(L)}{dx} + a_8 A_p V &= 0, \\ E(I_{p2} + I_{b2}) \frac{d^2v(L)}{dx_1^2} - a_8 A_{p2} V &= 0, \\ E(I_{p2} + I_{b2}) \frac{d^3v(L)}{dx_1^3} - F_2 &= 0, \\ (EI_{b3} + 2a_2 I_{p3} + 2a_3 A_p) \frac{d^3w(L)}{dx_1^3} - F_3 &= 0, \\ (EI_{b3} + 2a_2 I_{p3} + 2a_3 A_p) \frac{d^2w(L)}{dx_1^3} + a_4 A_p V &= 0, \end{aligned} \quad (4.6)$$

where (A_p, A_b) , (A_{p2}, A_{b2}) , (I_{p2}, I_{b2}) , and (I_{p3}, I_{b3}) are the cross-sectional area, first moment of area, and second moment of area of the active and passive regions, respectively, about the neutral axis as given in Tab. 4.2.

The solutions of Eqs. (4.4) are

$$\begin{aligned} u(x_1) &= b_1 x_1 + b_0, \\ v(x_1) &= c_3 x_1^3 + c_2 x_1^2 + c_1 x_1 + c_0. \\ w(x_1) &= d_3 x_1^3 + d_2 x_1^2 + d_1 x_1 + d_0. \end{aligned} \quad (4.7)$$

The 10 unknown coefficients b_j , c_i , d_i are solved analytically using the 10 boundary

Table 4.2. Cross-sectional area, first moment of area, and second moment of area for web, flange and, single flange actuation

Constant	Web	Flange	Single flange
A_b	$t(s-b)$	bh	$\frac{(2h-t)b+st}{2}$
A_p	bh	$t(s-b)$	$\frac{(s-b)t}{2}$
A_{p2}	0	0	$\frac{t(s^2-b^2)}{8}$
I_{b2}	$\frac{t}{12}(s^3-b^3)$	$\frac{b^3h}{12}$	$\frac{(2h-t)b^3+s^3t}{24}$
I_{p2}	$\frac{b^3h}{12}$	$\frac{t}{12}(s^3-b^3)$	$\frac{t(s^3-b^3)}{24}$
I_{b3}	$\frac{(s-b)t^3}{12}$ $+A_b\left(e-\frac{t}{2}\right)^2$	$\frac{bh^3}{12}$ $+A_b\left(e-t+\frac{h}{2}\right)^2$	$I_{p3}+\frac{bh^3}{12}$ $+bh\left(e-t+\frac{h}{2}\right)^2$
I_{p3}	$\frac{bh^3}{12}$ $+A_p\left(e-t+\frac{h}{2}\right)^2$	$\frac{(s-b)t^3}{12}$ $+A_p\left(e-\frac{t}{2}\right)^2$	$\frac{(s-b)t^3}{24}$ $+A_p\left(e-\frac{t}{2}\right)^2$

conditions to obtain

$$\begin{aligned}
 w(x_1) &= \frac{-(LF_3 + a_4VA_p)x_1^2}{2(2a_2I_{p3} + 2a_3A_p + E_pI_{b3})} + \frac{F_3x_1^3}{6(2a_2I_{p3} + 2a_3A_p + E_pI_{b3})}, \\
 v(x_1) &= \frac{(-LF_2 + a_8VA_{p2})x_1^2}{2E_p(I_{p2} + I_{b2})} + \frac{F_2x_1^3}{6E_p(I_{p2} + I_{b2})},
 \end{aligned} \tag{4.8}$$

The tip displacements obtained by substituting $x_1 = L$ in Eq. (4.8) are

$$\begin{aligned} v(L) &= -\frac{L^3 F_2}{3E_p (I_{p2} + I_{b2})} + \frac{a_8 A_{p2} L^2 V}{2E_p (I_{p2} + I_{b2})}, \\ w(L) &= -\frac{L^3 F_3}{3(2a_2 I_{p3} + 2a_3 A_p + E_p I_{b3})} - \frac{a_4 A_p L^2 V}{2(2a_2 I_{p3} + 2a_3 A_p + E_p I_{b3})}, \end{aligned} \quad (4.9)$$

The free tip displacements, v_f and w_f defined as the displacement at the tip of actuator when the applied force F_2 and F_3 equal to zero. From Eq. (4.9) the expressions for free displacement can be obtained as

$$\begin{aligned} v_f &= \frac{a_8 A_{p2} L^2 V}{2E_p (I_{p2} + I_{b2})}, \\ w_f &= -\frac{a_4 A_p L^2 V}{2(2a_2 I_{p3} + 2a_3 A_p + E_p I_{b3})}, \end{aligned} \quad (4.10)$$

are obtained by substituting $F_2=F_3=0$ in Eq.4.9. The blocking forces,

$$\begin{aligned} F_{2b} &= -\frac{3a_8 A_{p2} V}{2L}, \\ F_{3b} &= \frac{3a_4 A_p V}{2L} \end{aligned} \quad (4.11)$$

constrain the tip displacements $v(L)=w(L)=0$ in Eq.4.9.

4.3.1 Nondimensional modeling

Two nondimensionalization schemes are used to validate the model and optimize the T-beam performance. For the model validation nondimensionalization, we reduce the parametric model to a simple linear relationship between the nondimensional voltage

and the nondimensional displacements and blocking forces. In this way, all of the obtained experimental data can be shown on one plot, regardless of the device parameters.

The nondimensional parameters

$$x_1^* = \frac{x_1}{L}, w^* = \frac{w}{L}, v^* = \frac{v}{L}, \quad (4.12)$$

are introduced into Eq. 4.4 to produce

$$w^*(1) = F_3^* + V_3^*, v^*(1) = F_2^* + V_2^*, \quad (4.13)$$

where the nondimensional forces and voltages in the out-of-plane and in-plane directions are

$$F_2^* = -\frac{\kappa}{3\gamma}, F_3^* = -\frac{\beta}{3\alpha}, V_2^* = -\frac{\psi}{2\gamma}, V_3^* = -\frac{\tau}{2\alpha}, \quad (4.14)$$

with the parameters

$$\begin{aligned} \alpha &= 1 + \frac{2a_2 I_{p3}}{EI_{b3}} + \frac{2a_3 A_p}{EI_{b3}}, \beta = \frac{F_3 L^2}{EI_{b3}}, \tau = \frac{a_4 V A_p L}{EI_{b3}}, \\ \gamma &= 1 + \frac{I_{p2}}{I_{b2}}, \kappa = \frac{F_2 L^2}{EI_{b2}}, \psi = -\frac{a_8 V A_{p2} L}{EI_{b2}}, \end{aligned} \quad (4.15)$$

From Eq. (4.13) the nondimensional free tip displacements

$$v_f^* = V_2^*, w_f^* = V_3^*, \quad (4.16)$$

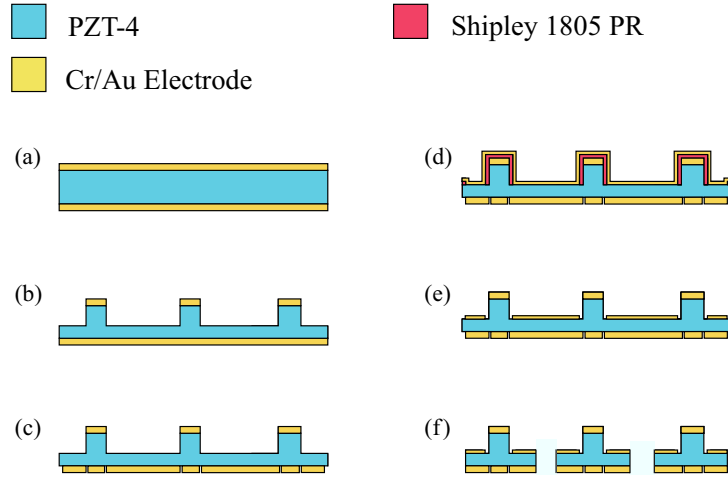


Figure 4.4. Schematic illustration of T-beam fabrication: (a) start with 1mm thick bulk PZT-4 with Cr/Au coating, (b) dice to form web regions, (c) etch bottom electrodes, (d) spray photoresist pattern and evaporate Cr/Au for flange electrodes, (e) lift-off photoresist to form flange electrodes, (f) release individual T-beams by dicing.

and the non-dimensional blocking forces

$$F_{2b}^* = -V_2^*, F_{3b}^* = -V_3^*. \quad (4.17)$$

4.4 Fabrication Process

A schematic illustration of the T-beam fabrication process using a precision dicing saw and photolithography is shown in figure 4.4. We start with a 25.4 X 25.4 mm X 1 mm PZT-4 chip with both sides polished and coated with a layer of Cr/Au as shown in figure 4.4(a). The web regions are defined using a K & S Model 980 precision dicing saw (Fig. 4.4(b)). Height calibration ensures $\pm 10 \mu\text{m}$ resolution in the vertical direction. A resolution of approximately $20 \mu\text{m}$ is obtained in the horizontal direction. A thick

layer of Shipley 1827 photoresist spun using a Model PWM32 Headway Research, Inc spinner at 1000 rpm for 20 seconds and cured at 115°C protects the uncut PZT from particles created during dicing and is then removed in acetone and IPA.

High quality, precleaned VWR microscope glass slides function as sample holders for the PZT chip using Shipley 1827 (1000 RPM, 20 seconds, 115 °C for 15 minutes) as mounting adhesive. The PZT is mounted upside down and spin coated with Shipley 1827 (3000 RPM, 40 seconds, 115 °C for 15 minutes). The Karl Suss MJB-3 Contact aligner provides 0.9 mW/cm² at 315 nm of exposure and transparency masks drawn in Corel Draw X4 provide sufficient resolution (approximately 50 μm) to pattern the bottom electrodes. The large thickness of the photoresist requires a high exposure time (7 minutes) as compared to conventional silicon processes. The chip is developed in 3:1 Microposit™ 351 developer and DI water for one minute. Gold etchant-Type TFA and Chrome etchant-Type 1020 defines the bottom electrode and a Cole Parmer 8892 ultrasonic bath of acetone unmounts the chip as shown in figure 4.4(c). After cleaning, the chip is remounted right side up and spray coated with Shipley 1805 photoresist (115 °C, 10 minutes) using a Badger Model 250 spray gun. The flange electrode mask is then aligned, patterned, and inspected under a microscope. Significant nonuniformity in the S1805 spray coat and the high aspect ratio of the sample require multiple exposures at very high exposure times (> 14 minutes). A conformal layer of 15 nm Cr and 150 nm Au are evaporated onto the substrate using a planetary sample holder on an electron beam evaporator with a MDC Mighty Source™ as shown in figure 4.4(d). An ultrasonic

Table 4.3. Fabricated prototype parameters

Device	Length L (mm)	Total width s (μm)	Flange thickness t (μm)	Height h (μm)	Web width b (μm)
1	14.6	2012	134	1000	765
2	20.4	2008	298	1000	774
3	20.1	2000	417	1000	764
4	20.4	1993	612	1000	756
5	21.3	2017	788	1000	770
6	20.7	1995	320	1000	512

acetone bath performs the liftoff procedure removing photoresist and gold from the undesired areas as shown in figure 4.4(e). The final T-beams are released by dicing (see figure 4.4(f)).

The T-Beams are then packaged onto custom designed PCBs and wirebonded using a K&S Model 4524 wirebonding machine. Due to high surface roughness of flange H20E EPO-TEK® silver conductive epoxy is used to hold the 25 μm gold wirebond to the flange and cured at 115 °C. In total, 6 independent electrodes (3 on top and 3 on bottom) enable actuation of T-beam in both out-of-plane and in-plane directions.

4.5 Prototyping and Experimental Setup

Six devices are built with the different configurations shown in Table 4.3. Five of the devices have different flange thicknesses and approximately same length and web thickness except for first one which had its tip broken off during fabrication. Figure 4.5 shows the picture of fabricated and mounted Device 4. The inset zooms in on the cross-section

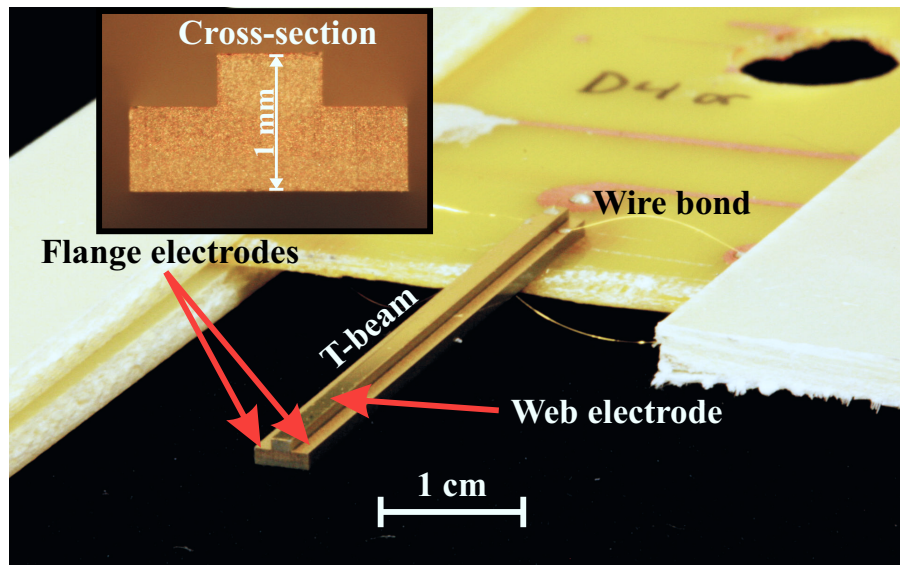


Figure 4.5. Photograph of a fabricated and mounted T-beam (Device 4) actuator.

of T-beam at the tip. The 0.8 mm thick FR4 circuit board is attached along its edges thicker 1.6 mm FR4 base which then is attached to linear stages that allow precise positioning of the actuator. High resolution pictures of cross-section, top-view, and bottom view of each device are used to measure the various geometric parameters with a precision of approximately $\pm 20 \mu\text{m}$ in cross-sectional dimensions and $\pm 50 \mu\text{m}$ in length. The material properties of PZT-4 used for T-beams are given in table 4.4.

The experimental setup used to measure the displacement and blocking force of the actuators is shown in figure 4.6. A model OFV5000 Polytec laser vibrometer controller with OFV534 sensor head measures the displacement with a measuring spot size of $20 \mu\text{m}$. A 3-axis Newport linear stage with micrometer screws accurately positions the T-beam so that the laser is precisely focused at the desired location. An Aurora 402A force transducer with a 1 mm diameter glass tube sensing tip is used to measure

the blocking force. The force transducer has a resolution of 10 nN and can measure up to 500 mN. The force transducer is mounted on two Aurora linear stages to allow positioning the sensor tip at the desired location on the T-beam. A model 609E6 Trek amplifier generates the desired voltage running.

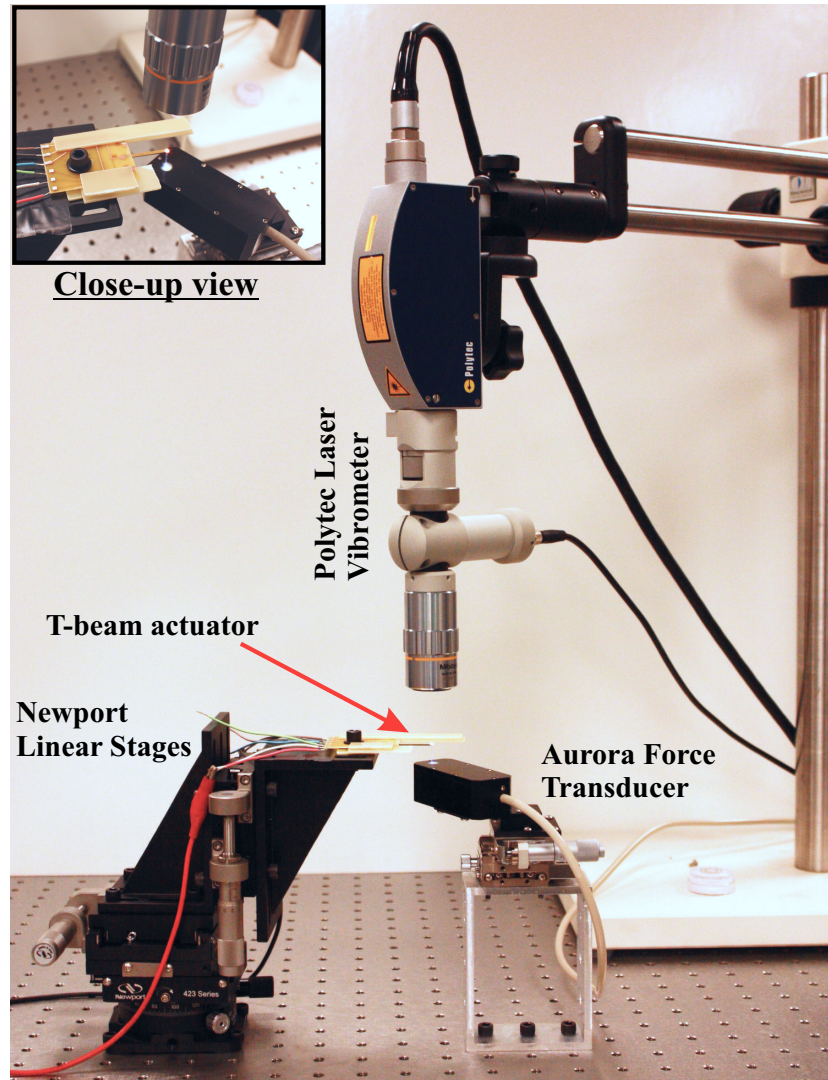


Figure 4.6. Photograph of experimental set-up to measure displacement and blocking force of T-beam actuators.

Table 4.4. PZT-4 material properties

Description	
Youngs modulus of PZT, E (GPa)	78
Piezoelectric strain coefficient, d_{31} (C/N)	-122e-12
Permittivity of PZT, ϵ_{33} ($C^2/(Nm^2)$)	1.15e-08

4.6 Experimental Testing and Validation

The six independent electrical connections on the fabricated T-beams enable web, flange, right flange or left flange actuation to produce out-of-plane and in-plane motions. Blocking force measurements are performed only for web and flange actuations due to the difficulty in measuring transverse forces.

A triangle wave signal at 1 Hz frequency (total 10 cycles) actuates the T-beam such that the electric field ϕ is always in the direction of poling. The experiment is repeated for peak electric fields of 0.1, 0.2, 0.3, 0.4, 0.5 V/ μ m for both displacement and blocking force measurements. The peak voltage applied is $V = \phi h$ for web actuation and $V = \phi t$ for flange actuation and the un-actuated electrodes are allowed to float. To account for the compliance of force sensor and FR4 mounting, displacement measurements are taken at the tip and base of the T-beam actuator during blocking force measurements.

Figure 4.7 shows the out-of-plane free tip displacements w_f of device 3 for different actuations. The yellow, green, red, cyan blue colored lines are the experimental data under triangle wave excitation for applied electric field of 0.5, 0.4, 0.3, 0.2, 0.1 V/ μ m, and the symbols are averages over 10 cycles. Similarly, Fig. 4.8 shows the experimen-

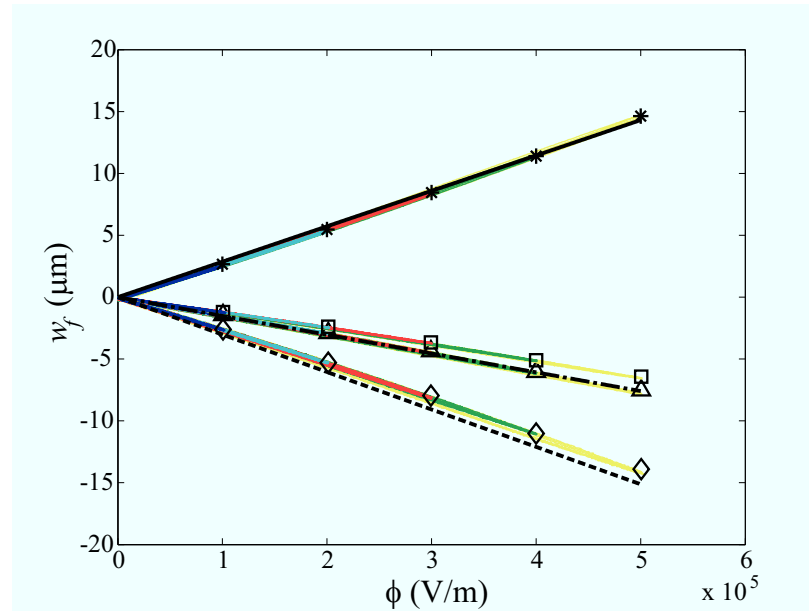


Figure 4.7. Applied electric field ϕ versus free tip out of plane displacement w_f for Device 3: Theoretical (solid - web actuation, dashed - flange actuation, dashdot - right or left flange actuation) and experimental (star - web actuation, diamond - flange actuation, square - left flange, and triangle - right flange).

tal and analytical in-plane free tip displacement v_f versus applied electric field ϕ . The data shows that the analytical predictions closely match the displacement magnitude and trend for the T-beam actuator. The experimental T-beams are not rigidly clamped at the base because the FR4 circuit board is thinner and softer than the T-beam. The electrodes extend all the way to the end of the beam. Sixty percent of the "clamped" region is included in the beam length to model this effect. The experimental displacements are proportional to the applied field. Web and both flange actuation produce similar displacements in opposite directions. Single flange actuation produces less out of plane displacement and, as they should, the left and right flange actuation cases produce similar displacements.

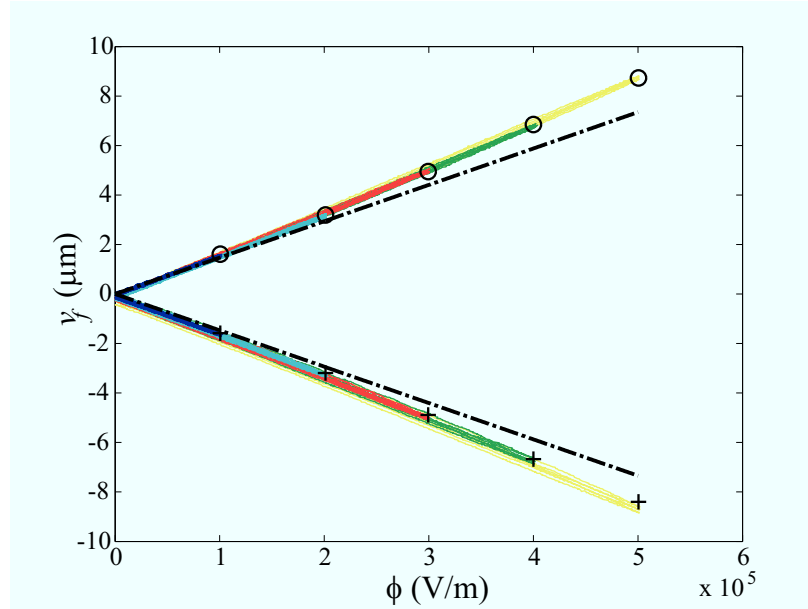


Figure 4.8. Applied electric field, ϕ versus in-plane tip displacement, v_f for Device 3: theoretical (dashdot - Right flange (top), left flange (bottom)) and experimental (plus - left flange, circle - right flange).

The compliance of the FR4 circuit board also affects the blocking force measurements. As a result, perfect clamped boundary conditions could not be realized. Accordingly, the force F_3 is calculated (from Eq.(4.9)) as

$$F_3 = -\frac{3a_4VA_p}{2L} - \frac{3(2a_2I_{p3} + 2a_3A_p + E_pI_{b3})w_{\text{exp}}}{L^3}, \quad (4.18)$$

and is shown for device 3 in Fig. 4.9 for web and flange actuations, where, w_{exp} is the measured displacement of T-beam with tip force. The analytical model predicts the trend accurately but slightly overpredicts the magnitude. The results are linear with applied field and the web and flange actuation produce similar blocking forces at similar field.

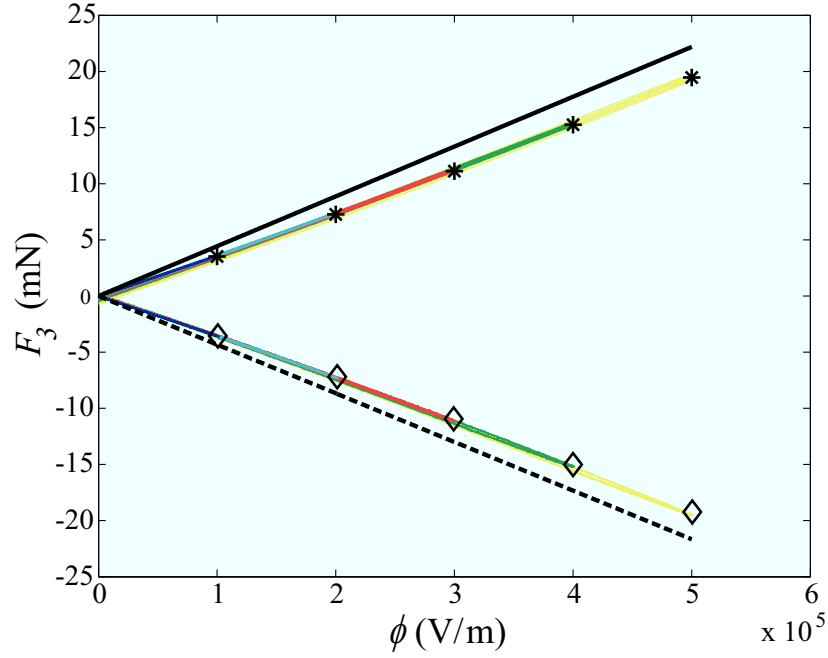


Figure 4.9. Applied electric field ϕ versus tip force, F_3 for Device 3: Theoretical (solid - web actuation, dashed - flange actuation) and experimental (star - web actuation, diamond - flange actuation).

It should be noted, however, that flange actuation uses less voltage because the flange is thinner than the web. For further analysis, the force measurements are corrected with the measured displacement using Eqns. (4.9) and (4.13) to obtain blocking force as

$$(F_{3b})_{\text{exp}} = (F_3)_{\text{exp}} + \frac{3(2a_2I_{p3} + 2a_3A_p + E_pI_{b3})w_{\text{exp}}}{L^3}, \quad (4.19)$$

$$(F_{3b}^*)_{\text{exp}} = (F_3^*)_{\text{exp}} - w_{\text{exp}}^*,$$

Figure 4.10 shows the nondimensional analytical and experimental displacements v_f^* , w_f^* versus nondimensional voltage V_2^* and V_3^* , for Devices 1 - 6. The nondimensionalization allows the in-plane and out-of-plane displacement results for all the devices

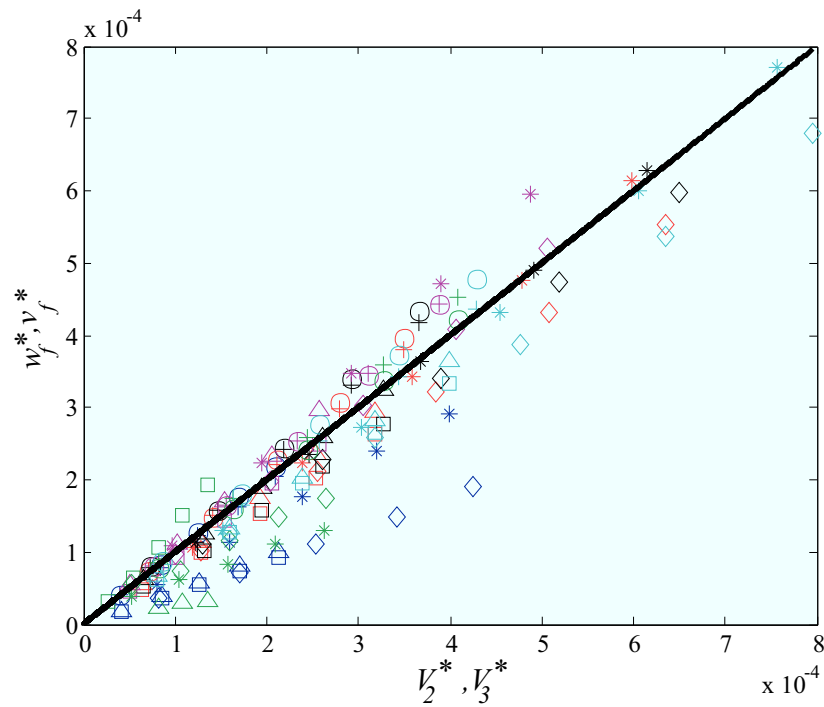


Figure 4.10. Non-dimensional voltage, V_2^* , V_3^* , versus displacement, v_f^* , w_f^* , for Devices 1 - 6: Theoretical (solid) and experimental (star - web actuation, diamond - flange actuation, square or plus - left flange, triangle or circle - right flange actuation).

in all actuation modes to be plotted against the one theoretical line. Different symbols denote different types of actuation and each color represents a different device. From the plot, it can be seen, that the analytical model in general closely predicts the trend and magnitude of all the devices. A linear fit to the data has a slope of 43.3° within 3.8% of the analytical slope of 45° . The 95% confidence interval has a lower limit of 42.5° and an upper limit of 44.1° . Device-1 (blue) has inferior flange electrodes that produce poor performance in flange actuation. Device 4 (magenta) in web actuation, however, produced higher displacements than predicted by theory.

Figure 1.10 shows the dimensionless blocking force F_{3b}^* for Devices 1 - 6 versus

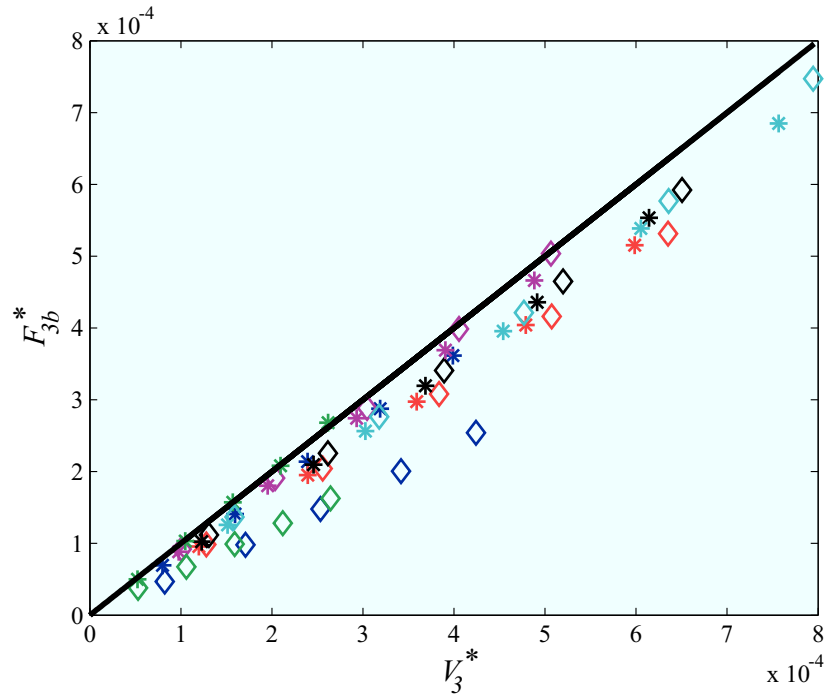


Figure 4.11. Non-dimensional blocking force F_{3b}^* versus nondimensional voltage V_3^* for Devices 1 to 6: Theoretical (solid) and experimental (star - web actuation, diamond - flange actuation).

dimensionless voltage V_3^* . The best fit line for the experimental data has a slope of 41.2° , within 8% of the theoretical slope of 45° . The 95% confidence interval of slope has a lower limit of 40.5 and a upper limit of 41.9. Again, the flange actuation cases slightly underperform web actuation, probably due to incomplete coverage of the flanges by the deposited electrodes.

4.7 Optimization of the T-beam Cross Section

In this section, we optimize T-beam actuators for maximum tip displacement, blocking force, and mechanical energy by varying the cross section geometry. To generalize the

optimization results, we define six, independent, non-dimensional parameters,

$$\begin{aligned} b^* &= \frac{b}{s}, t^* = \frac{t}{h}, s^* = \frac{s}{h}, L^* = \frac{L}{h}, \\ M^* &= \frac{E d_{31}^2}{\epsilon_{33}}, \text{ and } \phi^* = d_{31} \phi. \end{aligned} \quad (4.20)$$

The first four parameters are geometry dependent. The non-dimensional parameters b^* and t^* are the percentage of web width and flange thickness with respect to total width, s , and total height, h , of the actuator cross section. These two parameters are inversely proportional to the material removed during the fabrication process. s^* is the aspect ratio of the enclosure from which T-beam is fabricated and L^* is the slenderness of the T-beam. M^* is a non-dimensional material parameter that depends on mechanical, electrical, and electromechanical coupling coefficients. For a given material, M^* is constant. ϕ^* is the nondimensional electric field, where $\phi = \frac{V}{t}$ for flange actuation and $\phi = \frac{V}{h}$ for web actuation. The free tip displacement, w_f and the blocking force F_{3b} are normalized as

$$w_f^{**} = \frac{w_f}{L}, F_{3b}^{**} = \frac{F_{3b}}{EL^2}. \quad (4.21)$$

Using Eqns. (4.21), (4.20), (4.10) and (4.11) we can obtain the nondimensional tip displacements, w_{flange}^{**} and w_{web}^{**} , and blocking forces $F_{b3flange}^{**}$ and F_{b3web}^{**} for flange and

web actuations, respectively, in terms of the non-dimensional parameters

$$\begin{aligned}
 w_{flange}^{**} &= \frac{3L^* \phi^* b^* t^* (1-b^*)(1-t^*)}{\left(\begin{aligned} &(1-b^*)^2 (1+M^*) t^{*4} + b^* t^{*3} (4+M^*) (1-b^*) \\ &-6b^* t^{*2} (1-b^*) + 4b^* t^* (1-b^*) + b^{*2} \end{aligned} \right)}, \\
 F_{3b_{flange}}^{**} &= \frac{3s^* \phi^* b^* t^* (1-b^*)(1-t^*)}{4L^{*3} (b^* + t^* - b^* t^*)}, \\
 w_{web}^{**} &= \frac{3L^* \phi^* b^* t^* (1-b^*)(1-t^*)}{\left(\begin{aligned} &(1-t^*) b^{*2} (t^{*3} - 3t^{*2} + 3t^* - 1 - M^*) \\ &+ 2b^* t^* (t^{*3} - 2t^{*2} + 3t^* - 2 - M^*/2) - t^{*4} \end{aligned} \right)}, \\
 F_{3b_{web}}^{**} &= -\frac{3s^* \phi^* b^* t^* (1-b^*)(1-t^*)}{4L^{*3} (b^* + t^* - b^* t^*)},
 \end{aligned} \tag{4.22}$$

4.7.1 Displacement Optimization

Equation (4.22) shows that the displacements w_{flange}^{**} and w_{web}^{**} are proportional to nondimensional electric field ϕ^* and slenderness L^* . For commercially available PZT materials (e.g. PZT-4 and PZT-5H), M^* ranges from 0.1 to 0.2 and has very little influence on tip displacement. The Equation (4.22) is independent of aspect ratio s^* , so the shape of the bounding rectangle does not influence the displacement. The optimal design of the actuator depends on only b^* and t^* . new non-dimensional displacement

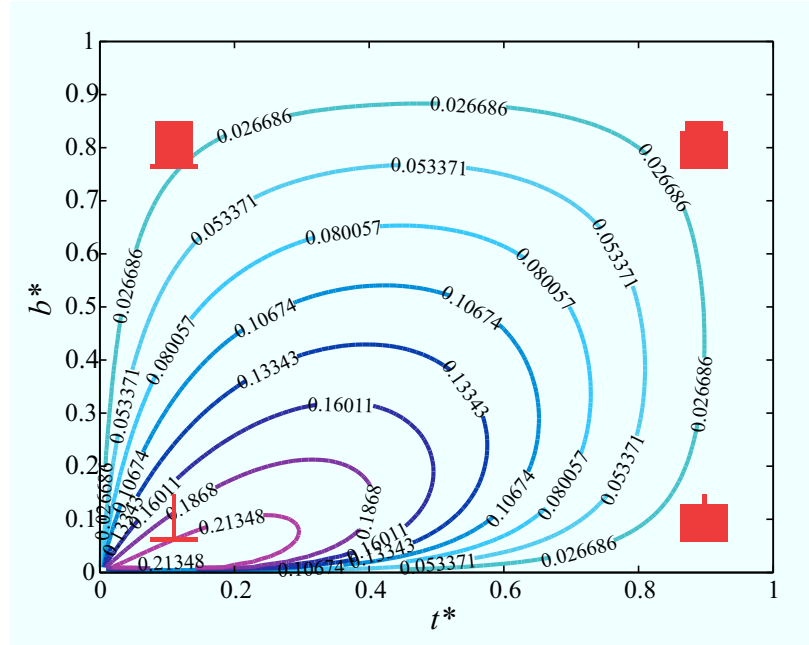


Figure 4.12. Contour plot of nondimensional displacement $(K_w)_{flange}$ versus b^* and t^* for PZT-4 material properties (Tab. 4.4)

parameter K_w for flange and web actuations as a function of b^* , t^* , and M^* as

$$(K_w)_{flange} = \frac{b^*t^*(1-b^*)(1-t^*)}{\left(\begin{array}{l} (1-b^*)^2(1+M^*)t^{*4} + b^*t^{*3}(4+M^*)(1-b^*) \\ -6b^*t^{*2}(1-b^*) + 4b^*t^*(1-b^*) + b^{*2} \end{array} \right)}, \quad (4.23)$$

$$(K_w)_{web} = \frac{b^*t^*(1-b^*)(1-t^*)}{\left(\begin{array}{l} (1-t^*)b^{*2}(t^{*3} - 3t^{*2} + 3t^* - 1 - M^*) \\ + 2b^*t^*(t^{*3} - 2t^{*2} + 3t^* - 2 - M^*/2) - t^{*4} \end{array} \right)},$$

Figure (4.12) is a contour plot of

$$(K_w)_{flange} = \frac{W_{flange}^{**}}{3L^* \phi^*}, \quad (4.24)$$

versus b^* and t^* for the PZT-4 material properties shown in Tab. 4.4. The inset drawings show the cross-section of the T-beam for extreme of b^* and t^* . The contours show that the maximum displacement can be obtained when both b^* and t^* tend towards zero, so the configurations with very thin webs and flanges produce maximum displacements. A similar conclusion can be obtained for web actuation. There exists an optimal t^* for a given b^* for web and flange actuations,

$$t_{web}^* = \frac{b^* - \sqrt{b^*}}{b^* - 1},$$

$$t_{flange}^* = \text{Rootof} \left(\begin{array}{l} 2(-1 + b^*)^2 (1 + M^*) Z^5 + \left(\begin{array}{l} (-7 - 4M^*) b^{*2} - 3M^* \\ + (7M^* + 10)b^* - 3 \end{array} \right) Z^4 \\ + 2b^* (M^* + 4) (b^* - 1) Z^3 + 2(b^* - b^{*2}) Z^2 - 2b^{*2} Z + b^{*2} \end{array} \right), \quad (4.25)$$

respectively.

Figure 4.13 shows the nondimensionalized displacement versus t^* for $b^* = 0.381$ for web (top curve) and flange (bottom curve) actuations. Devices 1 - 6 were designed to span this curve and, as theory predicted, Device 3 (black symbols) is optimal for both flange and web actuation.

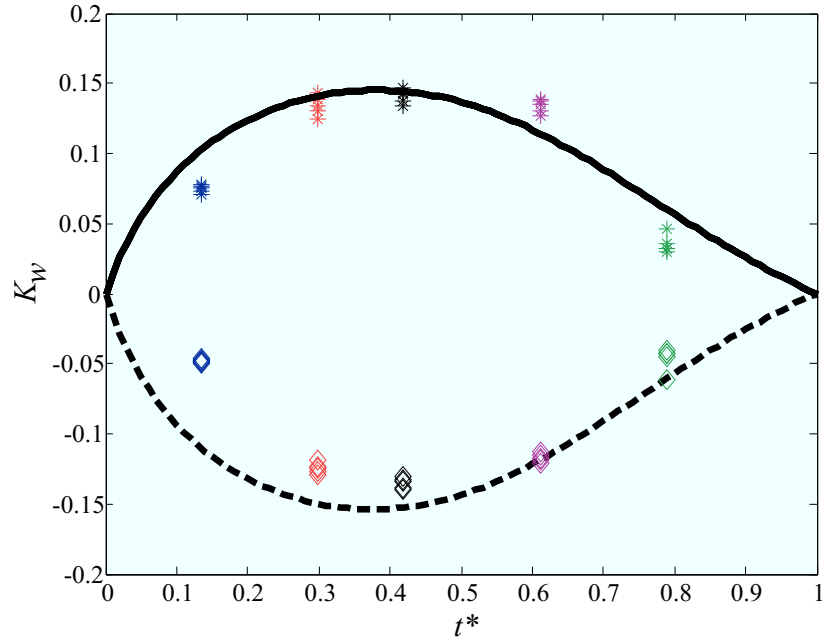


Figure 4.13. Non-dimensional displacement K_w versus t^* for $b^*=0.381$ with PZT-4 material properties for web (theoretical - solid, experimental - star) and flange (theoretical - dashed, experimental - diamond) actuation.

4.7.2 Blocking Force Optimization

From Eq. (4.22), nondimensional blocking force F_{b3}^{**} is independent of the material parameter M^* , is directly proportional to aspect ratio s^* and field ϕ^* , and inversely proportional to L^{*3} . Equation (4.22) shows that T-beams produce equal and opposite blocking forces for web and flange actuations. Hence, there exists a single optimal configuration that maximizes blocking force for both web and flange actuations. As the optimal configuration is dependent only on b^* and t^* , we define nondimensional blocking force K_F as

$$K_F = F_{b3}^{**} \frac{4L^{*3}}{3s^*\phi^*}, \quad (4.26)$$

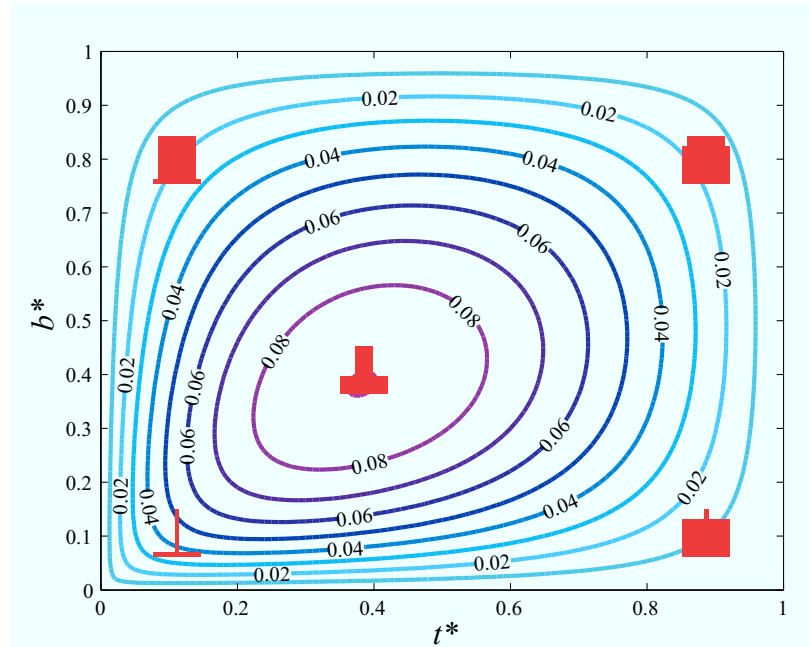


Figure 4.14. Non-dimensional blocking force K_F versus b^* and t^* .

Figure 4.14 shows the contour plot of nondimensional blocking force K_F versus b^* and t^* . The plot shows that there is an optimal solution that maximizes blocking force.

The optimal solution is

$$\frac{\partial (K_F)}{\partial b^*} = 0, \frac{\partial (K_F)}{\partial t^*} = 0, \quad (4.27)$$

or

$$b^* = t^* = \text{Rootof}(Z^2 - 3Z + 1) \approx 0.381. \quad (4.28)$$

T-beams with web widths and flange thicknesses that are 38% of total width and height, respectively, produce maximum blocking force, independent of material properties, field, or slenderness of the actuator and type (web or flange) of actuation.

Figure 4.15 plots the nondimensional blocking force K_F for web (top) and flange

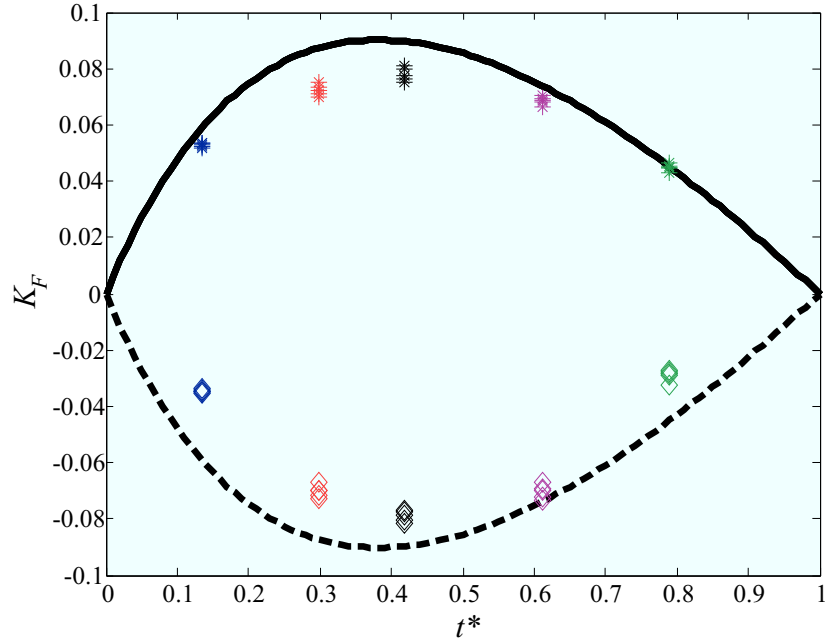


Figure 4.15. Non-dimensional blocking force K_F versus t^* for $b^*=0.381$ for web (theoretical - solid and experimental - star) and flange (theoretical - dashed and experimental - diamond) actuation.

(bottom) actuation. The plot shows that the optimally designed actuator (Device 3 - black) outperforms the other four actuators.

4.7.3 Energy Optimization

Mechanical energy stored in the actuator is defined as $E_M = \frac{1}{2}w_f F_{3b}$. The nondimensional

mechanical energy

$$\begin{aligned} (K_E)_{web} &= \frac{1}{2}(K_w)_{web}K_F, \\ (K_E)_{flange} &= \frac{1}{2}(K_w)_{flange}K_F. \end{aligned} \quad (4.29)$$

Figure 4.16 shows the contour plot of $(K_E)_{flange}$ for flange actuation with PZT-4

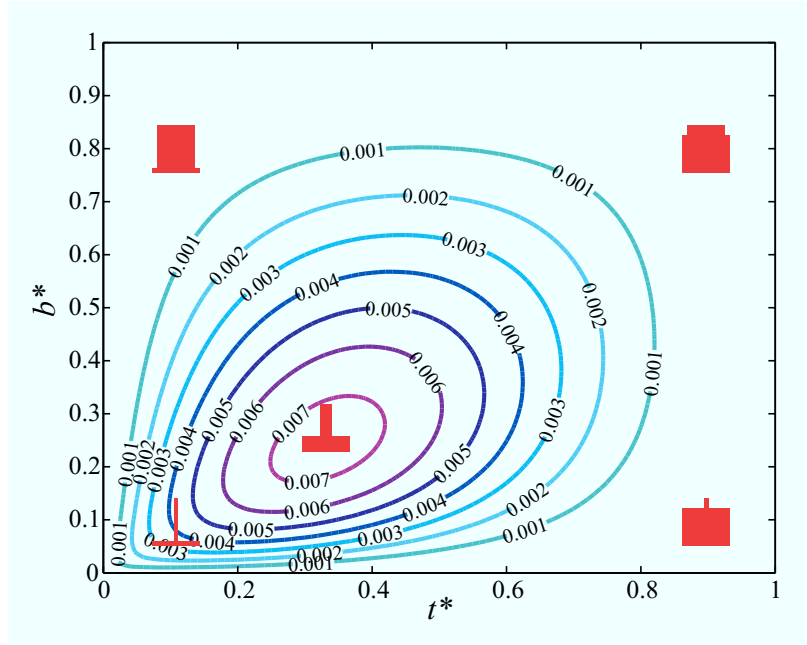


Figure 4.16. Non-dimensional energy parameter K_E versus b^* , t^*

material properties. The plot shows there exists an optimal configuration for a given material. Web actuation shows similar trend. The optimal solution are obtained by the gradient method as

$$b_{web}^* = \frac{1}{M^*} \begin{pmatrix} 24 (\text{Rootof} (12Z^3 - (28 + 2M^*)Z^2 + (20 + 4M^*)Z - M^* - 4))^2 \\ -20 \text{Rootof} (12Z^3 - (28 + 2M^*)Z^2 + (20 + 4M^*)Z - M^* - 4) \\ -4 \text{Rootof} (12Z^3 - (28 + 2M^*)Z^2 + (20 + 4M^*)Z - M^* - 4) M^* \\ + M^* + 4 \end{pmatrix},$$

$$t_{web}^* = \text{Rootof} (12Z^3 - (28 + 2M^*)Z^2 + (20 + 4M^*)Z - M^* - 4), \quad (4.30)$$

for web actuation. Solving the roots numerically for both web and flange actuations

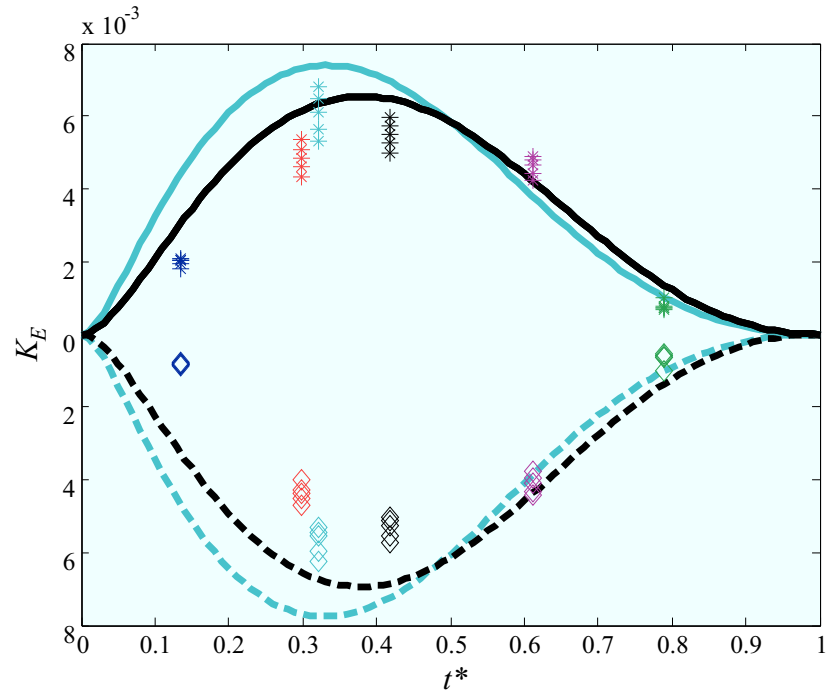


Figure 4.17. Non-dimensional mechanical energy K_E versus t^* for $b^*=0.381$ (theoretical - black solid (web actuation) and black dashed (flange actuation), Experimental - star (web actuation) and diamond (flange actuation)) and $b^*=0.25$ (cyan)

gives $b^* \approx 0.25$ and $t^* \approx 0.33$ for the piezoelectric materials ($M^* = 0.1 - 0.2$) studied.

Figure 4.17 non-dimensional energy K_E for both web (top) and flange (bottom) actuations with $b^* = 0.381$ and the optimal $b^* = 0.25$. The plot clearly shows that the device with optimal design $b^* = 0.25$ exceeds the energy performance of the other actuators.

4.8 Comparison with Unimorph Actuator

To understand the performance of T-beam actuators compared to state-of-the-art piezoelectric actuators, we compare the T-beam actuators with unimorph actuators. The free

tip displacement, w_{fU} and blocking force F_{bU} of unimorph actuators[79, 32] are given by

$$\begin{aligned} w_{fU} &= \frac{6\epsilon_{33}e_{31}L^2\phi}{h(8E\epsilon_{33} + e_{31}^2)}, \\ F_{bU} &= \frac{3e_{31}h^2s\phi}{16L}, \end{aligned} \quad (4.31)$$

where E is the Young's modulus, h is the total thickness of the passive and active layers, and s and L are the total width and cantilevered length of the actuator.

Using PZT-4 material properties, the displacement per unit cross-section area $(w_{fA})_U$ of the unimorph

$$(w_{fA})_U = 9 \times 10^{-11} \frac{L^2\phi}{h^2s}. \quad (4.32)$$

The displacement per unit cross-section area of the T-beam is

$$(w_{fA})_{flange} = \frac{w_{flange}^{**} L}{A} = (w_c)_{flange} \frac{L^2\phi}{h^2s} \approx (w_{fA})_{web}, \quad (4.33)$$

for flange and web actuations, respectively, where

$$(w_c)_{flange} = \frac{-0.366E - 9t^*b^*(t^* - 1)(b^* - 1)}{\begin{pmatrix} 1.1t^{*4} - 2.2b^*t^{*4} + 1.1b^{*2}t^{*4} + 4.1b^*t^{*3} + b^{*2} - \\ 4.1b^{*2}t^{*3} + 6t^{*2}b^{*2} - 6t^{*2}b^* - 4t^*b^{*2} + 4t^*b^* \end{pmatrix} (t^*b^* - t^* - b^*)}, \quad (4.34)$$

Figure 4.18 shows the contour plot of the flange $(w_c)_{flange}$ displacement coefficient versus b^* and t^* . The shaded regions show where the T-beam displacement coefficient is greater than unimorph displacement coefficient. As the web and flange become thinner

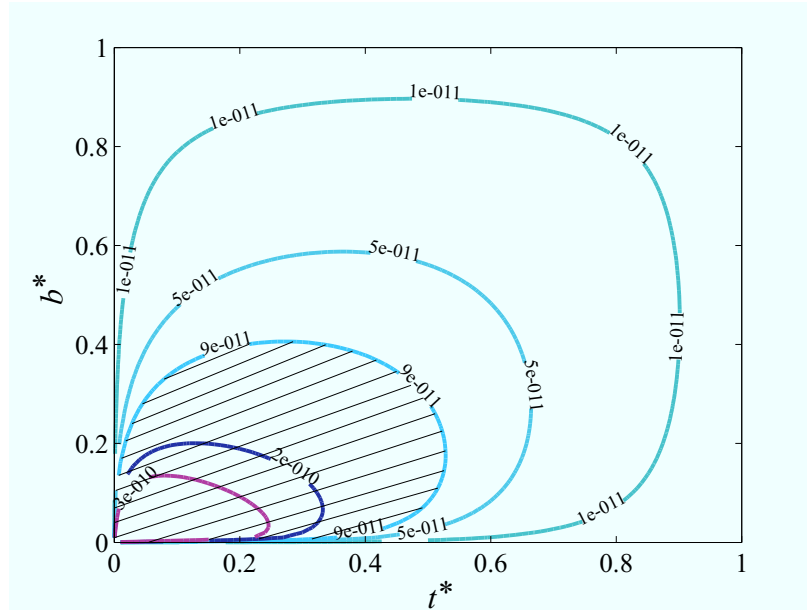


Figure 4.18. Flange displacement coefficient $(w_c)_{flange}$ versus b^* , t^*

we realize higher displacements per unit cross-section area than a unimorph with the same thickness and width. In addition, the voltage required in flange actuation is less than that of a unimorph to produce same field.

The optimal blocking force per unit area of the unimorph is

$$(F_{bA})_U = 1.78 \frac{h\phi}{L}, \quad (4.35)$$

and the blocking force per unit area of T-beam is

$$F_{b3A} = \frac{F_{b3flange}^{**} EL^2}{A} = F_c \frac{h\phi}{L}, \quad (4.36)$$

where the blocking force coefficient F_c is

$$F_c = -\frac{7.137b^*t^*(t^*b^* - t^* + 1 - b^*)}{(t^*b^* - t^* - b^*)^2}, \quad (4.37)$$

and is same in magnitude for both flange and web actuations. F_c is maximum in the limit

$$\lim_{b^*, t^* \rightarrow 0} (F_c) = 1.78, \quad (4.38)$$

so a T-beam with thin webs and flanges approaches the blocking force per unit area produced by a unimorph.

Similarly, the maximum mechanical energy per unit area for the T-beam is maximum and approaches unimorph as both b^* and t^* approach zero for web and flange actuation.

Conclusions

In this research, the design, fabrication, and mechanical model of a novel uniflex microactuator combining the strain amplification mechanisms of a unimorph and flexural motion to produce large displacement and blocking force is presented. Uniflex microactuators can provide displacement performance that exceeds that of similarly sized unimorph actuators if the parameters are properly chosen and as demonstrated by the fabricated uniflex devices in this work. The clearance between the unimorph and the Al cap, for example, must be sufficiently large so that the unimorph and flexural motion strain amplification mechanisms work together to produce large displacement and blocking force. In the experimentally fabricated uniflex actuators, weakened joint enabled a much larger response and was able to predict reasonable well the observed displacement and blocking force of the various actuators tested. Displacement-optimized uniflex designs produce larger displacements than unimorph and flextensional actuators but their blocking force is smaller than the unimorph. Blocking force optimized uniflex

designs outperform flexensional actuators but can only approach the blocking force performance of unimorph actuators.

Also, a novel piezoelectric T-beam actuator is introduced. Analytical models is developed to predict displacement, blocking force, and mechanical energy of T-beam are validated using six successfully fabricated prototypes. Optimization of T-beam cross-section shows that the geometry with ratio of web width b to total width s , b^* , and flange thickness t to total height h , t^* approaching zero produces maximum displacement. Also, the tip displacement is independent of bounding box of T-beam. The cross section with $b^* = t^* = 0.381$ produces maximum blocking force, while, $b^* = 0.25, t^* = 0.33$ produces maximum mechanical energy. A properly designed T-beam has better free tip displacement per unit cross section area than a unimorph. Also, a flange actuated T-beam requires lower voltage than a unimorph to generate same electric field.

5.1 Future Work

For the uniflex actuator, current a spring is modeled to account for inaccuracies in fabrication at the unimorph and aluminum cal interface. The interface can further be studied using fracture mechanics models and further experimentation. For the T-beam actuator, the current model assumes floating electrodes in the passive region. The performance of T-beam under short circuited boundary conditions in the currently passive regions can be studied further. Also, the current work explores the T-beam under uniform electric field across the thickness which necessitates three different bottom ground electrodes.

However, using a continuous bottom electrode would enable greater yield in fabrication. To understand T-beam performance under such conditions, analytical model needs to be developed with two dimensional electric field across the thickness. Also, such a model would help understand the bimorph type actuation of T-beam. (where passive regions are applied electric field in the opposite direction as poling). Further, the models that predict the electromechanical coupling factors and performance with constant tip loads or spring loads would enhance the understanding of the Tbeam actuator. Other cross-sections like I, U, L etc... need to be further explored.

Additional Results for Uniflex Actuator

A.1 Constants for Uniflex Displacement

The constants for uniflex displacement in Eqn. 3.1 are

$$C_1 = - \left(\begin{array}{c} \left(\begin{array}{c} 6K_4K_tL_1^3 - 12K_4(-K_2 + K_t\delta)L_1^2 \\ + (6K_4K_t\delta^2 - 12K_2K_4\delta + 12K_2K_t) \end{array} \right) P_2 \\ L_1 + 12K_2^2 - 12K_2K_t\delta \\ -6 \left(\begin{array}{c} -K_t(-K_3 + K_2)L_1^2 - \\ 2K_3(-K_2 + K_t\delta)L_1 + \\ \delta(K_3 + K_2)(-2K_2 + K_t\delta) \end{array} \right) P_1 \\ + 12P_2K_2K_4(-K_tL_1 + K_t\delta - K_2) - \end{array} \right) K_1$$

$$\begin{aligned}
& K_4 (\delta - L_l)^3 (K_t \delta - K_t L_l - 4K_2) P_2 K_l, \\
C_2 &= -K_4 P_2 K_l (\delta - L_l)^3 (K_t \delta - K_t L_l - 4K_2), \\
C_3 &= \left(\begin{array}{c} (24K_t L_l^2 K_2 K_4 + 24(K_t K_3 + K_2 K_t) K_2) K_l \\ + 24(K_t K_3 + K_2 K_t) K_4 K_2 \end{array} \right), \\
C_4 &= \left(\begin{array}{c} \left(\begin{array}{c} 2(L_l - \delta)^2 (12K_2 + (4L_l - 4\delta) K_t) K_3 + \\ 8(3K_2 \delta^2 + (-\delta^3 + L_l^3) K_t) K_2 \\ + 24(K_2 + K_t (L_l - \delta)) K_3 K_2 \end{array} \right) K_4 \\ + 24(K_2 + K_t (L_l - \delta)) K_3 K_4 K_2, \end{array} \right) K_l \\
C_5 &= 2(L_l - \delta)^3 (4K_2 + K_t (L_l - \delta)) K_3 K_4 K_l, \\
K_1 &= E_a A_a, K_2 = E_a I_a, P_1 = a_8 A_p, P_2 = a_4 A_p, \\
K_3 &= E_b I_{be} + 2a_2 I_{pe} + 2a_3 A_p, K_4 = E_b A_b + E_p A_p.
\end{aligned}$$

A.2 Constants for Uniflex Blocking Force

The constants for uniflex blocking force in Eqn. 3.2 are

$$\begin{aligned}
B_1 &= -3K_2^2 K_l K_t (K_4 + K_l) K_3^2 \\
&\quad - (6K_2^3 K_l K_t (K_4 + K_l) + 3K_2^2 K_l^2 K_t K_4 L_l^2) K_3 \\
&\quad + (-3K_t K_2^2 (K_4 + K_l) - 3K_l K_2 K_t K_4 L_l^2) K_2^2 K_l,
\end{aligned}$$

$$\begin{aligned}
B_2 = & \left(\begin{array}{c} 12(-K_2 + K_t(\delta - L_l))K_2^3K_l(K_4 + K_l) + 2K_2^2K_l^2 \\ K_4 \left(\begin{array}{c} (3\delta L_l - 3\delta^2 - 6L_l^2)K_2 + (\delta - L_l) \\ (11/2L_l^2 - 1/2\delta L_l + \delta^2)K_t \end{array} \right) \end{array} \right) K_3 \\
& + \left(\begin{array}{c} 12(-K_2 + K_t(\delta - L_l))K_2^2K_l(K_4 + K_l) + \\ K_2K_l^2(-3K_2 + K_t(\delta - L_l))(\delta - L_l)^2K_4 \end{array} \right) K_3^2 \\
& + K_l^2K_4(-3K_2\delta^2 + (\delta^3 - L_l^3)K_t)K_2^3,
\end{aligned}$$

$$B_3 = -K_l^2(\delta - L_l)^3K_4(-4K_2 + K_t(\delta - L_l))K_2K_3(K_2 + K_3),$$

$$\begin{aligned}
B_4 = & \left(\begin{array}{c} 36K_tK_2^4(K_4 + K_l)(\delta - L_l) \\ +36K_2^3L_l^2K_lK_tK_4(\delta - L_l) \end{array} \right) K_3 \\
& + 36K_tK_2^3(K_4 + K_l)(\delta - L_l)K_3^2,
\end{aligned}$$

$$\begin{aligned}
B_5 = & \left(\begin{array}{c} -36(-K_2 + K_t(\delta - L_l))K_2^3(K_4 + K_l)(\delta - L_l) \\ -12(-3K_2 + K_t(\delta - L_l))K_l(\delta - L_l)^3K_4K_2^2 \end{array} \right) K_3^2 \\
& - 12K_l(\delta - L_l)K_4K_2^3(-3K_2\delta^2 + (\delta^3 - L_l^3)K_t)K_3,
\end{aligned}$$

$$B_6 = 3K_lK_2^2K_3^2(\delta - L_l)^4K_4(-4K_2 + K_t(\delta - L_l)),$$

$$\begin{aligned}
B_7 = & 3K_3K_lK_2 \left(\begin{array}{c} \left(\begin{array}{c} 12K_tK_2^2K_3 + \\ 4(3L_l^2K_tK_l + 3K_2K_t)K_2^2 \end{array} \right) K_4 \\ + 12K_lK_2(K_tK_2K_3 + K_2K_2K_t) \end{array} \right),
\end{aligned}$$

$$\begin{aligned}
B_8 &= 3K_2K_3K_l \left(\left(\left(\begin{array}{c} (12K_2 + 4K_t(L_l - \delta)) \\ (L_l - \delta)^2 K_3 \\ +4K_2(3K_2\delta^2 + K_t(L_l^3 - \delta^3)) \\ K_4 + 12K_2(K_2 + K_t(L_l - \delta))K_3 \\ K_l + 12K_2(K_2 + K_t(L_l - \delta))K_3K_4 \end{array} \right) \right) \right), \\
B_9 &= 3 \left(K_t K_l K_2 (L_l - \delta)^4 + 4(L_l - \delta)^3 K_2^2 K_l \right) K_3^2 K_4 K_l K_2.
\end{aligned}$$

A.3 Maximum Displacement Design

Figure A.1 shows the variation of optimal clearance L_1 with actuator length L_a for aluminum cap thicknesses $t_a = 1 \mu\text{m}$ and $t_a = 0.3 \mu\text{m}$. For $t_a = 1 \mu\text{m}$, it can be seen that $L_a/L_1 \approx 300$ for the actuators considered. Also, the thickness ratio $t_p/t_b \approx 2$ as shown in Fig. A.2. Figure A.3 shows that the optimal thickness ratio t_p/t_b varies from 2.1 to 1.6 for the actuator length $L_a = 300 \mu\text{m}$.

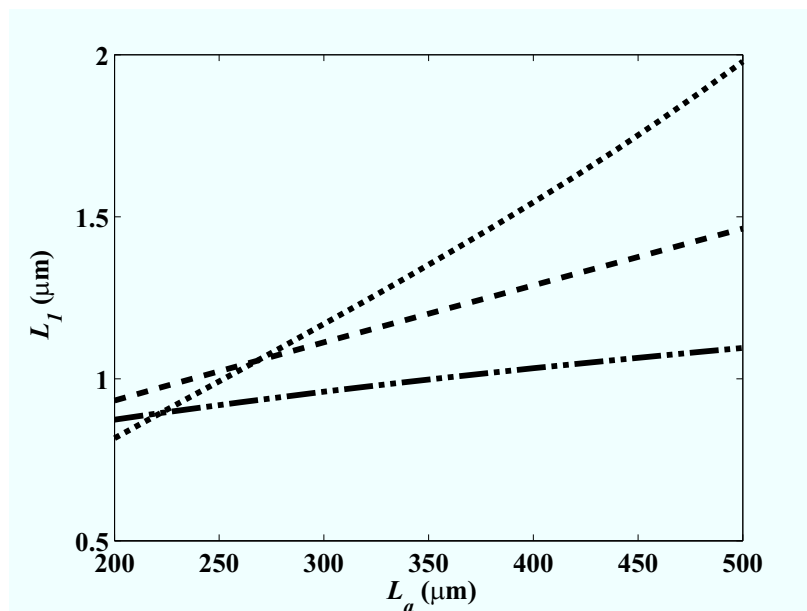


Figure A.1. Clearance L_1 for maximum displacement versus length (L_a): uniflex actuator with $t_a = 1 \mu\text{m}$ (dashed) and $t_a = 0.3 \mu\text{m}$ (dotted), and flextensional actuator with $t_a = 1 \mu\text{m}$ (dash-double dotted).

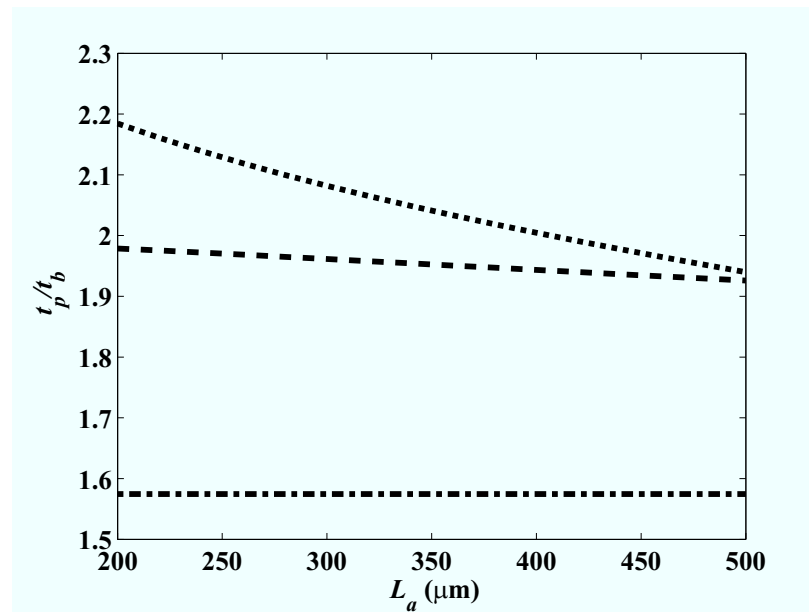


Figure A.2. Ratio t_p/t_b for maximum displacement versus length L_a : unimorph actuator with $t_a = 1 \mu\text{m}$ (dashed) and $t_a = 0.3 \mu\text{m}$ (dotted), and unimorph actuator (dash-dotted).

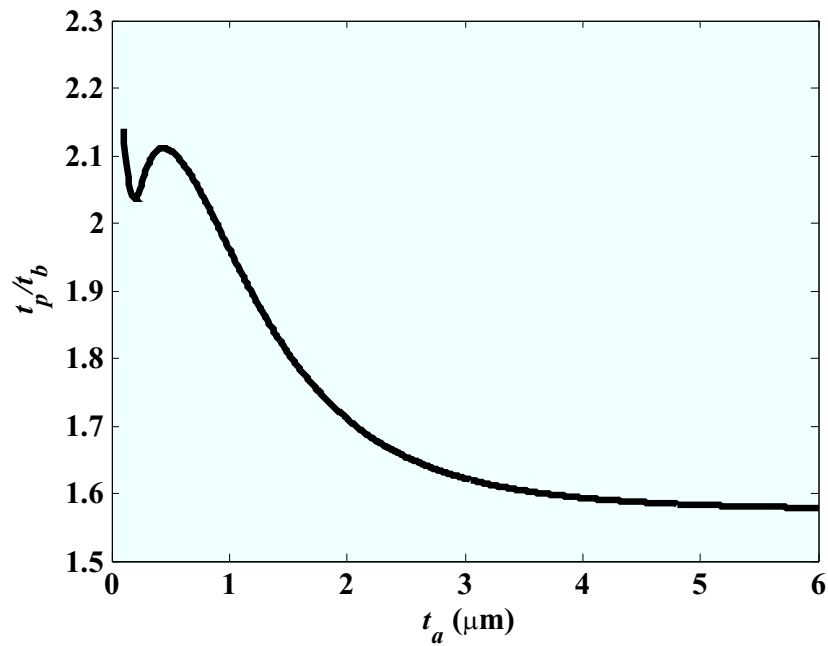


Figure A.3. Uniflex actuator ratio t_p/t_b for maximum displacement versus Al thickness t_a ($L_a = 300 \mu\text{m}$).

A.4 Maximum Displacement Design with Additional Flextensional Actuator Results

Figures A.4 and A.5 show the variation of maximum free displacement and corresponding blocking force F with actuator length $L_a = 200$ to $500 \mu\text{m}$. The results clearly show that the uniflex produces a higher displacement than that of the unimorph and the flextensional actuators when the clearance is optimal (see Fig. A.6). Also, a thinner aluminum cap produces greater displacements.

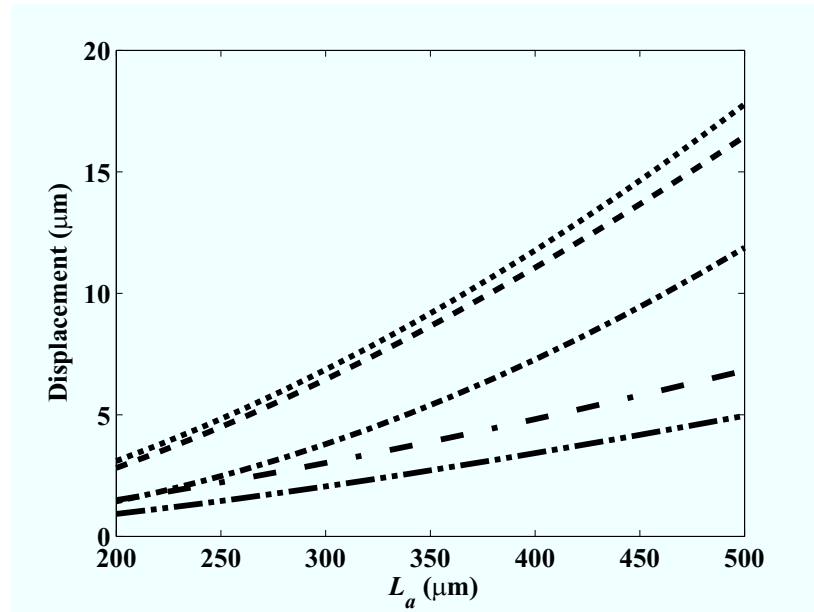


Figure A.4. Maximum displacement versus length L_a : uniflex actuator $w_2(L)$ with $t_a = 1 \mu\text{m}$ (dashed) and $t_a = 0.3 \mu\text{m}$ (dotted), unimorph actuator $w_3(0)$ (dash-dotted), and flextensional actuator $w_2(L)$ with $t_a = 1 \mu\text{m}$ (dash-double dotted) and $t_a = 0.3 \mu\text{m}$ (double dash-dotted).

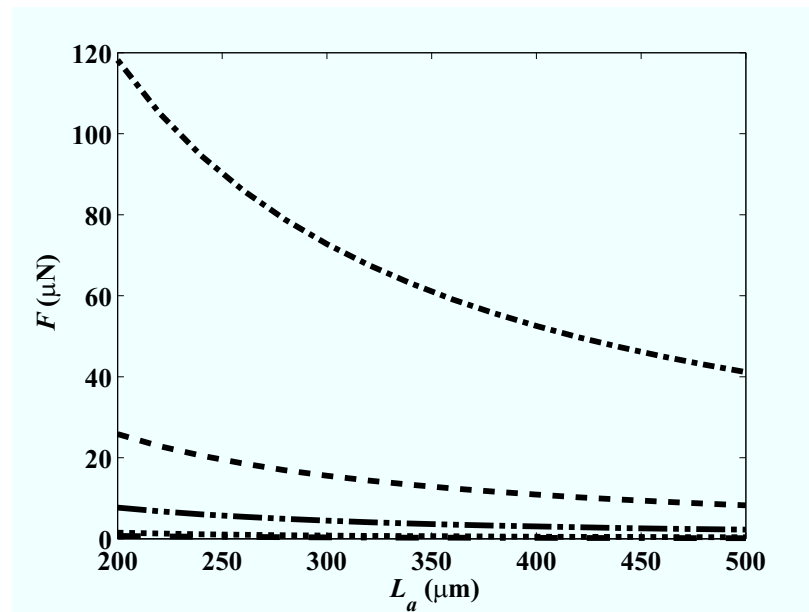


Figure A.5. Blocking force F for maximum displacement configuration versus length L_a : unimorph actuator with $t_a = 1 \mu\text{m}$ (dashed) and $t_a = 0.3 \mu\text{m}$ (dotted), unimorph actuator (dash-dotted), and flextensional actuator with $t_a = 1 \mu\text{m}$ (dash-double dotted) and $t_a = 0.3 \mu\text{m}$ (double dash-dotted).

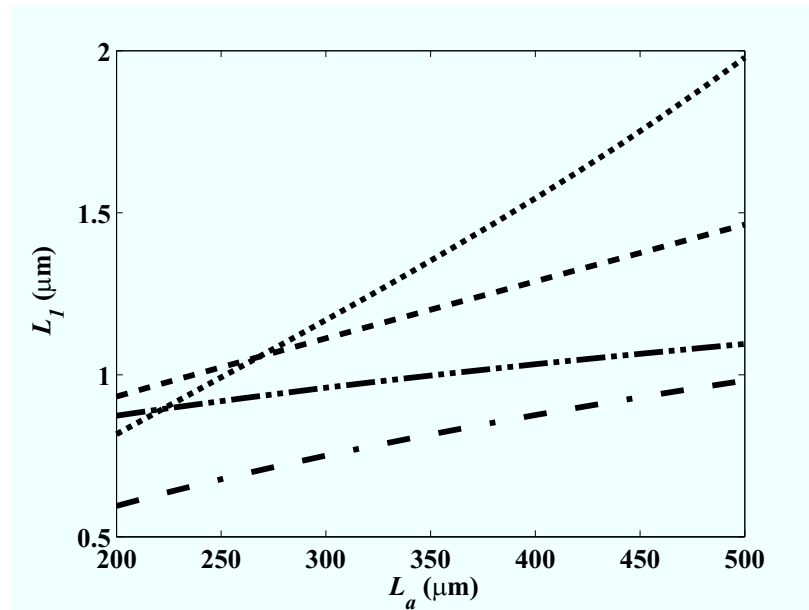


Figure A.6. Clearance L_1 for maximum displacement versus length L_a : uniflex actuator with $t_a = 1 \mu\text{m}$ (dashed) and $t_a = 0.3 \mu\text{m}$ (dotted), and flextensional actuator with $t_a = 1 \mu\text{m}$ (dash-double dotted) and $t_a = 0.3 \mu\text{m}$ (double dash-dotted).

A.5 Maximum Blocking Force Design

Figures A.7 and A.8 show the variation of optimal aluminum cap thickness t_a and thickness ratio t_p/t_b with actuator length L_a for clearances $L_1 = 2.7 \mu\text{m}$ and $L_1 = 2.7 \mu\text{m}$ that produce maximum blocking force. The plot shows that larger clearances and thicker aluminum cap are needed to produce maximum blocking force, whereas, the thickness ratio t_p/t_b remains almost constant (≈ 1.65) for the clearances considered. Fig. A.9 shows that the thickness ratio does not change with clearance as well.

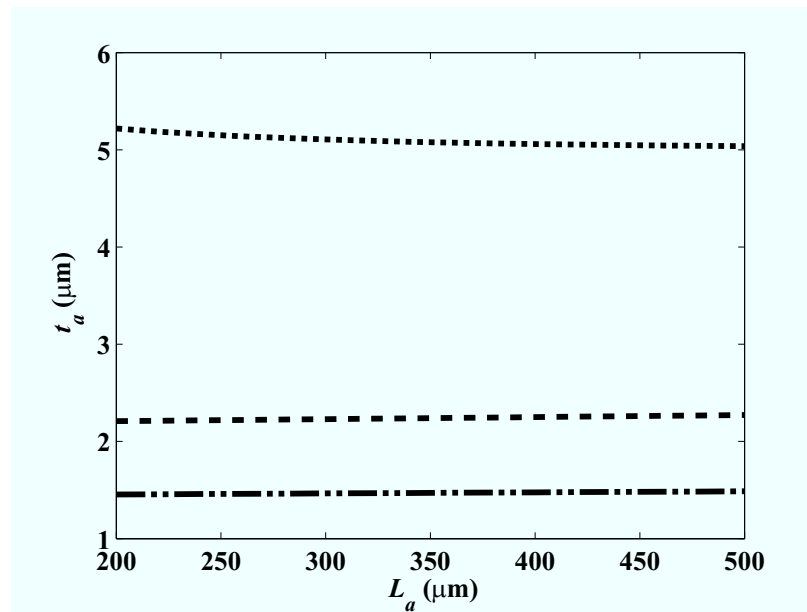


Figure A.7. Al thickness t_a for maximum blocking force versus length L_a : uniflex actuator with clearance $L_1 = 2.7 \mu\text{m}$ (dashed) and $L_1 = 40 \mu\text{m}$ (dotted), and flextensional actuator with $L_1 = 2.7 \mu\text{m}$ (dash-double dotted).

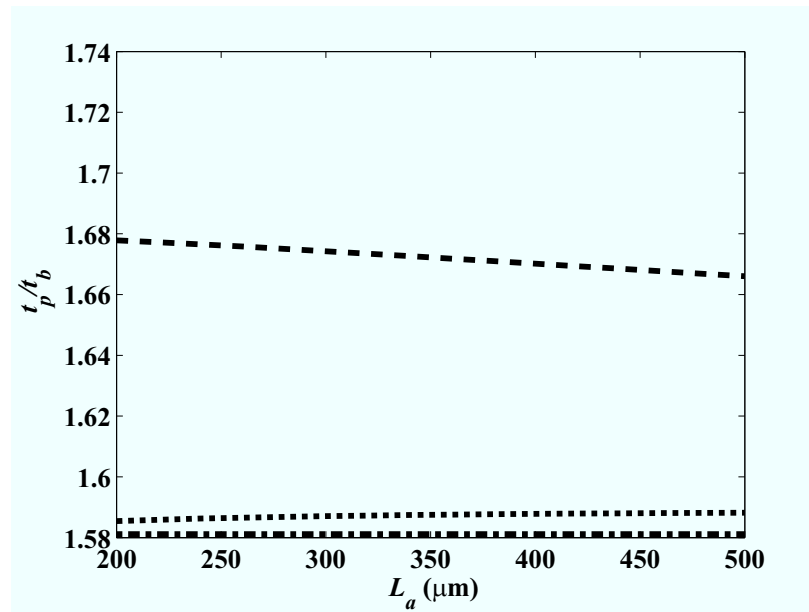


Figure A.8. Ratio t_p/t_b for maximum blocking force versus length L_a : uniflex actuator with clearance $L_1 = 2.7 \mu\text{m}$ (dashed) and $L_1 = 40 \mu\text{m}$ (dotted), and unimorph actuator (dash-dotted).

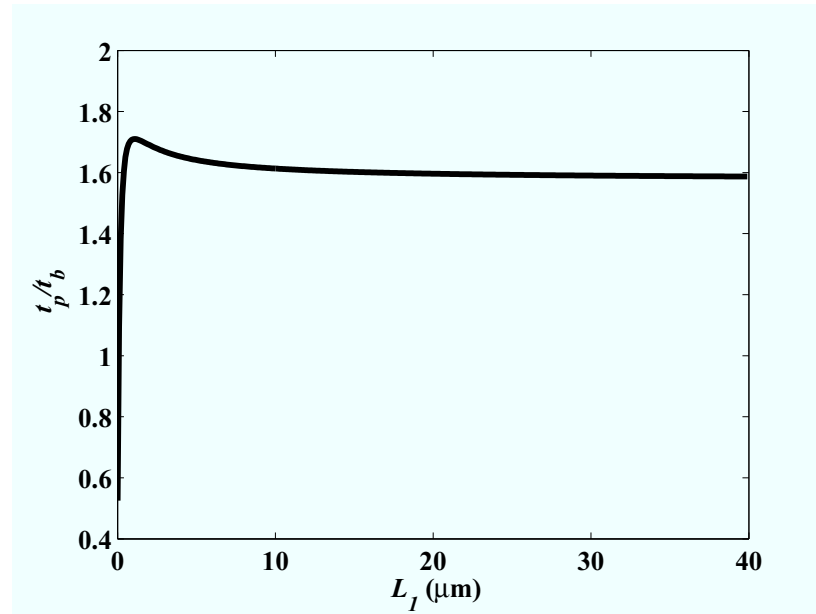


Figure A.9. Uniflex actuator ratio t_p/t_b for maximum blocking force versus clearance L_1 for $L_a = 300 \mu\text{m}$.

A.6 Maximum Blocking Force Design with Additional Flextensional Actuator Results

Figures A.10 and A.11 show the variation of maximum blocking force F and corresponding displacement with actuator length L_a . Unimorph actuator produces highest blocking force followed by uniflex and flextensional actuators. Higher clearances produce larger blocking forces in uniflex actuator. Figure A.12 shows that a thicker aluminum cap is needed at larger clearances to produce maximum blocking force.

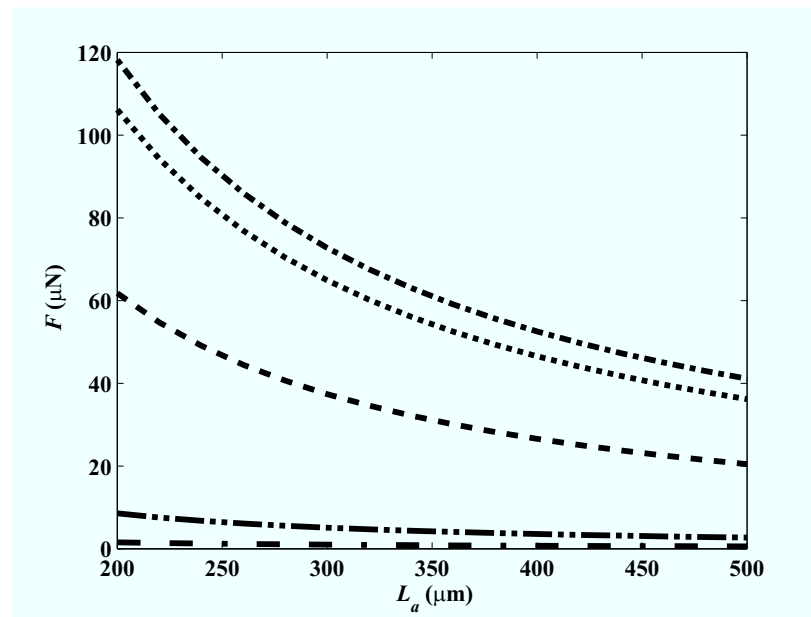


Figure A.10. Maximum blocking force F versus length L_a : uniflex actuator with clearance $L_1 = 2.7 \mu\text{m}$ (dashed) and $L_1 = 40 \mu\text{m}$ (dotted), unimorph actuator (dash-dotted), and flexensional actuator with $L_1 = 2.7 \mu\text{m}$ (dash-double dotted) and $L_1 = 40 \mu\text{m}$ (double dash-dotted).

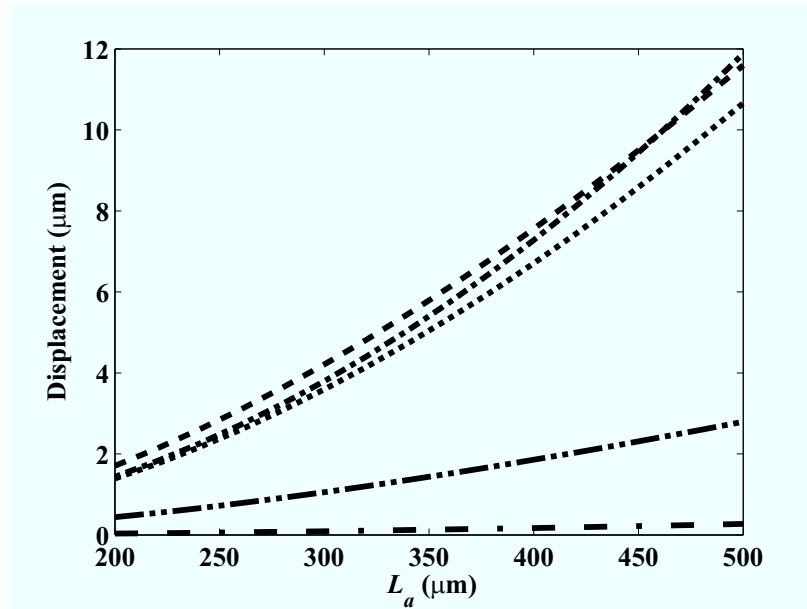


Figure A.11. Displacement for maximum blocking force configuration versus length L_a : uniflex $w_2(L)$ with clearance $L_1 = 2.7 \mu\text{m}$ (dashed) and $L_1 = 40 \mu\text{m}$ (dotted), unimorph actuator $w_3(0)$ (dash-dotted), and flextensional actuator $w_2(L)$ with $L_1 = 2.7 \mu\text{m}$ (dash-double dotted) and $L_1 = 40 \mu\text{m}$ (double dash-dotted).

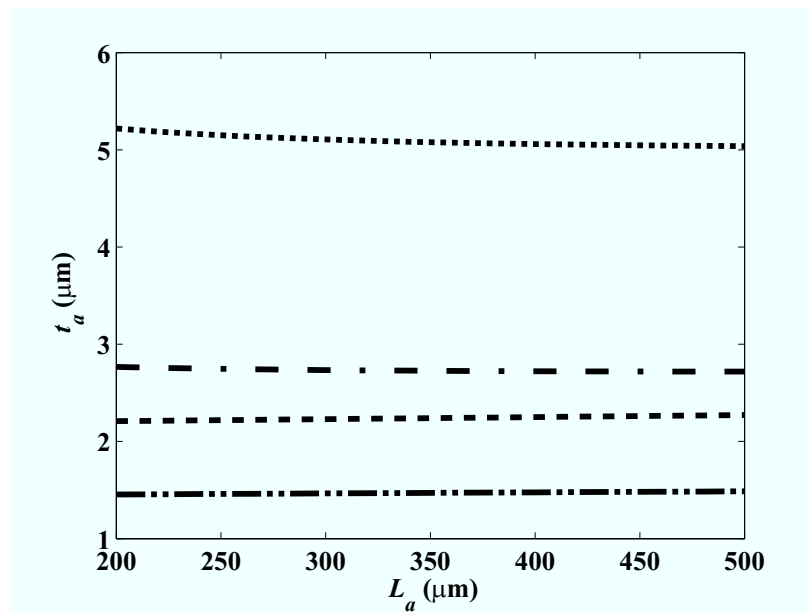


Figure A.12. Al thickness t_a for maximum blocking force versus length L_a : uniflex with clearance $L_1 = 2.7 \mu\text{m}$ (dashed) and $L_1 = 40 \mu\text{m}$ (dotted), and flextensional actuator with clearance $L_1 = 2.7 \mu\text{m}$ (dash-double dotted) and $L_1 = 40 \mu\text{m}$ (double dash-dotted).

Appendix **B**

Additional Results for T-beam

Actuator

Figures B.1 to B.15 show the out of plane and inplane displacements, and out of plane blocking forces at the tip for the devices 1, 2, 4, 5, and 6 (see Tab. 4.3). Solid lines in yellow, green, red, cyan, and blue represent the experimental data for 500, 400, 300, 200, and 100 V peak actuation voltage of triangle wave, respectively. The symbols (diamond, star, circle, plus, square, and triangle) are the average peak to peak data for 10 cycles.

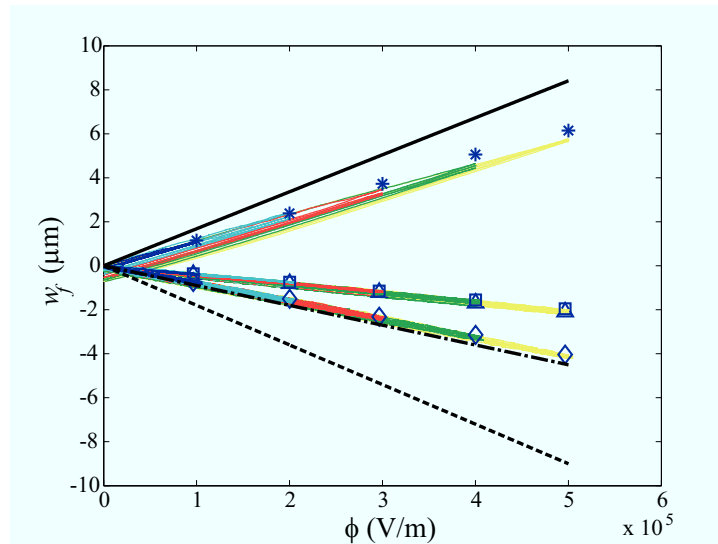


Figure B.1. Applied electric field ϕ versus free tip out of plane displacement w_f for Device 1: Theoretical (solid - web actuation, dashed - flange actuation, dashdot - right or left flange actuation) and experimental (star - web actuation, diamond - flange actuation, square - left flange, and triangle - right flange).

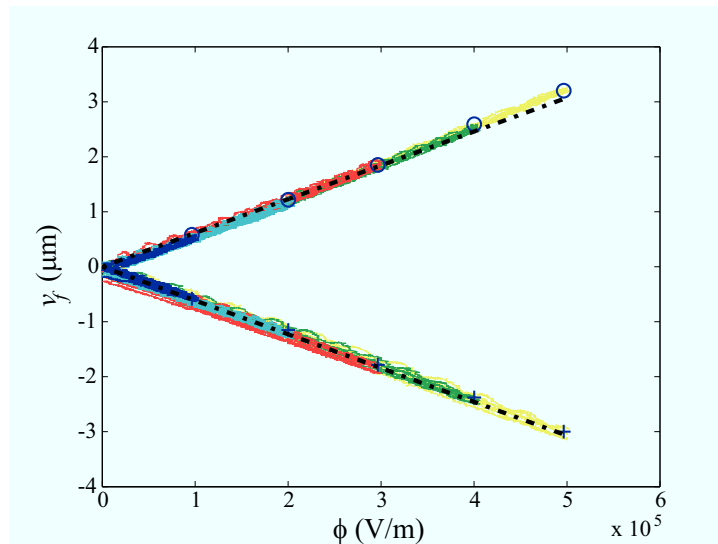


Figure B.2. Applied electric field, ϕ versus in-plane displacement tip displacement, v_f for Device 1: theoretical (dashdot - Right flange (top), left flange (bottom)) and experimental (plus - left flange, circle - right flange).

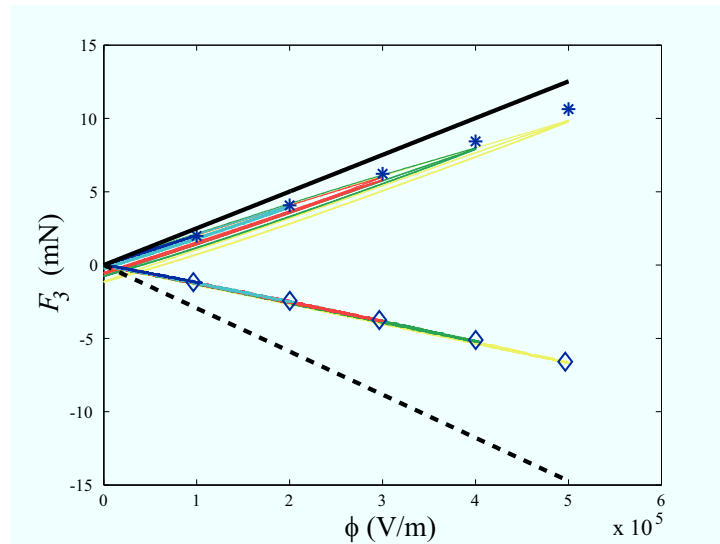


Figure B.3. Applied electric field ϕ versus tip force, F_3 for Device 1: Theoretical (solid - web actuation, dashed - flange actuation) and experimental (star - web actuation, diamond - flange actuation).

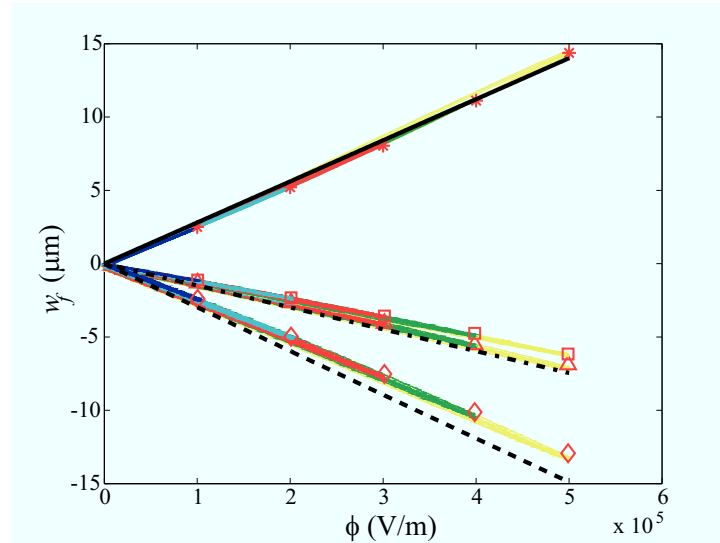


Figure B.4. Applied electric field ϕ versus free tip out of plane displacement w_f for Device 2: Theoretical (solid - web actuation, dashed - flange actuation, dashdot - right or left flange actuation) and experimental (star - web actuation, diamond - flange actuation, square - left flange, and triangle - right flange).

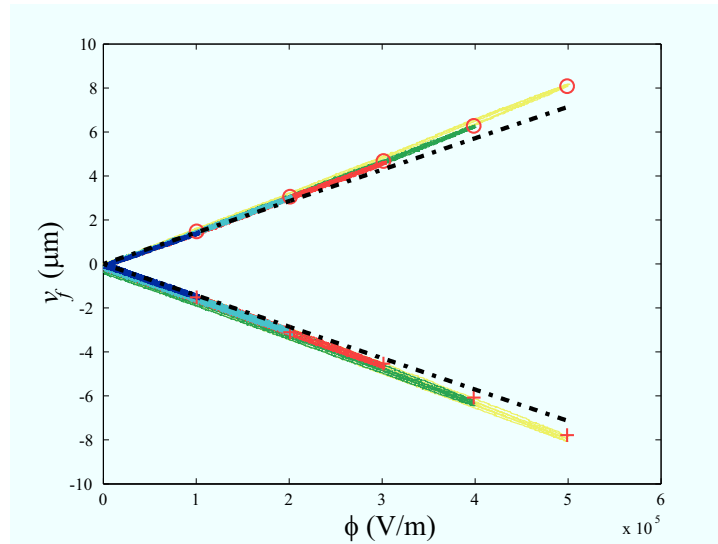


Figure B.5. Applied electric field, ϕ versus in-plane displacement tip displacement, v_f for Device 2: theoretical (dashdot - Right flange (top), left flange (bottom)) and experimental (plus - left flange, circle - right flange).

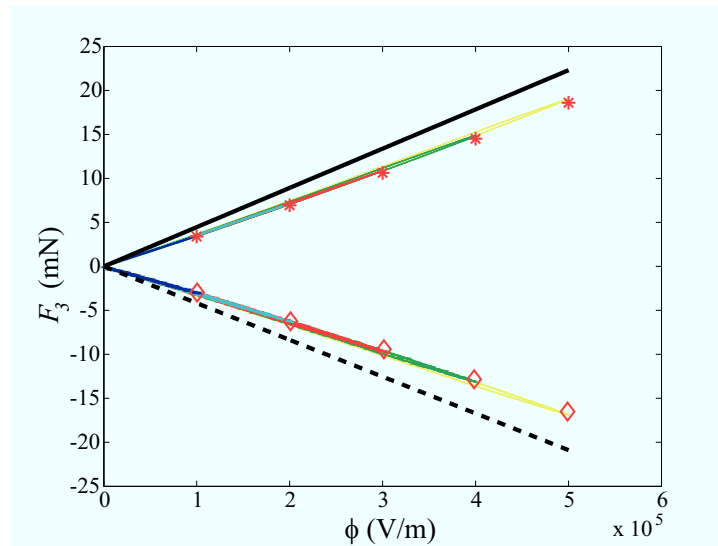


Figure B.6. Applied electric field ϕ versus tip force, F_3 for Device 2: Theoretical (solid - web actuation, dashed - flange actuation) and experimental (star - web actuation, diamond - flange actuation).

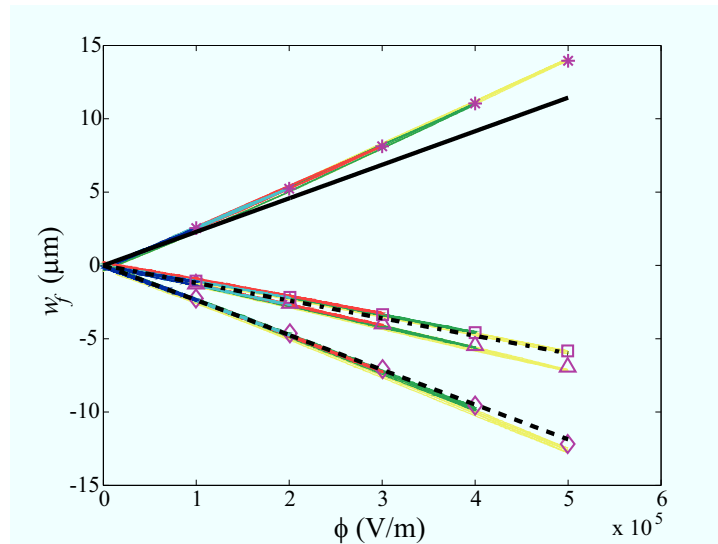


Figure B.7. Applied electric field ϕ versus free tip out of plane displacement w_f for Device 4: Theoretical (solid - web actuation, dashed - flange actuation, dashdot - right or left flange actuation) and experimental (star - web actuation, diamond - flange actuation, square - left flange, and triangle - right flange).

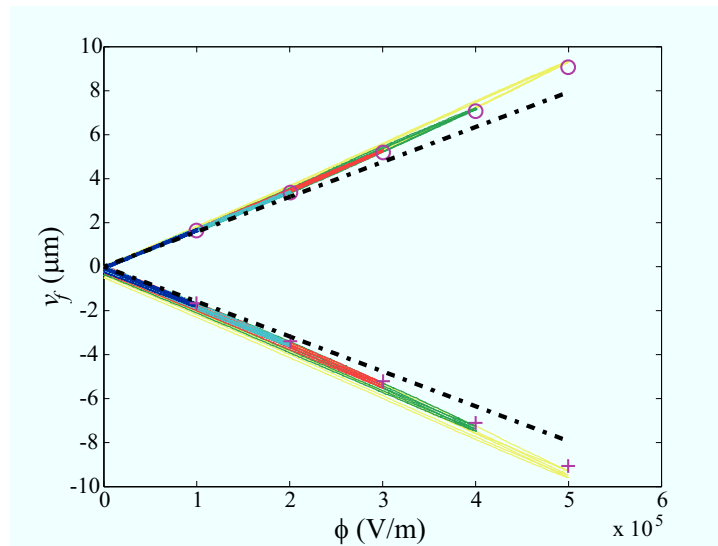


Figure B.8. Applied electric field, ϕ versus in-plane displacement tip displacement, v_f for Device 4: theoretical (dashdot - Right flange (top), left flange (bottom)) and experimental (plus - left flange, circle - right flange).

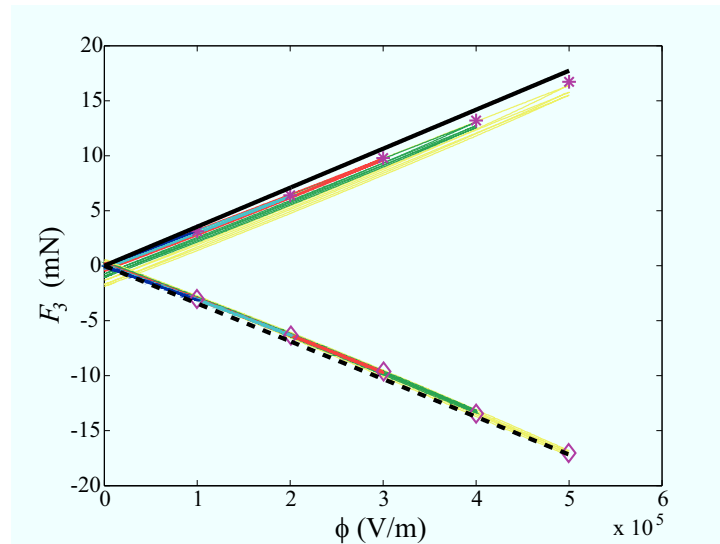


Figure B.9. Applied electric field ϕ versus tip force, F_3 for Device 4: Theoretical (solid - web actuation, dashed - flange actuation) and experimental (star - web actuation, diamond - flange actuation).

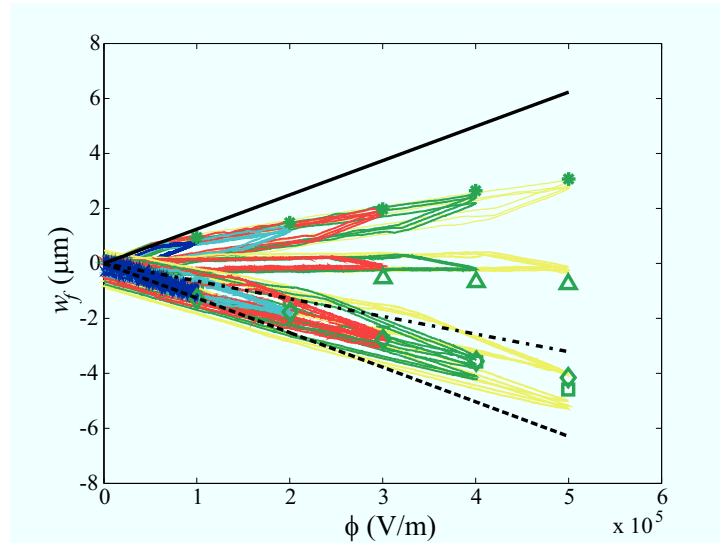


Figure B.10. Applied electric field ϕ versus free tip out of plane displacement w_f for Device 5: Theoretical (solid - web actuation, dashed - flange actuation, dashdot - right or left flange actuation) and experimental (star - web actuation, diamond - flange actuation, square - left flange, and triangle - right flange).

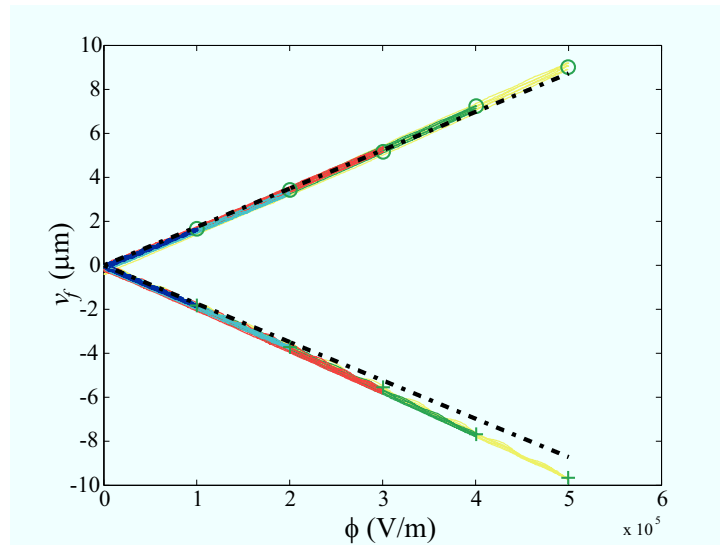


Figure B.11. Applied electric field, ϕ versus in-plane displacement tip displacement, v_f for Device 5: theoretical (dashdot - Right flange (top), left flange (bottom)) and experimental (plus - left flange, circle - right flange).

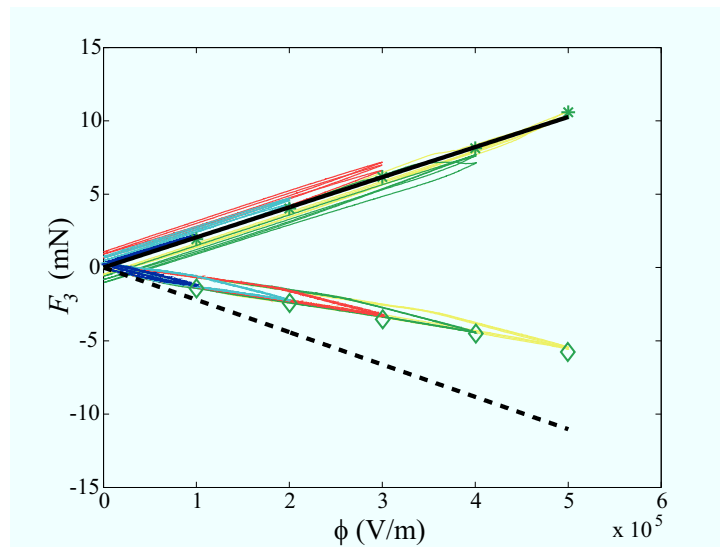


Figure B.12. Applied electric field ϕ versus tip force, F_3 for Device 5: Theoretical (solid - web actuation, dashed - flange actuation) and experimental (star - web actuation, diamond - flange actuation).

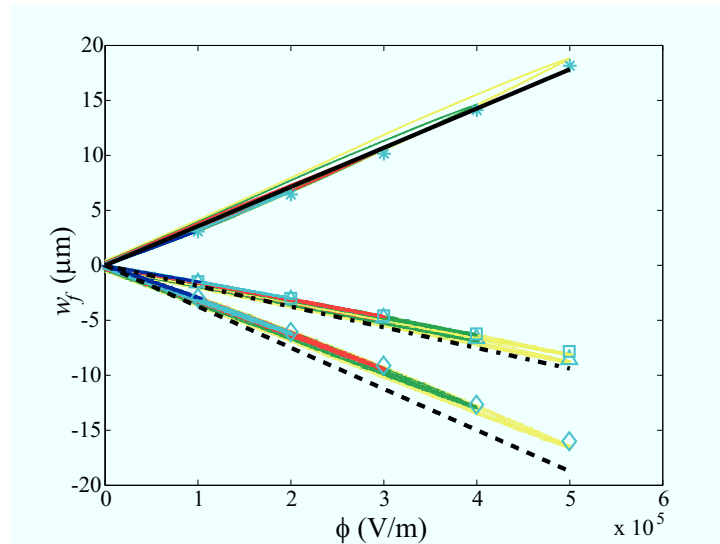


Figure B.13. Applied electric field ϕ versus free tip out of plane displacement w_f for Device 6: Theoretical (solid - web actuation, dashed - flange actuation, dashdot - right or left flange actuation) and experimental (star - web actuation, diamond - flange actuation, square - left flange, and triangle - right flange).

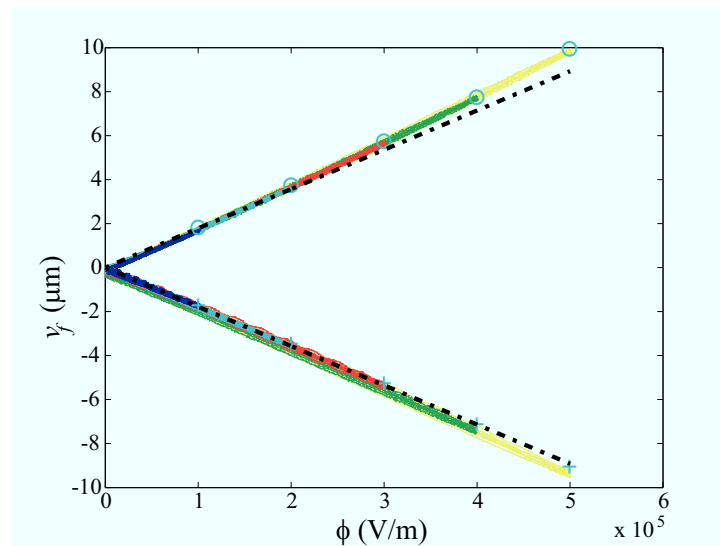


Figure B.14. Applied electric field, ϕ versus in-plane displacement tip displacement, v_f for Device 6: theoretical (dashdot - Right flange (top), left flange (bottom)) and experimental (plus - left flange, circle - right flange).

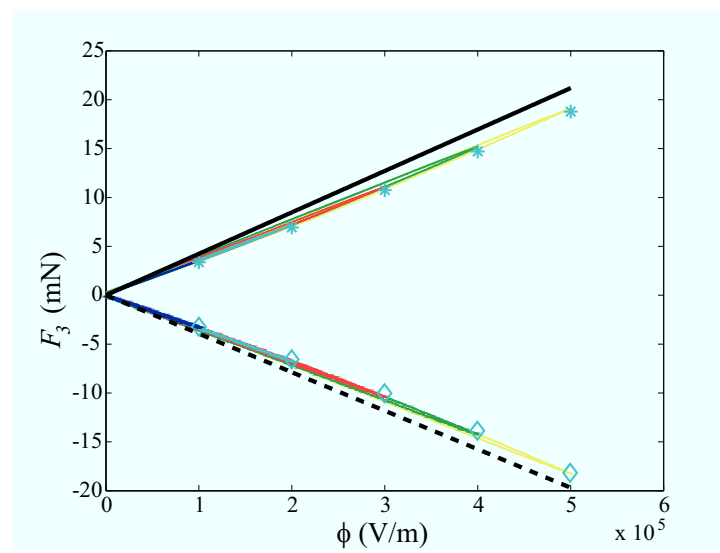


Figure B.15. Applied electric field ϕ versus tip force, F_3 for Device 6: Theoretical (solid - web actuation, dashed - flange actuation) and experimental (star - web actuation, diamond - flange actuation).

Bibliography

- [1] BERLINCOURT, D. A., C. CMOLIK, and H. JAFFE (1960) “Piezoelectric Properties of Polycrystalline Lead Titanate Zirconate Compositions,” *Proceedings of the Institute of Radio Engineers*, **48**(2), pp. 220–229.

- [2] SETTER, N., D. DAMJANOVIC, L. ENG, G. FOX, S. GEVORGIAN, S. HONG, A. KINGON, H. KOHLSTEDT, N. Y. PARK, G. B. STEPHENSON, I. STOLITCHNOV, A. K. TAGANSTEV, D. V. TAYLOR, T. YAMADA, and S. STREIFFER (2006) “Ferroelectric Thin Films: Review of materials, properties, and applications,” *Journal of Applied Physics*, **100**(5), setter, N. Damjanovic, D. Eng, L. Fox, G. Gevorgian, S. Hong, S. Kingon, A. Kohlstedt, H. Park, N. Y. Stephenson, G. B. Stolitchnov, I. Taganstev, A. K. Taylor, D. V. Yamada, T. Streiffer, S.

- [3] ARDELEAN, E. V., D. G. COLE, and R. L. CLARK (2004) “High Performance ”V-stack” Piezoelectric Actuator,” *Journal of Intelligent Material Systems and Structures*, **15**(11), pp. 879–889.

- [4] SPANGLER, R. L. and S. R. HALL (1990) “Piezoelectric Actuators for Helicopter Rotor Control,” *31st Structures, Structural Dynamics and Materials Conference*.

- [5] STRAUB, F. K. and D. J. MERKLEY (1995) "Design of a Smart Material Actuator for Rotor Control," *SPIE Proceedings*, **2443**, pp. 89–104.
- [6] STRAUB, F. K., M. A. EALEY, and M. SCHETKY (1997) "Application of Smart Materials to Helicopter Rotor Active Control," *SPIE*, **3044**, pp. 99–113.
- [7] GIURGIUTIU, V. (2000) "Review of Smart-Materials Actuation Solutions for Aeroelastic and Vibration Control," *Journal OF Intelligent Material Systems And Structures*, **11**, pp. 525–544.
- [8] LEE, T. and I. CHOPRA (1998) "Design and Static Testing of a Trailing Edge Flap Actuator with Piezostacks for a Rotor Blade," *SPIE Conference on Smart Structures and Integrated Systems*, **3329**, pp. 321–332.
- [9] TRESSLER, J. F. and T. R. HOWARTH (2002) "A Comparison of the Underwater Acoustic Performance of Cymbal-Based Projectors to 1-3 Piezocomposite Materials," *Journal of Electroceramics*, **8**, pp. 175–186.
- [10] KANNO, I., T. KUNISAWA, T. SUZUKI, and H. KOTERA (2007) "Development of Deformable Mirror Composed of Piezoelectric Thin Films for Adaptive Optics," *IEEE Journal of Selected Topics in Quantum Electronics*, **13**(2), pp. 155–161, kanno, Isaku Kunisawa, Takaaki Suzuki, Takaaki Kotera, Hidetoshi.
- [11] ANON (2002) "Piezo Autofocus Lens in VLDM," *Research Disclosure*, (505), p. 495.
- [12] KANEKO, T., K. OHBA, N. MITSUMOTO, and N. KAWAHARA (2000) "Quick Response Dynamic Focusing Lens Using Multi-layered Piezoelectric Bimorph Actuator," *Proceedings of SPIE - The International Society for Optical Engineering*, **4075**, pp. 24–31.

- [13] ZHANG, Q. and Z. S. LU (2006) "A Study on Design of Ultra-precision Micro-feed Stage," in *Advances in Machining & Manufacturing Technology Viii*, vol. 315-316 of *Key Engineering Materials*, pp. 131–135, zhang, Q. Lu, Z. S.
- [14] TING, Y., H. C. JAR, and C. C. LI (2007) "Measurement and calibration for Stewart micromanipulation system," *Precision Engineering-Journal of the International Societies for Precision Engineering and Nanotechnology*, **31**(3), pp. 226–233.
- [15] SCHEEPER, P. R., A. G. H. VAN DER DANK, W. OLTHUIS, and P. BERGVELD (1994) "Review of Silicon Microphone," *Sensors and Actuators*, **A44**, pp. 1–11.
- [16] KUHNEL, W. and G. HESS (1992) "Micromachined Subminiature Condenser Microphones in Silicon," *Sensors and Actuators*, **A32**, pp. 560–564.
- [17] LEE, S. S., R. P. RIED, and R. M. WHITE (1996) "Piezoelectric Cantilever Microphone and Microspeaker," *Journal of Microelectromechanical Systems*, **5**(4), pp. 238–242.
- [18] REN, T. L., L. T. ZHANG, L. T. LIU, and Z. J. LI (2002) "Design Optimization of Beam-like Ferroelectrics-Silicon Microphone and Microspeaker," *IEEE Transactions on Ultrasonics Ferroelectrics and Frequency Control*, **49**(2), pp. 266–270.
- [19] MORRIS, C. J. and F. K. FORSTER (2000) "Optimization of a Circular Piezoelectric Bimorph for a Micropump Driver," *Journal of Micromechanics and Microengineering*, **10**(3), pp. 459–465.
- [20] EDERER, I., P. RAETSCH, W. SCHULLERUS, C. TILLE, and U. ZECH (1997) "Piezoelectrically Driven Micropump for On-demand Fuel-drop Generation in an

- Automobile Heater with Continuously Adjustable Power Output,” *Sensors and Actuators a-Physical*, **62**(1-3), pp. 752–755.
- [21] WANG, B. and Q. XIA (2008) “Numerical Analysis on two Kinds of Cymbal membranes for Piezoelectric Micro-flow Actuator,” *Journal of Intelligent Material Systems and Structures*, **19**(3), pp. 343–349.
- [22] KANNO, I., H. ENDO, T. SUZUKI, and H. KOTERA (2005) “Piezoelectric Micro-actuators for RF-MEMS Switches,” *Pacific Rim Conference on Lasers and Electro-Optics, CLEO/Pacific Rim 2005*, pp. 1380–1381.
- [23] LEE, H.-C., J.-H. PARK, and Y.-H. PARK (2007) “Development of Shunt Type Ohmic RF MEMS Switches Actuated by Piezoelectric Cantilever,” *Sensors and Actuators, A: Physical*, **136**(1), pp. 282–290.
- [24] POLCAWICH, R. G., D. JUDY, J. S. PULSKAMP, S. TROLIER-MCKINSTRY, and M. DUBEY (2007) “Advances in Piezoelectrically Actuated RF MEMS Switches and Phase Shifters,” *EEE MTT-S International Microwave Symposium Digest, 2007*, pp. 2083–2086.
- [25] GIURGIUTIU, V. and C. A. ROGERS (1996) “Energy Based Comparison of Solid State Induced Strain Actuators,” *Journal of Intelligent Material Systems and Structures*, **7**, pp. 4–14.
- [26] GIURGIUTIU, V., C. A. ROGERS, and Z. CHAUDHRY (1997) “Design of Displacement Amplified Induced-Strain Actuators for Maximum Energy Output,” *Journal of Mechanical Design*, **119**, pp. 511–517.
- [27] UCHINO, K. (2000) *Ferroelectric devices*, Marcel Dekker, New York.

- [28] POMIRLEANU, R. and V. GIURGIUTIU (2002) "Full-stroke Static and Dynamic Analysis of High-power Piezoelectric Actuators," *Journal Of Intelligent Material Systems And Structures*, **13**, pp. 275–289.
- [29] SITTI, M. (2003) "Piezoelectrically Actuated Four-Bar Mechanism With Two Flexible Links for Micromechanical Flying Insect Thorax," *IEEE/ASME Transactions on Mechatronics*, **8**(1).
- [30] AVADHANU, S., R. WOOD, E. STELTZ, J. YAN, and R. FEARING (2003) "Lift Force Improvements for the Micromechanical Flying Insect," *Proceedings of the 2003 IROS*.
- [31] SMITS, J. G. and W.-S. CHOI (1991) "The Constituent Equations of Piezoelectric Heterogeneous Bimorphs," *IEEE Transactions on Ultrasonics, Ferroelectrics, and Frequency control*, **38**(3), pp. 256–270.
- [32] BASAK, S., A. RAMAN, and S. V. GARIMELLA (2005) "Dynamic Response Optimization of Piezoelectrically Excited Thin Resonant Beams," *Journal of Vibration and Acoustics*, **127**, pp. 18–27.
- [33] WANG, Q.-M., X.-H. DU, B. XU, and L. E. CROSS (1999) "Electromechanical Coupling and Output Efficiency of Piezoelectric Bending Actuators," *IEEE Transactions on Ultrasonics, Ferroelectrics, and Frequency control*, **46**(3), pp. 1947–1955.
- [34] DEVOE, D. L. and A. P. PISANO (1997) "Modeling and Optimal Design of Piezoelectric Cantilever Microactuators," *Journal of Microelectromechanical Systems*, **6**(3), pp. 266–270.

- [35] HA, S. K. and Y. H. KIM (2002) "Analysis of a Piezoelectric Multimorph in Extensional and Flexural Motions," *Journal of Sound and Vibration*, **253**(5), pp. 1001–1014.
- [36] BOOIJ, W. E., A. H. VOGL, D. T. WANG, F. TYHOLDT, N. P. STB, H. RAEDER, and K. PRUME (2007) "A Simple and Powerful Analytical Model for MEMS Piezoelectric Multimorphs," *Journal of Electroceramics*, **19**, pp. 387–393.
- [37] BERG, M., P. HAGEDORN, and S. GUTSCHMIDT (2004) "On the Dynamics of Piezoelectric Cylindrical Shells," *Journal of Sound and Vibration*, **274**(1-2), pp. 91–109.
- [38] NEWNHAM, R. E., A. DOGAN, and S. YOSHIKAWA (1993) "Flextensional Moonie Actuators," *IEEE Ultrasonics Symposium*, pp. 509–513.
- [39] JIANG, J. and E. MOCKENSTRUM (2006) "A Motion Amplifier Using an Axially Driven Buckling Beam:I. Design and Experiments," *Nonlinear Dynamics*, **43**, pp. 391–409.
- [40] DOGAN, A., K. UCHINO, and R. E. NEWNHAM (1997) "Composite Piezoelectric Transducer with Truncated Conical Endcaps Cymbal," *IEEE Transactions on Ultrasonics, Ferroelectrics, and Frequency Control*, **44**(3), pp. 597–605.
- [41] DOGAN, A., J. F. FERNANDEZ, K. UCHINO, and R. E. NEWNHAM (1996) "Cymbal Electromechanical Actuator," *EEE International Symposium on Applications of Ferroelectrics*, **1**, pp. 213–216.
- [42] OCHOA, P., M. VILLEGAS, and J. F. FERNANDEZ (2001) "Properties and Applications of Cymbal Piezocomposites," *Boletin De La Sociedad Espanola De Ceramica Y Vidrio*, **40**(4), pp. 301–308.

- [43] LAM, K. H., H. L. W. CHAN, H. S. LUO, Q. R. YIN, Z. W. YIN, and C. L. CHOY (2001) “Cymbal Actuators Fabricated Using PMN-PT Single Crystal,” *Ferroelectrics*, **263**(1-4), pp. 1535–1540.
- [44] LAM, K. H., X. X. WANG, and H. L. W. CHAN (2006) “Lead-free Piezoceramic Cymbal Actuator,” *Sensors and Actuators a-Physical*, **125**(2), pp. 393–397.
- [45] WANG, X. X., S. W. OR, K. H. LAM, H. L. W. CHAN, P. K. CHOY, and P. C. K. LIU (2006) “Cymbal Actuator Fabricated Using $(\text{Na}_{0.46}\text{K}_{0.46}\text{Li}_{0.08})\text{NbO}_3$ Lead-free Piezoceramic,” *Journal of Electroceramics*, **16**(4), pp. 385–388.
- [46] OCHOA, P., M. VILLEGAS, and J. F. FERNANDEZ (2002) “Resonant Frequency Response of Cymbal Transducer,” *Integrated Ferroelectrics*, **273**, pp. 321–326.
- [47] GUO, S. S., W. P. LI, Z. B. XING, G. C. LIU, and X. Z. ZHAO (2005) “Displacement Amplification and Resonance Characteristics of the Cymbal Transducers,” *Sensors and Actuators, A: Physical*, **121**(1), pp. 213–220.
- [48] OCHOA, P., M. VILLEGAS, and J. F. FERNANDEZ (2002) “Effective Piezoelectric Coefficient Calculation of Cymbal Piezocomposite,” *Ferroelectrics*, **273**, pp. 2693–2698.
- [49] SILVA, E. C. N., S. NISHIWAKI, and N. KIKUCHI (2000) “Topology Optimization Design of Flexensional Actuators,” *IEEE Transactions on Ultrasonics, Ferroelectrics, and Frequency Control*, **47**(3), pp. 657–671.
- [50] SUN, C. L., K. H. LAM, H. L. W. CHAN, X. Z. ZHAO, and C. CHOY (2006) “A Novel Drum Piezoelectric-actuator,” *Applied Physics A: Materials Science and Processing*, **84**(4), pp. 385–389.

- [51] SUN, C. L., K. H. LAM, S. G. LU, H. L. W. CHAN, X. Z. ZHA, and C. L. CHOY (2007) “Effect of Geometry on the Characteristics of a Drum Actuator,” *Journal of Intelligent Material Systems and Structures*, **18**, pp. 1077–1082.
- [52] GOYAL, A., J. CHEONG, and S. A. TADIGADAPA (2004) “Tin-based Solder Bonding for MEMS Fabrication and Packaging Applications,” *Journal of Micromechanics and Microengineering*, **14**(6), pp. 819–825.
- [53] PERIN, G. (2001) “Micromachined Piezoelectrically Actuated Flexensional Transducers For High Resolution Printing And Imaging,” *IEEE Ultrasonics Symposium*, pp. 921–924.
- [54] PERCIN, G. and B. T. KHURI-YAKUB (2002) “Piezoelectrically Actuated Flexensional Micromachined Ultrasound Transducers,” *Ultrasonics*, **40**(1-8), pp. 441–448.
- [55] ——— (2002) “Piezoelectrically Actuated Flexensional Micromachined Ultrasound Transducers - I: Theory,” *IEEE Transactions on Ultrasonics Ferroelectrics and Frequency Control*, **49**(5), pp. 573–584.
- [56] ——— (2002) “Piezoelectrically Actuated Flexensional Micromachined Ultrasound Transducers - II: Fabrication and experiments,” *IEEE Transactions on Ultrasonics Ferroelectrics and Frequency Control*, **49**(5), pp. 585–595.
- [57] ——— (2002) “Micromachined Droplet Ejector Arrays for Controlled Ink-jet Printing and Deposition,” *Review of Scientific Instruments*, **73**(5), pp. 2193–2196.
- [58] CHEONG, J., A. GOYAL, S. A. TADIGADAPA, and C. D. RAHN (2005) “Fabrication and Performance of a Flexensional Microactuator,” *Journal of Micromechanics and Microengineering*, **15**, pp. 1947–1955.

- [59] TUOMINEN, J., J. LAPPALAINEN, J. HILTUNEN, J. OLLILA, and V. LANTTO (2006) "Piezoelectric Thin-film Unimorph Actuator for Optical Fibre Alignment Applications," *Journal of Optics a-Pure and Applied Optics*, **8**(7), pp. S398–S404.
- [60] LI, S. F. and S. C. CHEN (2003) "Analytical Analysis of a Circular PZT Actuator for Valveless Micropumps," *Sensors and Actuators a-Physical*, **104**(2), pp. 151–161.
- [61] POLCAWICH, R. G., J. S. PULSKAMP, D. JUDY, P. RANADE, S. TROLIER-MCKINSTRY, and M. DUBEY (2007) "Surface Micromachined Microelectromechanical Ohmic Series Switch Using Thin-Film Piezoelectric Actuators," *IEEE Transactions on Microwave Theory and Techniques*, **55**(12), pp. 2642–2654.
- [62] SUDARSAN, S., J. HILLER, B. KABIUS, and O. AUCIELLO (2007) "Piezoelectric/Ultrananocrystalline Diamond Heterostructures for High-Performance Multifunctional Micro/Nanoelectromechanical Systems," *Applied Physics letters*, **90**(13).
- [63] LEE, H.-C., J. Y. PARK, K. H. LEE, H. J. NAM, and J. U. BU (2004) "Silicon Bulk Micromachined RF MEMS Switches with 3.5 volts Operation by using Piezoelectric Actuator," *IEEE MTT-S International Microwave Symposium Digest*, **2**, pp. 585–588.
- [64] FOX, C. H. J., X. CHEN, H. W. JIANG, P. B. KIRBY, and S. MCWILLIAM (2002) "Development of Micromachined RF Switches with Piezofilm Actuation," *Proceedings of SPIE - The International Society for Optical Engineering*, **4700**, pp. 40–49.

- [65] ONGKODJOJO, A., F. E. H. TAY, and R. AKKIPEDDI (2005) "Micromachined III-V Multimorph Actuators for MOEMS Applications: Concept, Design, and Model," *Journal of Microelectro Mechanical Systems*, **14**(3), pp. 610–618.
- [66] PERIN, G. and B. T. KHURI-YAKUB (2003) "Photoresist Deposition Without Spinning," *IEEE Transactions on Semiconductor Manufacturing*, **16**(9), pp. 452–459.
- [67] GROSS, S. J., S. A. TADIGADAPA, T. N. JACKSON, S. TROLIER-MCKINSTRY, and Q. Q. ZHANG (2003) "Lead-Zirconate-Titanate Based Piezoelectric Micro-machined Switch," *Applied Physics Letters*, **83**(1), pp. 174–176.
- [68] KOMMEPALLI, H. K. R., H. G. YU, C. L. MUHLSTEIN, S. TROLIER-MCKINSTRY, C. D. RAHN, and S. A. TADIGADAPA (2009) "Design, Fabrication, and Performance of a Piezoelectric Uniflex Microactuator," *Journal of Microelectromechanical Systems*.
- [69] KOMMEPALLI, H. K. R., A. D. HIRSH, C. D. RAHN, and S. A. TADIGADAPA (2008) "Piezoelectric T-beam Microactuators," *accepted for Proceedings of ASME 2008 International Design Engineering Technical Conference & Computers and Information in Engineering Conference*.
- [70] WOLF, R. A. (2001), "Temperature Dependence of the Piezoelectric Response of Lead Zirconate Titanate Films for MEMS Applications," M.S. thesis, The Pennsylvania State University, University Park, PA.
- [71] SUBASINGHE, S. S., A. GOYAL, and S. TADIGADAPA (2006) "High aspect ratio plasma etching of bulk Lead Zirconate Titanate," *Proceedings of SPIE: Micromachining and Microfabrication Process Technology XI, San Jose, CA*, pp. 100–108, Mary-Ann Maher, H. D. S., and Jung-Chih Chiao, Ed. SPIE: San Jose, CA, 2006.

- [72] SCHNEIDER, D. and M. D. TUCKER (1996) "Non-destructive characterization and evaluation of thin films by laser-induced ultrasonic surface waves," *Thin Solid Films*, **290-291**, pp. 305–311.
- [73] ZHANG, Q. Q., S. J. GROSS, S. TADIGADAPA, T. N. JACKSON, F. T. DJUTH, and S. TROLIER-MCKINSTRY (2003) "Lead zirconate titanate films for d33 mode cantilever actuators," *Sensors and Actuators A: Physical*, **105**, pp. 91–97.
- [74] CHINMULGUND, M., R. B. INTURI, and J. A. BARNARD (1995) "Effect of Ar gas pressure on growth, structure, and mechanical properties of sputtered Ti, Al, TiAl, and Ti₃Al films," *Thin Solid Films*, **270**, pp. 260–263.
- [75] POLCAWICH, R. G. and S. TROLIER-MCKINSTRY (2000) "Piezoelectric and dielectric reliability of lead zirconate titanate thin films," *Journal of Materials Research*, **15**, pp. 2505–2513.
- [76] WANG, L.-P., R. A. WOLF, W. YU, K. DENG, L. ZOU, R. J. DAVIS, and S. TROLIER-MCKINSTRY (2003) "Design, Fabrication, and Measurement of High-sensitivity Piezoelectric Microelectromechanical Systems Accelerometers," *Journal of Microelectromechanical Systems*, **12**, pp. 433–439.
- [77] CONWAY, N. J., Z. J. TRAINA, and S.-G. KIM (2007) "A strain amplifying piezoelectric MEMS actuator," *Journal of Micromechanics and Microengineering*, **17**, p. 781.
- [78] FOSTER, J. D. and R. M. WHITE (2005) "High aspect ratio piezoelectric bimorph transducer," in *Proceedings of the Electrochemical Society, Meeting Abstracts. Quebec, Canada: Electrochemical Society Inc.*, p. 1765.

- [79] KOMMEPALLI, H. K. R., H. G. YU, S. A. TADIGADAPA, C. D. RAHN, S. TROLIER-MCKINSTRY, and C. L. MUHLSTEIN (2008) "Displacement and Blocking Force Modeling for Piezoelectric Uniflex Microactuators," *Proceedings of ASME 2008 International Design Engineering Technical Conference & Computers and Information in Engineering Conference*.

HAREESH KOMMEPALLI

EDUCATION

PhD, Dept. of Mechanical Engineering, The Pennsylvania State University, University Park, PA **May 2010**

- GPA 3.97/4.00
- **PhD minor** in Computational Science

Master of Science, Dept. of Mechanical and Nuclear Engineering, The Pennsylvania State University, University Park, PA **December, 2008**

- GPA 3.97/4.00

Master of Technology, Dept. of Mechanical Engineering, Indian Institute of Technology Madras, India, **April 2003**

- GPA 9.42/10.00 (Rank 2)

Bachelor of Technology, Dept. of Mechanical Engineering, Sri Krishnadevaraya University, India, **April 2001**

- Percent- 85% (Topper – Gold medalist)

RESEARCH INTERESTS

My research interests include Solid mechanics, Micro-Electro-Mechanical Systems (MEMS), Structural Dynamics, Finite Element Analysis, Control Systems, and Bio-mechanics.

PUBLICATIONS

- **Kommepalli, H. K. R.**, H. G. Yu, S. A. Tadigadapa, C. D. Rahn, S. Trolier-McKinstry, and C. L. Muhlstein (2008) "Displacement and Blocking Force Modeling of Piezoelectric Uniflex Microactuators", *Proceedings of ASME 2008 IDETC/CIE, Aug 3-6, 2008, Brooklyn, Newyork, USA*
- **Kommepalli, H. K. R.**, A. D. Hirsh, C. D. Rahn, S. A. Tadigadapa (2008) "Piezoelectric T-beam Microactuators", *Proceedings of ASME 2008 IDETC/CIE, Aug 3-6, 2008, Brooklyn, Newyork, USA*
- **Kommepalli, H. K. R.**, H. G. Yu, C. L. Muhlstein, S. Trolier-McKinstry, C. D. Rahn, and S. A. Tadigadapa (2009) "Design, Fabrication and Performance of Piezoelectric Uniflex Microactuator", *IEEE JMEMS, 18(3), pp. 616 - 625*
- **Kommepalli, H. K. R.**, C. D. Rahn, S. A. Tadigadapa (2009) "Displacement and Blocking Force Optimization of MEMS Uniflex Actuators", *Proceedings of ASME 2009 IDETC/CIE, Aug 30- Sept 2, 2009, San Diego, California, USA*
- **Kommepalli, H. K. R.**, K. Mateti, C. D. Rahn, S. A. Tadigadapa (2010) "Performance Characteristics of Piezoelectric T-beam Actuators", *to be submitted to Proceedings of ASME 2010 IDETC/CIE*
- **Kommepalli, H. K. R.**, K. Mateti, C. D. Rahn, S. A. Tadigadapa (2010) "Piezoelectric T-beam Actuators", *to be submitted to ASME Journal of Mechanical Design*
- Mateti, K., **H. K. R. Kommepalli**, S. A. Tadigadapa, C. D. Rahn (2009) "Claping Wing Nano Air Vehicle Using Piezoelectric T-beam Actuators", *Proceedings of the ASME 2009 Conference on smart materials, Adaptive Structures and Intelligent Systems, Sept 20-24, 2009, Oxnard, California, USA*

WORK EXPERIENCE

- Design Engineer at General Electric Aviation, Bangalore India, 2003 – 2005
- Summer Intern at General Electric Global Research Center, Niskayuna, NY Summer, 2008 & Summer, 2009
- Graduate research assistant at Mechatronics Research Laboratory, The Pennsylvania State University, 2006 – 2010
- Graduate teaching assistant at The Pennsylvania State University, 2005 – 2006

AWARDS AND ACHIEVEMENTS

- Obtained Tau Beta Pi, Golden Key membership for academic excellence at The Pennsylvania State University
- Received three management awards and highly coveted "Hats off award" for outstanding performance, stretch and delivering the high quality results meeting the strict business deadlines at *General Electric Aviation*
- Awarded prestigious "DAAD Fellowship" (German Academic Exchange Service) during the master's program
- Awarded the prestigious "*Young Engineering Fellowship*" by the Indian Institute of Science, Bangalore, during summer 2000
- Member of American Society of Mechanical Engineers (ASME)